SANDIA REPORT
SAND2022-12772
Printed January 2023

Sandia National Laboratories

An Immersed Finite Element Lagrangian-Eulerian Code-Coupling Framework

M. A. Christon, N. S. Nanal, C. Shen, D. M. Hensinger, L. T. Zhang, M. K. Wong, A. M. Agelastos

Prepared by
Sandia National Laboratories
Albuquerque, New Mexico 87185
Livermore, California 94550

Issued by Sandia National Laboratories, operated for the United States Department of Energy by National Technology & Engineering Solutions of Sandia, LLC.

Available to DOE and DOE contractors from

U.S. Department of Energy
Office of Scientific and Technical Information
P.O. Box 62
Oak Ridge, TN 37831

Telephone: (865) 576-8401
Facsimile: (865) 576-5728
E-Mail: reports@osti.gov
Online ordering: http://www.osti.gov/scitech

Available to the public from

U.S. Department of Commerce
National Technical Information Service
5301 Shawnee Road
Alexandria, VA 22312

Telephone: (800) 553-6847
Facsimile: (703) 605-6900
E-Mail: orders@ntis.gov
Online order: https://classic.ntis.gov/help/order-methods

ABSTRACT

This report presents an assessment of immersed Eulerian-Lagrangian code-coupling techniques suitable for use in a broad range of mechanics applications. The coupling algorithm is based on an immersed finite element method that considers the Lagrangian and Eulerian overlap regions in the overall variational formulation. In this report the basic formulation details are presented followed by various aspects of the code-coupling algorithm using *OpenIFEM* as the Lagrangian/coupling framework. A series of representative test cases that illustrate the code-coupling algorithm are discussed. The current work provides an in-depth investigation into the immersed finite element method for the purposes of providing a rigorous coupling technique that is minimally invasive in the respective Eulerian and Lagrangian codes. A number of extensions to the base immersed finite element method have been examined. These extension include nodal and quadrature-based indicator functions, a Lagrangian volume-fraction calculation in regions of overlap, and the use of penalty constraints between the Lagrangian and Eulerian domains. A unique MPI-based coupling strategy that retains the independent MPI structure of each code has been demonstrated.

CONTENTS

1. Introduction & Background 13

2. Formulation 14
   2.1. Penalty Constraints 16

3. Coupled Algorithm 19
   3.1. Definitions 20
   3.2. Data Flow 23
   3.3. Stable Time-Step 25
   3.4. Lagrangian Traction Forces 26
   3.5. Lagrangian Boundary Added-Mass 27
   3.6. Eulerian Coupling Nodal Mass 28
   3.7. Overlap Indicator Update 31
      3.7.1. Lagrangian Volume Fraction 32
   3.8. Eulerian Coupling Forces 35
   3.9. Uniform Strain Elements 36
   3.10. Penalty Constraints – Eulerian Momentum Equations 37
   3.11. Penalty Constraints – Lagrangian Momentum Equations 41
   3.12. Velocity Reset with Void 43
   3.13. Subcycling for Time-Integration 44
   3.14. Eulerian Remap Issues 44

4. Results 45
   4.1. Block-On-Air 46
      4.1.1. Baseline Calculations 46
      4.1.2. Coupled, Matched Background Material 49
      4.1.3. Coupled, Void Background Material 51
      4.1.4. Leakage Issues 51
      4.1.5. Static Case, Matched Background Material 54
      4.1.6. Static Case, Void Background Material 56
   4.2. Two Ball Impact Test 58
      4.2.1. Eulerian 59
      4.2.2. Eulerian – with Inter-material Fracture 62
      4.2.3. Coupled, Matched Background Material 65
      4.2.4. Coupled, Matched Background Material, Inter-material Fracture 68
      4.2.5. Coupled, Void Background Material 71
   4.3. Normal Hemispherical Penetrator 74
      4.3.1. Force-Coupling, Void Background 75
      4.3.2. Force-Coupling, Air Background 79
      4.3.3. Preliminary Penalty Assessment 84
   4.4. Oblique Hemispherical Penetrator 91
   4.5. Programmed Burn Loading on a Ball 98
      4.5.1. Force-Coupling, Low-Pressure Air Background 98

4.5.2. Force-Coupling, Matched Background Material 106
4.6. Shock Loading on Balls and Walls 112
4.7. Sphere – Concrete Impact 121

5. Summary and Conclusions 127

References 128

Appendix A. SABLE Keywords 129

Appendix B. OpenIFEM Keywords 130

LIST OF FIGURES

Figure 2-1. Schematic representation of the computational domain. 14
Figure 3-1. Multiple materials contained in an Eulerian element with an overlapping Lagrangian element. The void volume fraction is reserved as material 0, and the material volume fraction is $\mathcal{F}^E = \mathcal{F}^1 + \mathcal{F}^2$. 21
Figure 3-2. Lagrangian elements overlapping the Eulerian element, and the associated intersection volumes V_1 and V_2 used used for the Lagrangian volume fraction calculation. 21
Figure 3-3. Lagrangian elements overlapping the Eulerian element and the associated density (ρ_1, ρ_2) and stress (σ_1, σ_2) used to compute the average Lagrangian density and stress on the Eulerian element. 22
Figure 3-4. Overlapping Lagrangian and Eulerian elements used to compute the traction forces on the Lagrangian body. Surface quadrature points are indicated by x, Eulerian nodes by •, and Eulerian centroids by •. 27
Figure 3-5. Normal offset for traction integration. Surface quadrature points are indicated by x, Eulerian nodes by •, and Eulerian centroids by • 27
Figure 3-6. Interpolation of the Eulerian nodal mass at the nodes of the overlapping Lagrangian mesh. 28
Figure 3-7. Penetrator-target model with void where the Lagrangian penetrator resides in the Eulerian mesh: (a) penetrator-target geometry, (b) Eulerian lumped mass for the target, (c) coupling lumped mass on the Eulerian mesh. 30
Figure 3-8. Overlap models: (a) completely inside, and (b) partially inside. 31
Figure 3-9. Indicator criteria: (a) node-based, and (b) quadrature-point based for completely-inside model. $\phi = 1$ for the elements filled in blue. 32
Figure 3-10. Schematic representation of Lagrangian overlap calculation (a) overlap geometry, (b) calculation for Lagrangian element:1, (c) calculation for Lagrangian element:2. 34
Figure 3-11. Interpolation of Lagrangian nodal values to Eulerian nodes in overlap regions. 36
Figure 3-12. Integration points on the Lagrangian boundary relative to the Eulerian elements. Surface quadrature points are indicated by ⋆, and Eulerian nodes by •. 40
Figure 4-1. Block-on-air geometry. 46

Figure 4-2. Snapshot of (a) the Eulerian velocity and (b) the Eulerian displacement at $50\mu s$. 47
Figure 4-3. Y-momentum time histories for rigid-body ($\times$) and Eulerian ($\triangle$) calculations. 48
Figure 4-4. Kinetic energy time histories for rigid-body ($\square$) and Eulerian ($+$) calculations. 48
Figure 4-5. Snapshot of (a) the Lagrangian velocity and (b) the Lagrangian displacement at $50\mu s$. 49
Figure 4-6. Y-momentum time histories for rigid-body ($\times$), Eulerian ($\triangle$), and coupled ($+$) calculations. 50
Figure 4-7. Kinetic energy time histories for rigid-body ($\bigcirc$), Eulerian ($\triangle$), and coupled ($\square$) calculations. 50
Figure 4-8. Snapshot of (a) the Lagrangian velocity and (b) the Lagrangian displacement at $50\mu s$. 51
Figure 4-9. Y-momentum time histories for rigid-body ($\times$), Eulerian ($\triangle$), and coupled ($+$) calculations. 52
Figure 4-10. Kinetic energy time histories for rigid-body ($\bigcirc$), Eulerian ($\triangle$), and coupled ($\square$) calculations. 52
Figure 4-11. Snapshots of the Eulerian gas (red) and void volume fraction (blue) on the left and the Lagrangian block and velocities on the right at (a) $t = 0\ s$, (b) $t = 3.75 \times 10^{-3}\ s$, and (c) $t = 7.0 \times 10^{-3}\ s$. 53
Figure 4-12. Snapshot of (a) the Eulerian gas velocity and (b) the gas volume fraction at $50\mu s$. 54
Figure 4-13. Y-momentum time history for the Eulerian gas. 55
Figure 4-14. Kinetic energy time history for the Eulerian gas. 55
Figure 4-15. Snapshot of (a) the Eulerian gas velocity and (b) the gas volume fraction at $50\mu s$. 56
Figure 4-16. Y-momentum time history for the Eulerian gas. 57
Figure 4-17. Kinetic energy time history for the Eulerian gas. 57
Figure 4-18. Two ball impact geometry. 58
Figure 4-19. Y-momentum time histories for lower (–) and upper (–) copper balls. 59
Figure 4-20. Kinetic energy time histories for lower (–) and upper (–) copper balls. 60
Figure 4-21. Y-position time histories for lower (–) and upper (–) copper balls. 60
Figure 4-22. Y-velocity time histories for lower (–) and upper (–) copper balls. 61
Figure 4-23. Y-momentum time histories for lower (–) and upper (–) copper balls. 62
Figure 4-24. Kinetic energy time histories for lower (–) and upper (–) copper balls. 63
Figure 4-25. Y-position time histories for lower (–) and upper (–) copper balls. 63
Figure 4-26. Y-velocity time histories for lower (–) and upper (–) copper balls. 64
Figure 4-27. Y-momentum time histories for the lower (–) and upper Eulerian (–) balls and the Lagrangian (–) copper ball in the coupled calculation. The baseline Eulerian y-momentum histories are shown for the lower (–) and upper (–) balls. 65
Figure 4-28. Kinetic energy time histories for the lower (–), upper Eulerian (–) and Lagrangian (–) copper balls in the coupled calculation. The Eulerian baseline histories are shown for the lower (–) and upper (–) balls. 66
Figure 4-29. Y-position time histories for the lower (–), upper Eulerian (–) and Lagrangian (–) copper balls in the coupled calculation. The Eulerian baseline histories are shown for the lower (–) and upper (–) balls. 66

Figure 4-30. Y-velocity time histories for the lower (–), upper Eulerian (–) and Lagrangian (- -) copper balls in the coupled calculation. The Eulerian baseline histories are shown for the lower (–) and upper (–) balls. 67
Figure 4-31. Y-momentum time histories for the lower (–), upper Eulerian (–) and Lagrangian (–) copper balls with the Eulerian baseline histories for the lower (–) and upper (–) balls. 68
Figure 4-32. Kinetic energy time histories for the lower (–), upper Eulerian (–) and Lagrangian (–) copper balls with the Eulerian baseline histories for the lower (–) and upper (–) balls. 69
Figure 4-33. Y-position time histories for the lower (–), upper Eulerian (–) and Lagrangian (- -) copper balls with the Eulerian baseline histories for the lower (–) and upper (–) balls. 69
Figure 4-34. Y-velocity time histories for the lower (–), upper Eulerian (–) and Lagrangian (- -) copper balls with the Eulerian baseline histories for the lower (–) and upper (–) balls. 70
Figure 4-35. Y-momentum time histories for the lower (–), void (–) and Lagrangian (–) copper balls with the Eulerian baseline histories for the lower (–) and upper (–) balls. 71
Figure 4-36. Kinetic energy time histories for the lower (–), void (–) and Lagrangian (–) copper balls with the Eulerian baseline histories for the lower (–) and upper (–) balls. 72
Figure 4-37. Y-position time histories for the lower (–), upper Eulerian (–) and Lagrangian (- -) copper balls with the Eulerian baseline histories for the lower (–) and upper (–) balls. 72
Figure 4-38. Y-velocity time histories for the lower (–), upper Eulerian (–) and Lagrangian (- -) copper balls with the Eulerian baseline histories for the lower (–) and upper (–) balls. 73
Figure 4-39. Hemispherical penetrator and concrete target. 74
Figure 4-40. Penetrator y-momentum time history for the Eulerian (- -) and coupled Eulerian-Lagrangian (–) calculations. 76
Figure 4-41. Penetrator kinetic energy time history for the Eulerian (- -) and coupled Eulerian-Lagrangian (–) calculations. 76
Figure 4-42. Target y-momentum time history for the Eulerian (- -) and coupled Eulerian-Lagrangian (–) calculations. 77
Figure 4-43. Target kinetic energy time history for the Eulerian (- -) and coupled Eulerian-Lagrangian (–) calculations. 77
Figure 4-44. Target velocity magnitude at $t = 50\mu s$ for (a) the Eulerian, and (b) the coupled Eulerian-Lagrangian calculations. 78
Figure 4-45. Penetrator y-momentum time history for the Eulerian (- -) and coupled Eulerian-Lagrangian (–) calculations. 80
Figure 4-46. Penetrator kinetic energy time history for the Eulerian (- -) and coupled Eulerian-Lagrangian (–) calculations. 80
Figure 4-47. Target y-momentum time history for the Eulerian (- -) and coupled Eulerian-Lagrangian (–) calculations. 81

Figure 4-48. Target kinetic energy time history for the Eulerian (- -) and coupled Eulerian-Lagrangian (–) calculations. 81
Figure 4-49. Air x-velocity at $t = 50\mu s$ for the Eulerian and coupled Eulerian-Lagrangian calculations. 82
Figure 4-50. Air y-velocity at $t = 50\mu s$ for the Eulerian and coupled Eulerian-Lagrangian calculations. 83
Figure 4-51. Penetrator y-momentum time history for the Eulerian (–) and coupled Eulerian-Lagrangian calculations with (LP,EP) = (0.0,0.0) (–), (LP,EP) = (0.5,0.0) (–), (LP,EP) = (1.0,0.0) (–). 85
Figure 4-52. Target y-momentum time history for the Eulerian (–) and coupled Eulerian-Lagrangian calculations with (LP,EP) = (0.0,0.0) (–), (LP,EP) = (0.5,0.0) (–), (LP,EP) = (1.0,0.0) (- -). 85
Figure 4-53. Penetrator tip position time history for the Eulerian (–) and coupled Eulerian-Lagrangian calculations with (LP,EP) = (0.0,0.0) (–), (LP,EP) = (0.5,0.0) (–), (LP,EP) = (1.0,0.0) (- -). 86
Figure 4-54. Penetrator kinetic energy time history for the Eulerian (–) and coupled Eulerian-Lagrangian calculations with (LP,EP) = (0.0,0.0) (- -), (LP,EP) = (0.5,0.0) (- -), (LP,EP) = (1.0,0.0) (- -). 86
Figure 4-55. Penetrator y-momentum time history for the Eulerian (–) and coupled Eulerian-Lagrangian calculations with (LP,EP) = (0.0,0.0) (–), (LP,EP) = (0.0,0.5) (- -), (LP,EP) = (0.5,0.5) (- -), (LP,EP) = (1.0,0.5) (–). 87
Figure 4-56. Target y-momentum time history for the Eulerian (–) and coupled Eulerian-Lagrangian calculations with (LP,EP) = (0.0,0.0) (–), (LP,EP) = (0.0,0.5) (- -), (LP,EP) = (0.5,0.5) (- -), (LP,EP) = (1.0,0.5) (- -). 87
Figure 4-57. Penetrator tip position time history for the Eulerian (–) and coupled Eulerian-Lagrangian calculations with (LP,EP) = (0.0,0.0) (–), (LP,EP) = (0.0,0.5) (- -), (LP,EP) = (0.5,0.5) (- -), (LP,EP) = (1.0,0.5) (- -). 88
Figure 4-58. Penetrator kinetic energy time history for the Eulerian (–) and coupled Eulerian-Lagrangian calculations with (LP,EP) = (0.0,0.0) (- -), (LP,EP) = (0.0,0.5) (–), (LP,EP) = (0.5,0.5) (–), (LP,EP) = (1.0,0.5) (–). 88
Figure 4-59. Penetrator y-momentum time history for the Eulerian (–) and coupled Eulerian-Lagrangian calculations with (LP,EP) = (0.0,0.0) (–), (LP,EP) = (0.0,1.0) (–), (LP,EP) = (0.5,1.0) (–), (LP,EP) = (1.0,1.0) (–). 89
Figure 4-60. Target y-momentum time history for the Eulerian (–) and coupled Eulerian-Lagrangian calculations with (LP,EP) = (0.0,0.0) (–), (LP,EP) = (0.0,1.0) (- -), (LP,EP) = (0.5,1.0) (- -), (LP,EP) = (1.0,1.0) (- -). 89
Figure 4-61. Penetrator tip position time history for the Eulerian (–) and coupled Eulerian-Lagrangian calculations with (LP,EP) = (0.0,0.0) (–), (LP,EP) = (0.0,1.0) (- -), (LP,EP) = (0.5,1.0) (- -), (LP,EP) = (1.0,1.0) (- -). 90
Figure 4-62. Penetrator kinetic energy time history for the Eulerian (–) and coupled Eulerian-Lagrangian calculations with (LP,EP) = (0.0,0.0) (- -), (LP,EP) = (0.0,1.0) (–), (LP,EP) = (0.5,1.0) (–), (LP,EP) = (1.0,1.0) (–). 90
Figure 4-63. Oblique impact hemispherical penetrator and concrete target. 91
Figure 4-64. Penetrator x-momentum time history for the Eulerian (- -) and coupled Eulerian-Lagrangian (–) calculations. 92

Figure 4-65. Penetrator y-momentum time history for the Eulerian (- -) and coupled Eulerian-Lagrangian (–) calculations. 93
Figure 4-66. Penetrator kinetic energy time history for the Eulerian (- -) and coupled Eulerian-Lagrangian (–) calculations. 93
Figure 4-67. Target x-momentum time history for the Eulerian (- -) and coupled Eulerian-Lagrangian (–) calculations. 94
Figure 4-68. Target y-momentum time history for the Eulerian (- -) and coupled Eulerian-Lagrangian (–) calculations. 94
Figure 4-69. Target kinetic energy time history for the Eulerian (- -) and coupled Eulerian-Lagrangian (–) calculations. 95
Figure 4-70. Final configuration for (a) the Eulerian simulation and (b) the coupled (OPENIFEM – SABLE) simulation. 96
Figure 4-71. Comparison of the (a) the final projectile position and target material interface for the Eulerian (–) and coupled (–) simulations, and (b) the target material location for the Eulerian (blue) and coupled (red) simulations. 97
Figure 4-72. Programmed burn loading on a ball geometry. 98
Figure 4-73. Snapshots of the gas pressure and ball location at $t = 2.1 \times 10^{-5} s$ for (a) the Eulerian simulation, and (b) the coupled simulation. 100
Figure 4-74. Snapshots of the gas pressure and ball location at $t = 3.1 \times 10^{-5} s$ for (a) the Eulerian simulation, and (b) the coupled simulation. 101
Figure 4-75. Ball y-momentum time history for the Eulerian (–) and Lagrangian (–) calculations. 102
Figure 4-76. Ball kinetic energy time history for the Eulerian (–) and Lagrangian (–) calculations. 102
Figure 4-77. Ball y-position time history for the Eulerian (–) and Lagrangian (–) calculations. 103
Figure 4-78. Ball y-velocity time history for the Eulerian (–) and Lagrangian (–) calculations. 103
Figure 4-79. Snapshots of the HE pressure and ball location showing (a) the residual pressure halo below the Lagrangian ball, and (b) the high pressure region behind the Lagrangian ball. 104
Figure 4-80. Snapshots of the velocity field and ball location for (a) the Eulerian calculation, and (b) the coupled simulation. 105
Figure 4-81. Snapshots of the gas pressure and ball location at $t = 2.1 \times 10^{-5} s$ for (a) the Eulerian simulation, and (b) the coupled simulation. 107
Figure 4-82. Snapshots of the gas pressure and ball location at $t = 3.1 \times 10^{-5} s$ for (a) the Eulerian simulation, and (b) the coupled simulation. 108
Figure 4-83. Ball y-momentum time history for the Eulerian (–) and Lagrangian (–) calculations. 109
Figure 4-84. Ball kinetic energy time history for the Eulerian (–) and Lagrangian (–) calculations. 109
Figure 4-85. Ball y-position time history for the Eulerian (–) and Lagrangian (–) calculations. 110
Figure 4-86. Ball y-velocity time history for the Eulerian (–) and Lagrangian (–) calculations. 110
Figure 4-87. Snapshots of the velocity field and ball location for (a) the Eulerian calculation, and (b) the coupled simulation using a matched background material. . . . 111
Figure 4-88. Shock loading on balls and walls geometry. 113

Figure 4-89. Snapshots of the gas pressure and ball location at $t = 1.89 \times 10^{-4}[s]$ for (a) the Eulerian simulation, and (b) the coupled simulation. 114
Figure 4-90. Snapshots of the gas pressure and ball location at $t = 3.79 \times 10^{-4}[s]$ for (a) the Eulerian simulation, and (b) the coupled simulation. 115
Figure 4-91. Ball-1 position as a function of time: Lagrangian (–) and Eulerian (–) x-position; Lagrangian (–) and Eulerian (–) y-position. 116
Figure 4-92. Ball-1 velocity as a function of time: Lagrangian (–) and Eulerian (–) x-velocity; Lagrangian (–) and Eulerian (–) y-velocity. 116
Figure 4-93. Ball-2 position as a function of time: Lagrangian (–) and Eulerian (–) x-position; Lagrangian (–) and Eulerian (–) y-position. 117
Figure 4-94. Ball-2 velocity as a function of time: Lagrangian (- -) and Eulerian (–) x-velocity; Lagrangian (–) and Eulerian (–) y-velocity. 117
Figure 4-95. Ball-3 position as a function of time: Lagrangian (–) and Eulerian (–) x-position; Lagrangian (- -) and Eulerian (–) y-position. 118
Figure 4-96. Ball-3 velocity as a function of time: Lagrangian (–) and Eulerian (- -) x-velocity; Lagrangian (- -) and Eulerian (–) y-velocity. 118
Figure 4-97. Ball-4 position as a function of time: Lagrangian (- -) and Eulerian (–) x-position; Lagrangian (–) and Eulerian (–) y-position. 119
Figure 4-98. Ball-4 velocity as a function of time: Lagrangian (- -) and Eulerian (–) x-velocity; Lagrangian (–) and Eulerian (–) y-velocity. 119
Figure 4-99. Ball-5 position as a function of time: Lagrangian (- -) and Eulerian (–) x-position; Lagrangian (–) and Eulerian (–) y-position. 120
Figure 4-100. Ball-5 velocity as a function of time: Lagrangian (- -) and Eulerian (–) x-velocity; Lagrangian (- -) and Eulerian (–) y-velocity. 120
Figure 4-101. Sphere – concrete impact problem. 121
Figure 4-102. Sphere penetration depth time history for the Eulerian (–) and coupled Eulerian-Lagrangian (–) calculations. 123
Figure 4-103. Sphere z-momentum time history for the Eulerian (–) and coupled Eulerian-Lagrangian (–) calculations. 123
Figure 4-104. Penetrator kinetic energy time history for the Eulerian (–) and coupled Eulerian-Lagrangian (- -) calculations. 124
Figure 4-105. Target z-momentum time history for the Eulerian (–) and coupled Eulerian-Lagrangian (–) calculations. 124
Figure 4-106. Target kinetic energy time history for the Eulerian (–) and coupled Eulerian-Lagrangian (–) calculations. 125
Figure 4-107. Target velocity magnitude at $t = 100\mu s$ for (a) the Eulerian, and (b) the coupled Eulerian-Lagrangian calculations. 126

LIST OF TABLES

Table 2-1. mIFEM nomenclature 14
Table 3-1. Grid transfer operations (L: Lagrangian, E: Eulerian). 23
Table 3-2. Algorithmic flow, communication steps and data flow. function() indicates a fixed algorithmic step in the respective solvers. 24

Table 4-1. Cases considered for the two ball impact problem. 59
Table 4-2. Penetration depth based on the tip of the penetrator for Eulerian and coupled simulations at $t = 500\mu s$. 75
Table 4-3. Penetration depth based on the tip of the penetrator for Eulerian and coupled simulations at $t = 500\mu s$. 79
Table 4-4. Matrix of Lagrangian (LP) and Eulerian (EP) penalty scale factors. 84
Table 4-5. Ball and tracer point locations. The ball identifiers correspond to the numbers in Figure 4-88. 112
Table 4-6. Penetration depth based on the base of the sphere for Eulerian and coupled simulations at $t = 100\mu s$. 122

1. INTRODUCTION & BACKGROUND

This report presents an assessment of immersed Lagrangian-Eulerian code coupling techniques suitable for a broad range of mechanics applications. The immersed finite element method (IFEM) [6], [7] is a non-boundary conforming method used for the simulation of fluid-structure interaction. IFEM, inspired by the immersed boundary (IB) method originally proposed by Peskin [3] and [4], seeks to provide a rigorous variational foundation for coupled fluid-solid interaction solution methods.

In contrast, the IB method describes a solid boundary using a set of Lagrangian points connected with springs "floating" on top of a fixed Eulerian grid. Since both fluid and solid domains are represented independently, frequent re-meshing is not required to accommodate nonlinear displacements, large strains, and rigid body motion of the solid. In the IB method, the immersed boundary is connected using discrete points, thus the boundary (even if enclosing a volume) does not technically occupy volume and material behavior cannot be described using an appropriate constitutive law. IFEM was originally developed specifically to allow solids to occupy volume in the computational domain and to describe the solids using a rich set of constitutive relations rather than just an elastic model.

The underlying methods for the code-coupling considered here are based on the work of Zhang, et al. [1, 6, 5]. The initial work by Zhang, et al. [6] introduced the immersed finite element method (IFEM) as a formalism for performing immersed boundary simulations while avoiding some of the limitations of Peskin's algorithm [4, 3]. In this work, the reproducing kernel particle method (RKPM) was used to interpolate velocities, and distribute restoring forces between the Lagrangian and Eulerian finite element models.

The work by Wang and Zhang [5] modified the immersed finite element method by assuming that the Lagrangian material drives the motion of the overlapping background Eulerian material. This modification permits the description of the Lagrangian material to be more accurately represented, and to ensure that the Eulerian material motion, particularly when it is highly dynamic, is consistent with the behavior of the Lagrangian body.

In 2019, Cheng, Yu and Zhang [1] introduced OPENIFEM as an open-source software base for performing immersed finite element simulations. This code base, in particular, the coupling scheme and concomitant data communications that enable independent Lagrangian and Eulerian solvers, is used for the study reported here.

In the following sections, we present an overview of the formulation used for the coupled Lagrangian-Eulerian simulations. The data communications and algorithmic details are presented in §3. A series of prototypical coupled simulations in §4 are used to demonstrate the Eulerian-Lagrangian coupled method using OPENIFEM with SABLE. Finally a summary of the work and future directions is presented in §5.

2. FORMULATION

In this section, the modified IFEM (mIFEM) formulation is presented. The basic IFEM formulation is based on the conservation of virtual work, and is not restricted to fluid-structure interaction. Similarly, the modified IFEM (mIFEM) formulation for Eulerian-Lagrangian solid-solid is based on virtual work conservation.

Following the idea of the immersed finite element method, we assume that one or more materials occupy the entire background computational domain Ω, and are described using an Eulerian description. One or more deformable solids, represented as separate meshes with a Lagrangian description, are completely immersed in the background domain and occupy volume Ω^L. The computational domain Ω can be divided into real Eulerian region Ω^E, which can be comprised of multiple materials, and the volume that overlaps with the Lagrangian solid. The overlap region is defined as the artificial domain $\bar{\Omega}$. It can be noted that $\Omega = \Omega^E \cup \Omega^L$ so that Ω^L coincides with the artificial domain $\bar{\Omega}$. The Eulerian and Lagrangian solid domains share a common interface $\Gamma^{int} = \Omega^E \cap \Omega^L$ which also coincides with the Lagrangian solid boundary Γ^L. Figure 2-1 shows a schematic representation and decomposition of the computational domains. The nomenclature associated with the two domains is shown in Table 2-1.

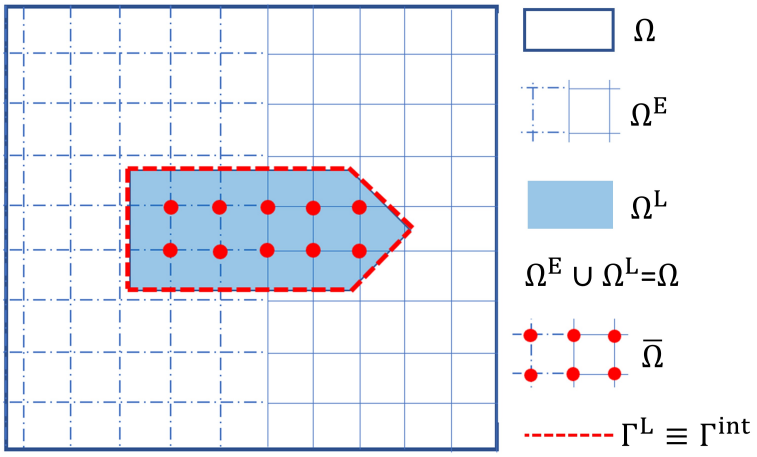

Figure 2-1 Schematic representation of the computational domain.

Parameters/variables	Lagrangian domain Ω^L	Eulerian domain Ω^E
density	ρ^L	ρ^E
velocity	$\mathbf{v}^L$	$\mathbf{v}^E$
stress	$\boldsymbol{\sigma}^L$	$\boldsymbol{\sigma}^E$

Table 2-1 mIFEM nomenclature

We begin with the weak form of the momentum equations for Eulerian and Lagrangian solids as follows

$$\int_{\Omega^{\mathrm{E}}} \delta v_i \left(\rho^{\mathrm{E}} \frac{\mathrm{D}v_i^{\mathrm{E}}}{\mathrm{D}t} - \sigma_{ij,j}^{\mathrm{E}} - \rho^{\mathrm{E}} g_i \right) d\Omega = 0 \tag{1a}$$

$$\int_{\Omega^{\mathrm{L}}} \delta v_i \left(\rho^{\mathrm{L}} \frac{\mathrm{D}v_i^{\mathrm{L}}}{\mathrm{D}t} - \sigma_{ij,j}^{\mathrm{L}} - \rho^{\mathrm{L}} g_i \right) d\Omega = 0 \tag{1b}$$

Combining Eq. (1a) and Eq. (1b):

$$\int_{\Omega^{\mathrm{E}}} \delta v_i \left(\rho^{\mathrm{E}} \frac{\mathrm{D}v_i^{\mathrm{E}}}{\mathrm{D}t} - \sigma_{ij,j}^{\mathrm{E}} - \rho^{\mathrm{E}} g_i \right) d\Omega + \int_{\Omega^{\mathrm{L}}} \delta v_i \left(\rho^{\mathrm{L}} \frac{\mathrm{D}v_i^{\mathrm{L}}}{\mathrm{D}t} - \sigma_{ij,j}^{\mathrm{L}} - \rho^{\mathrm{L}} g_i \right) d\Omega = 0 \tag{2}$$

We can re-write the second term in Eq. (2) to account for the virtual work done by the artificial domain $\bar{\Omega}$ as follows

$$\begin{aligned}
&\int_{\Omega^{\mathrm{L}}} \delta v_i \left(\rho^{\mathrm{L}} \frac{\mathrm{D}v_i^{\mathrm{L}}}{\mathrm{D}t} - \sigma_{ij,j}^{\mathrm{L}} - \rho^{\mathrm{L}} g_i \right) d\Omega \\
&= \int_{\Omega^{\mathrm{L}}} \delta v_i \left(\rho^{\mathrm{L}} \frac{\mathrm{D}v_i^{\mathrm{E}}}{\mathrm{D}t} - \sigma_{ij,j}^{\mathrm{E}} - \rho^{\mathrm{L}} g_i \right) d\Omega + \int_{\Omega^{\mathrm{L}}} \delta v_i \left(\rho^{\mathrm{L}} \left(\frac{\mathrm{D}v_i^{\mathrm{L}}}{\mathrm{D}t} - \frac{\mathrm{D}v_i^{\mathrm{E}}}{\mathrm{D}t} \right) - (\sigma_{ij,j}^{\mathrm{L}} - \sigma_{ij,j}^{\mathrm{E}}) \right) d\Omega \\
&= \int_{\bar{\Omega}} \delta v_i \left(\rho^{\mathrm{L}} \frac{\mathrm{D}v_i^{\mathrm{E}}}{\mathrm{D}t} - \sigma_{ij,j}^{\mathrm{E}} - \rho^{\mathrm{L}} g_i \right) d\Omega + \int_{\Omega^{\mathrm{L}}} \delta v_i \left(\rho^{\mathrm{L}} \left(\frac{\mathrm{D}v_i^{\mathrm{L}}}{\mathrm{D}t} - \frac{\mathrm{D}v_i^{\mathrm{E}}}{\mathrm{D}t} \right) - (\sigma_{ij,j}^{\mathrm{L}} - \sigma_{ij,j}^{\mathrm{E}}) \right) d\Omega
\end{aligned} \tag{3}$$

Substituting Eq. (3) into Eq. (2), the following equation is obtained

$$\begin{aligned}
\int_{\Omega^{\mathrm{E}}} \delta v_i \left(\rho^{\mathrm{E}} \frac{\mathrm{D}v_i^{\mathrm{E}}}{\mathrm{D}t} - \sigma_{ij,j}^{\mathrm{E}} - \rho^{\mathrm{E}} g_i \right) d\Omega + \int_{\bar{\Omega}} \delta v_i \left(\rho^{\mathrm{L}} \frac{\mathrm{D}v_i^{\mathrm{E}}}{\mathrm{D}t} - \sigma_{ij,j}^{\mathrm{E}} - \rho^{\mathrm{L}} g_i \right) d\Omega \\
+ \int_{\Omega^{\mathrm{L}}} \delta v_i \left(\rho^{\mathrm{L}} \left(\frac{\mathrm{D}v_i^{\mathrm{L}}}{\mathrm{D}t} - \frac{\mathrm{D}v_i^{\mathrm{E}}}{\mathrm{D}t} \right) - (\sigma_{ij,j}^{\mathrm{L}} - \sigma_{ij,j}^{\mathrm{E}}) \right) d\Omega = 0
\end{aligned} \tag{4}$$

The second term in Eq. (4) is the virtual work done by the Eulerian material in the artificial domain, which is then subtracted from the virtual work done by the Lagrangian solid in the third term. Since $\Omega^{\mathrm{E}} \cup \bar{\Omega} = \Omega$, we can re-write Eq. (4) as

$$\int_{\Omega} \delta v_i \left(\bar{\rho} \frac{\mathrm{D}v_i^{\mathrm{E}}}{\mathrm{D}t} - \sigma_{ij,j}^{\mathrm{E}} - \bar{\rho} g_i \right) d\Omega = \int_{\Omega^{\mathrm{L}}} \delta v_i \left(\rho^{\mathrm{L}} \left(\frac{\mathrm{D}v_i^{\mathrm{E}}}{\mathrm{D}t} - \frac{\mathrm{D}v_i^{\mathrm{L}}}{\mathrm{D}t} \right) + (\sigma_{ij,j}^{\mathrm{L}} - \sigma_{ij,j}^{\mathrm{E}}) \right) d\Omega \tag{5}$$

Eq. (5) is the weak form of the linear momentum equations for the entire computational domain. Here, an indicator function has been used to account for the presence of the artificial domain where the density is

$$\bar{\rho} = (1 - \phi(\vec{x}))\rho^{\mathrm{E}} + \phi(\vec{x})\rho^{\mathrm{L}} \tag{6}$$

and, ϕ is the indicator field defined as

$$\phi(\vec{x}) = \begin{cases} 0, & \vec{x} \text{ in } \Omega^{\mathrm{E}} \\ 1, & \vec{x} \text{ in } \bar{\Omega}. \end{cases} \tag{7}$$

The indicator field ϕ identifies the artificial domain $\bar{\Omega}$ in Ω and is used to define an appropriate density for the artificial domain. The effect of the Lagrangian solid in the Eulerian domain is managed by treating the forces from the Lagrangian solid as external forces and also removing the work done in the artificial domain. This impact is reflected in the right-hand-side of Eq. (5). It can be treated as an external forcing term acting on the Eulerian domain which is zero outside of $\bar{\Omega}$. We refer to this force as the coupling force, denoted by $\mathbf{f}^{\text{int}}$. Note that the coupling force is applied over the entire overlapping region of the Eulerian domain, and not just where the Lagrangian boundary overlaps the Eulerian domain. We re-write Eq. (5) as follows

$$\int_{\Omega} \delta v_i \left(\bar{\rho} \frac{\mathrm{D}v_i^{\mathrm{E}}}{\mathrm{D}t} - \sigma_{ij,j}^{\mathrm{E}} - \rho^{\mathrm{E}} g_i \right) d\Omega = \int_{\bar{\Omega}} \delta v_i f_i^{\text{int}} d\Omega \tag{8}$$

where,

$$f_i^{\text{int}} = \begin{cases} \rho^{\mathrm{L}} \left(\frac{\mathrm{D}v_i^{\mathrm{E}}}{\mathrm{D}t} - \frac{\mathrm{D}v_i^{\mathrm{L}}}{\mathrm{D}t} \right) + (\sigma_{ij,j}^{\mathrm{L}} - \sigma_{ij,j}^{\mathrm{E}}), & \text{in } \bar{\Omega} \\ 0, & \text{otherwise} \end{cases} \tag{9}$$

Eq. (8) along with Eq. (7) allows the background Eulerian mesh to be solved independently. Besides the interaction force, the interface conditions are also applied for the two domains to interact with each other. These conditions are: 1) a velocity continuity condition in $\bar{\Omega}$ Eq. (10a) and 2) traction continuity on Γ^{int} Eq. (10b).

$$\vec{v}^{\mathrm{E}} = \vec{v}^{\mathrm{L}} \qquad \text{in} \quad \bar{\Omega} \tag{10a}$$

$$\boldsymbol{\sigma}^{\mathrm{L}} \cdot \vec{n}^{\mathrm{L}} = \boldsymbol{\sigma}^{\mathrm{E}} \cdot \vec{n}^{\mathrm{E}} \qquad \text{on} \quad \Gamma^{\text{int}} \tag{10b}$$

These two conditions are obtained by applying integration by parts to the weak form of Eq. (9), rather than simply assumed as in the initial derivation of the immersed finite element method. This provides a rigorous enforcement of these conditions and provides additional consistency in the coupled solutions. The traction interface condition is satisfied by enforcing the traction forces from the Eulerian domain on the boundary of Lagrangian solid. Velocity continuity within the overlapping domain is satisfied by essentially replicating the Lagrangian velocity field by solving the Eulerian momentum equations with Lagrangian material properties. This issue of velocity continuity is explored further in §2.1. The general algorithm for the immersed solid-solid interaction problem is summarized below.

2.1. Penalty Constraints

In regions of overlap and at the Lagrangian boundary, it may be desirable to directly enforce velocity continuity between the Eulerian and Lagrangian velocities. Here, a penalty formulation is adopted based on the variational principles in Eq. (1b) and (2).

The velocity constraint is simply stated as

$$G(\mathbf{v}^L, \mathbf{v}^E) = (\mathbf{v}^L - \mathbf{v}^E) = 0 \tag{11}$$

Algorithm 1: Algorithm of the modified Immersed finite element method for solid-solid interactions.

Initialization of mesh, material properties, and solver parameters for all computational domains, Ω and Ω^{L};

for $time = t_0 : t_n$ **do**

(1) Evaluate traction boundary condition on Γ^{L} or Γ^{int} from the surrounding Eulerian domain by interpolating $\boldsymbol{\sigma}^{\mathrm{E}}$ onto the Lagrangian solid boundary satisfying Eqs. (10a) and (10b);

(2) Solve Lagrangian solid dynamics $\vec{v}^{\mathrm{L}}$ and $\boldsymbol{\sigma}^{\mathrm{L}}$, update the solid nodal position;

(3) Update indicator field $I(\vec{x})$ to identify the artificial domain $\bar{\Omega}$ in Ω, Eq. (7) and assign appropriate material properties as in Eq. (6);

(4) Evaluate interaction force using Eq. (9);

(5) Solve for Eulerian solid velocity $\vec{v}^{\mathrm{E}}$ and stress $\boldsymbol{\sigma}^{\mathrm{E}}$ in Ω using corresponding governing equations;

end

A quadratic form for the constraint may be added to the functional for either the Lagrangian or the Eulerian functional. The form of the functionals is well-known and omitted here for brevity. The quadratic form of the constraint is

$$\frac{\chi}{2}G(\mathbf{v}^L,\mathbf{v}^E)^2 = \frac{\chi}{2}(\mathbf{v}^L\cdot\mathbf{v}^L - 2\mathbf{v}^E\cdot\mathbf{v}^L + \mathbf{v}^E\cdot\mathbf{v}^E) \tag{12}$$

where χ is the penalty parameter.

In the following discussion, the addition of the penalty constraints to both the Eulerian and Lagrangian functionals is presented. However, it may be desirable to attempt to enforce the Lagrangian velocity as known relative to Eulerian domain based on the specific details of the Lagrangian and Eulerian time-integration methods. In some cases, permitting the Lagrangian velocity to "dominate" in the overlapping Eulerian region may be preferred.

The variation of the quadratic form of the penalty constraint with respect to the Eulerian velocity yields

$$\delta G = \chi^E(\mathbf{v}^E - \mathbf{v}^L)\delta\mathbf{v}^E \tag{13}$$

where the Lagrangian velocity $\mathbf{v}^L$ is presumed known, and the penalty parameter has been specialized to the Eulerian domain.

Applying the penalty constraint to the Eulerian problem, i.e., Eq.s (8) – (9), in the interior of the overlap region, $\bar{\Omega}$, the modified Eulerian variational statement is

$$\begin{aligned}\delta\tilde{J}^E = \int_\Omega \delta v_i\left(\bar{\rho}\frac{\mathrm{D}v_i^{\mathrm{E}}}{\mathrm{D}t} - \sigma_{ij,j}^{\mathrm{E}} - \bar{\rho}g_i\right)d\Omega - \int_{\bar{\Omega}}\delta v_i\left(\rho^{\mathrm{L}}\left(\frac{\mathrm{D}v_i^{\mathrm{E}}}{\mathrm{D}t} - \frac{\mathrm{D}v_i^{\mathrm{L}}}{\mathrm{D}t}\right) + (\sigma_{ij,j}^{\mathrm{L}} - \sigma_{ij,j}^{\mathrm{E}})\right)d\Omega \\ + \int_{\bar{\Omega}}\delta v_i\,\chi^E(v_i^{\mathrm{E}} - v_i^{\mathrm{L}})d\Omega = 0\end{aligned} \tag{14}$$

In this form, the penalty constraints attempt to *weakly* enforce velocity continuity on the unknown Eulerian velocity using a presumably known Lagrangian velocity.

The enforcement of the velocity continuity (aka, no-slip/no-penetration) at the Eulerian-Lagrangian boundary may take several forms depending on how the constraints are to be implemented. It is simpler to consider the constraint being applied to the boundary of the Lagrangian domain because this boundary is well defined. Using the constraint in Eq. (11) and the associated quadratic form in Eq. (12), the variation with respect to the Lagrangian velocity yields

$$\delta G = \chi^E(\mathbf{v}^L - \mathbf{v}^E)\delta\mathbf{v}^L \tag{15}$$

The variation with respect to the Lagrangian velocity presumes that the Eulerian velocity is known, and is consistent with the variation of the Lagrangian functional. As will be seen in later sections, this choice fits well with the overall algorithmic flow. However, other choices may be made as well.

Similar to the procedure used for the Eulerian variational statement, the modified Lagrangian variational principle is

$$\delta\tilde{J}^L = \int_{\Omega^{\mathrm{L}}} \delta v_i \left(\rho^{\mathrm{L}} \frac{\mathrm{D}v_i^{\mathrm{L}}}{\mathrm{D}t} - \sigma_{ij,j}^{\mathrm{L}} - \rho^{\mathrm{L}} g_i \right) d\Omega + \int_{\Omega^{\mathrm{L}}} \delta v_i \, \chi^L (v_i^{\mathrm{L}} - v_i^{\mathrm{E}}) d\Omega = 0 \tag{16}$$

Here, the superscript on the velocity variation has been dropped for simplicity, and the penalty multiplier χ^L has been specialized for the Lagrangian domain.

The most simple choice for the penalty multipliers that is scale and dimensionally consistent is

$$\chi^L = \chi^E = \frac{\theta\overline{\rho}}{\Delta t_{mid}} \tag{17}$$

where $0 \leq \theta \leq 1$ is an input scale factor, and Δt_{mid} is the mid-step time step associated with the central-differences time integrator typically associated with explicit Lagrangian codes and used in SABLE for the Lagrangian step. The penalty multipliers are not unique, and research on the best choice for the multipliers is an ongoing effort.

The discrete penalty constraints and their implementation are discussed in detail in §3.10 and §3.11.

3. COUPLED ALGORITHM

In this section, the steps of the coupled algorithm are presented in detail with an emphasis on the flow of data that requires communications, and the concomitant grid-transfer operations. The initial OPENIFEM – SABLE coupling algorithm was based in large part on the work in [6] and [7]. The methods research reported on here evolved a series of extensions to the base immersed finite element method in order to obtain a better, i.e, an effectively sharper interface representation with more accurate data for exchange at the interface. The versions investigated include

1. Version-0 (**V0**) using a nodal binary indicator function, considering only elements that are entirely inside the overlap region, and nodal-based (lifted via L^2 projection) stresses.
2. Version-1 (**V1**) using the node-based indicator and forces of **V0**, but including the use of element-centered stresses. This version distinguishes between the volume-fraction averaged stress field used for the residual force calculation, and the stress field used for the traction forces on the Lagrangian domain. For the traction forces, an material-average stress is used that can optionally filter out the contribution from the Eulerian background material in the overlap region. The two average stress definitions are presented in more detail in §3.1.
3. Version-2 (**V2**) derived from **V1**, and uses a scaling of the coupling forces by the Eulerian material volume-fraction. This method did not produce reasonable results and was dropped.
4. Version-3 (**V3**) is based on **V1**, but makes use of a Lagrangian volume fraction $\mathcal{F}^L$ that indicates the amount of volume in an Eulerian element that overlaps with the Lagrangian mesh. In addition, this method includes the ability to reset the velocity in overlap regions where there is pure void in the Eulerian mesh. In addition, an added-mass effect was integrated during the evolution of **V3**. Where appropriate, we note when the added-mass contribution is not used. There are two variants of **V3** that differ in how the overlap indicator and coupling forces are computed. **V3-nodes** uses the node-based indicator from **V0**, but makes use of the Lagrangian volume fraction. In contrast, **V3-quadrature** uses quadrature points in the Eulerian element to determine the overlap indicator and for the calculation of the coupling forces. See §3.7 for additional details.

In addition to the versions outlined above, a direct velocity coupling that inserts the Lagrangian velocity into the Eulerian solution was tested. This variant of the algorithm was dropped as it did not always deliver physical solutions. The results presented in §4 are presented for **V3** using either the **V3-nodes** or the **V3-quadrature** variants.

The following subsections present the details of the coupled Lagrangian-Eulerian solution algorithm. In general, the overall algorithm flow follows the modified immersed finite element method of Wang and Zhang [5]. Extensions to the base algorithm are outlined in §3.3 – 3.12. Section 3.3 explains the additional steps required to obtain a stable time-step estimate when coupling to an explicit multimaterial Eulerian solver. The changes required to account for the added-mass effect, typical in coupled fluid-solid interaction algorithms, is explained in §3.5. The use of the Lagrangian volume-fraction in the calculation of the modified Eulerian mass matrix is detailed in §3.6. The overlap conditions, and associated Lagrangian volume-fraction used in the Eulerian coupling mass matrix are outlined in §3.7. Considerations for the use of the

uniform-strain element found in many explicit Lagrangian solid dynamics codes are presented in §3.9. The use of penalty enforcement of velocity continuity between the Eulerian and Lagrangian domains is outlined in §3.10 – 3.11.

Finally, because SABLE is a multimaterial Eulerian code, it uses a geometrical material insertion algorithm to represent multiple physical parts in the physical problem. Each material occupies a non-overlapping volume of the computational domain, including void material which occupies space but does not have mass, pressure, temperature, etc. The setup of coupled problems requires making choices about the Eulerian material in the region of overlap with the Lagrangian domain. There are multiple valid choices for the material in the Eulerian overlap region that include: (a) a void material, (b) a material matched to the material properties of the Lagrangian material, and (c) a material that is not matched to the Lagrangian material, e.g., an ideal gas. The extensions required for handling the coupling velocity in Eulerian regions that contain a void material and overlap with the Lagrangian domain is presented in §3.12. The various background material choices are also considered in §4 for a number of prototypical coupled Lagrangian-Eulerian problems.

3.1. Definitions

The following definitions are used for the quantities involved in the coupling algorithm.

- Binary indicator:

$$\phi = \begin{cases} 0 \; if \; no \; intersection \; between \; meshes \\ 1 \; if \; intersection \; between \; meshes \end{cases} \tag{18}$$

  Additional details on the how the indicator is computed and used may be found in §3.7.

- Eulerian material volume fraction:

$$\mathcal{F}^E = \sum_{\alpha=1}^{Nmat} \mathcal{F}^\alpha \tag{19}$$

  The Eulerian material volume fraction represents the total volume of all material contained in an Eulerian element. The volume fraction for a given material α in an Eulerian element is

$$\mathcal{F}^\alpha = \frac{V^\alpha}{V^E} \tag{20}$$

  where the material occupies a volume V^α, and V^E is the total volume of the element. Figure shows a prototypical Eulerian element containing multiple materials including void. A void material occupies part of the element volume, but represents empty space in the element. Void material does not carry any thermodynamic properties, i.e., density and internal energy, and it's pressure is zero. Figure 3-1 shows a prototypical multimaterial Eulerian element and the associated volume fraction for each material.

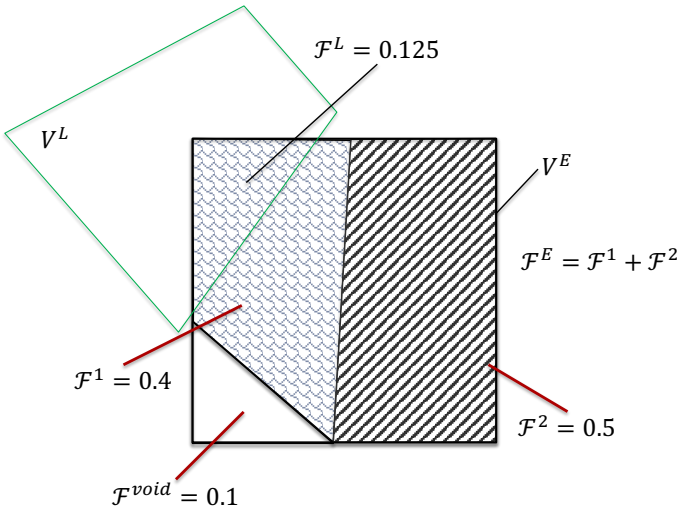

Figure 3-1 Multiple materials contained in an Eulerian element with an overlapping Lagrangian element. The void volume fraction is reserved as material 0, and the material volume fraction is $\mathcal{F}^E = \mathcal{F}^1 + \mathcal{F}^2$.

- Lagrangian volume fraction:

$$\mathcal{F}^L = \frac{\sum_k V_k}{V^E} \tag{21}$$

where k ranges over all elements that intersect the Eulerian volume, and V_k are the associated overlapping volumes for each Lagrangian element as shown in Figure 3-2. The overlapping Lagrangian volume represented on a given Eulerian element is

$$V^L = \sum_k V_k \tag{22}$$

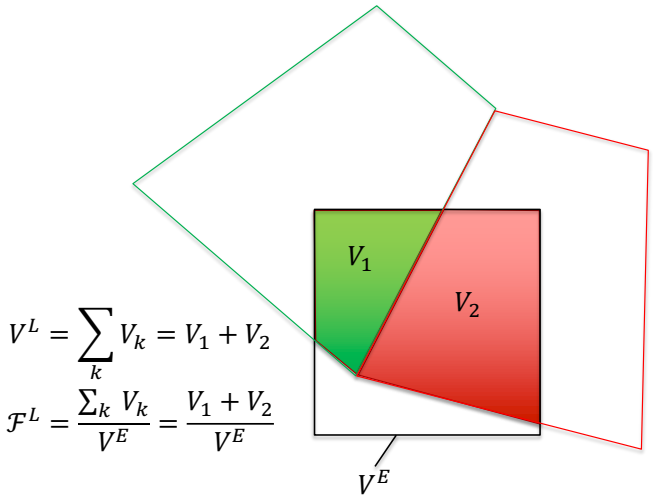

Figure 3-2 Lagrangian elements overlapping the Eulerian element, and the associated intersection volumes V_1 and V_2 used used for the Lagrangian volume fraction calculation.

- Average Eulerian Stress: The volume-fraction averaged Eulerian stress is used in the residual calculation for the coupling forces.

$$\boldsymbol{\sigma}^E = \sum_{\alpha=1}^{Nmat} \mathcal{F}^\alpha \boldsymbol{\sigma}^\alpha \tag{23}$$

- Average Eulerian Material Stress: The average Eulerian material stress accounts for the volume occupied by real materials carrying stress, i.e., the volume of the element less the volume occupied by void. In addition, the stress and volume for any background material in the Lagrangian-Eulerian overlap region can optionally be removed. This stress field is used exclusively for computing the Lagrangian traction forces at the wetted Lagrangian-Eulerian interface.

$$\overline{\boldsymbol{\sigma}}^E = \frac{\sum_{\alpha=1}^{Nmat} \mathcal{F}^\alpha \boldsymbol{\sigma}^\alpha}{\sum_{\alpha=1}^{Nmat} \mathcal{F}^\alpha} \quad \alpha \neq \textit{Background Material Id} \tag{24}$$

- Average Eulerian Density:

$$\rho^E = \sum_{\alpha=1}^{Nmat} \mathcal{F}^\alpha \rho^\alpha \tag{25}$$

- Average Lagrangian Density:

$$\rho^L = \frac{\sum_k \rho_k V_k}{V^L} \tag{26}$$

where k ranges over all elements that overlap the Eulerian element, and V_k is the associated overlapping volume for each Lagrangian element as shown in Figure 3-3.

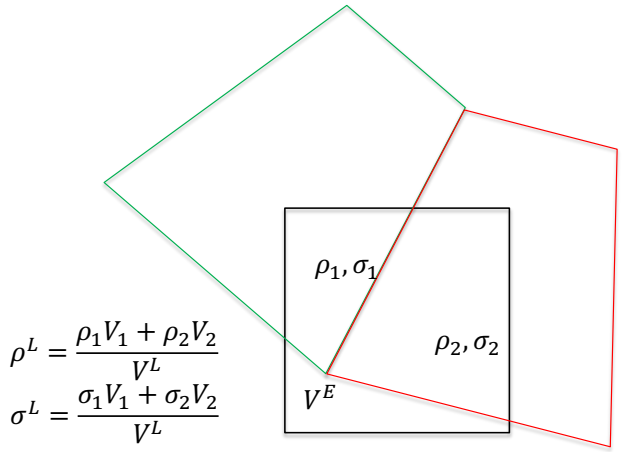

Figure 3-3 Lagrangian elements overlapping the Eulerian element and the associated density (ρ_1, ρ_2) and stress (σ_1, σ_2) used to compute the average Lagrangian density and stress on the Eulerian element.

- Average Lagrangian Stress:

$$\boldsymbol{\sigma}^L = \frac{\sum_k \boldsymbol{\sigma}_k V_k}{V^L} \tag{27}$$

where k ranges over all elements that intersect the Eulerian volume, and V_k is the associated intersecting volume as shown in Figure 3-3.

3.2. Data Flow

The data computed and transferred between SABLE and OpenIFEM are presented in Table 3-2. Here, the primary algorithmic steps are identified with the associated function calls. Additional communications will be required for the "man-in-the-middle" model with a stand-alone coupling application.

A brief summary of the grid transfer operations required for implementation of an independent code-coupling application is shown in Table 3-1. Here, the overlap type calculations require finding the overlap volume for Lagrangian elements on the Eulerian mesh. The interpolation using shape functions implies an element location step followed by a solve for the element's natural coordinates ($\boldsymbol{\xi}$) and subsequent shape function evaluation.

Grid Transfer Calculation	From $\rightarrow$ To	Usage
Overlap	L $\rightarrow$ E	$\mathcal{F}^L$, ρ^L, $\boldsymbol{\sigma}^L$, C^L_{wave}
Indicator Update	L $\rightarrow$ E	Coupling forces
Interpolate w. Shape Functions	L $\rightarrow$ E	$\boldsymbol{v}^L$, $\boldsymbol{a}^L$
Element in Eulerian Mesh	E $\rightarrow$ L	Lagrangian traction force
Interpolate w. Shape Functions	E $\rightarrow$ L	Added mass

Table 3-1 Grid transfer operations (L: Lagrangian, E: Eulerian).

SABLE	Communication	OpenIFEM
Client.C		**Test Code cpp file**
run()		main()
Send_OIFEM_Geom()		
$(x_{min}, y_{min}, z_{min})$	Global Max $\longrightarrow$	$(x_{min}, y_{min}, z_{min})$
Δx	Global Max $\longrightarrow$	Δx
Nel_{1D}	Global Max $\longrightarrow$	Nel_{1D}
Client.C		**openifem_sable_fsi.cpp**
Run_step()		run()
Send_dt()		
Δt	Global Max $\longrightarrow$	Δt
str_solid_dynamics.C		**sable_wrapper.cpp**
Calculate_OIFEM_Coupling_Force()		rec_stress()
$\boldsymbol{\sigma}^E$	send/recv $\longrightarrow$	$\boldsymbol{\sigma}^E$
$\overline{\boldsymbol{\sigma}}^E$	send/recv $\longrightarrow$	$\overline{\boldsymbol{\sigma}}^E$
		rec_vf
$\mathcal{F}^E$	send/recv $\longrightarrow$	$\mathcal{F}^E$
$\overline{\rho}^E$	send/recv $\longrightarrow$	$\overline{\rho}^E$
		rec_velocity
$\boldsymbol{v}^E$	send/recv $\longrightarrow$	$\boldsymbol{v}^E$
str_solid_dynamics.C		**openifem_sable_fsi.cpp**
Solve_Balance_Equations()		
		find_solid_bc(): $\boldsymbol{F}^{ext}$ on Lagrangian mesh
		solid_solver.run_one_step()
		update_indicator() or update_indicator_qpoints()
		find_fluid_bc(): $\Delta \boldsymbol{F}_{acc}$, $\Delta \boldsymbol{F}_{\sigma}$
Receive_OIFEM_vars()		sable_solver.send_fsi_force()
$\boldsymbol{F}_{fsi}$	$\longleftarrow$ send/recv	$\Delta \boldsymbol{F}_{acc} + \Delta \boldsymbol{F}_{\sigma}$
$\boldsymbol{v}^L$	$\longleftarrow$ send/recv	$\boldsymbol{v}^L$
		sable_solver.send_indicator()
ρ^L	$\longleftarrow$ send/recv	ρ^L
$\mathcal{F}^L$	$\longleftarrow$ send/recv	$\mathcal{F}^L$
ϕ	$\longleftarrow$ send/recv	ϕ
Remainder of SABLE Time Step		

Table 3-2 Algorithmic flow, communication steps and data flow. function() indicates a fixed algorithmic step in the respective solvers.

3.3. Stable Time-Step

For the current work with OpenIFEM, the stable time-step estimate from SABLE controls the overall time-step since the OpenIFEM Lagrangian solver is unconditionally stable. However, the use of void where the Lagrangian material resides causes SABLE to estimate the stable time-step based only on the wave-speeds of materials in the Eulerian model. Due to the coupling algorithm, it is necessary to account for the wave-speed of the Lagrangian material on the Eulerian mesh in order to estimate the time-step. Thus, for problems where void is used in the Eulerian model where the Lagrangian material resides, it is necessary to scale the time-step based on the Lagrangian material wave speed.

By default, SABLE uses a time-step scale factor, $\alpha = 0.85$, where the stable time-step based on the minimum of stable time step estimates based on sound-speed, elastic wave speed, material velocity, artificial viscosity, and volume change.

$$\Delta t = \min(\Delta t_{sound}, \Delta t_{elastic}, \Delta t_{matvel}, \Delta t_{Q}, \Delta t_{volume}) \tag{28}$$

For coupled problems, when an Eulerian material with a sound-speed different than the Lagrangian material in the overlap region is used, it is necessary to account for the differences in wave speed. For example, when air is used in the overlap region, and the Lagrangian material is steel, it is necessary to scale the time-step accordingly for OPENIFEM – SABLE calculations. Using wave speeds for the Lagrangian and Eulerian materials, a second scale factor can be estimated as

$$\beta = min(1.0, \frac{\Delta t^L}{\Delta t^E}) = min(1.0, \frac{C^E_{wave}}{C^L_{wave}}) \tag{29}$$

This scale factor multiples the default value for α, i.e.,

$$\alpha = \beta\ 0.85 \tag{30}$$

For overlap regions with void in the Eulerian mesh, the limiting (maximum) wave speed for all Eulerian material is used for C^E_{wave}. This adjustment is made where necessary for the computations presented in §4.

For coupling with an explicit Lagrangian solver, the stable time-step calculation will require additional steps.

1. Transfer average wave speeds from the Lagrangian solver for overlapping elements that contain void in the Eulerian mesh

$$\overline{C}^L_{wave} = \frac{\sum_k C^L_k V_k}{V^L} \tag{31}$$

   where k ranges over all elements that intersect the Eulerian volume, C^L_k is the Lagrangian material wave speed, and V_k is the intersection volume, e.g., see Figure 3-3

2. Compute a minimum time-step on the Eulerian mesh in overlapping elements

$$\Delta t^{overlap} = \alpha \frac{h}{\overline{C}^L_{wave}} \tag{32}$$

   where h is the element size on a structured block.

3. Exchange the Lagrangian and Eulerian time step estimates
4. Take a minimum of the Lagrangian Δt^L, Eulerian Δt^E, and overlap $\Delta t^{overlap}$ time steps
5. Broadcast the final time-step to Eulerian and Lagrangian solvers for the next time-step

3.4. Lagrangian Traction Forces

The calculation of the Lagrangian traction forces (in OpenIFEM find_solid_bc()) requires point location in the Eulerian mesh, and evaluation of the Eulerian stress at that point with the necessary numerical integration over the surface of the Lagrangian mesh. This requires that the Eulerian stresses be passed to the Lagrangian code. The quadrature points on the surface of the Lagrangian mesh are used to define the point location used for the stress interpolation as shown in Figure 3-4. For the uniform-strain element, typical in explicit Lagrangian codes, this can be viewed as simply locating the Eulerian element containing the Lagrangian surface quadrature point and using the volume-fraction averaged Eulerian stress for the element to compute the traction. The centering of the stress in the Eulerian mesh, is at the element centroid. That is, the Eulerian stress is an average stress over the element. Testing has shown that lifting the Eulerian to the stress and then interpolating at quadrature points on the Lagrangian surface didn't offer any significant advantages in terms of accuracy when ratio of the Lagrangian mesh size to the Eulerian mesh spacing is one or less.

$$\boldsymbol{F}_I^{ext} = \int_{\Gamma^e} N_I \overline{\boldsymbol{\sigma}}^E \cdot \boldsymbol{n} d\Gamma \tag{33}$$

Here, the surface integration is performed over the Lagrangian surface, and $I \in 1, Nnpe$ where $Nnpe$ is the number of nodes per Lagrangian surface element. Testing has shown that a 2-point quadrature rule in 2-D (4-point rule in 3-D) is sufficient for the coupled problems tested in this work. For highly refined Eulerian elements, relative to the Lagrangian mesh size, higher-order quadrature rules may be required to adequately sample the stress distribution in the Eulerian mesh.

When a background material, matched to the Lagrangian body, is used in the Eulerian model, care must be taken to avoid problems due to a mismatch between the boundary of the background material and the Lagrangian body. For this reason, the stress contribution due to the background material in SABLE can be removed from the average Eulerian stress used for the traction calculation. See Eq. (24) and Appendix A for the SABLE *bgmat* keyword.

In some limiting cases, a normal extension of the Lagrangian surface is required in order to identify the correct Eulerian element for the traction calculation. In this case, the location of the Eulerian stress is identified using a normal offset $\beta\Delta x$ as shown in Figure 3-5. By default, $\beta = 0$, and is only specified for limiting cases, e.g., aligned Lagrangian/Eulerian meshes where void is used in the region occupied by the Lagrangian mesh. A good initial choice is $\beta = 0.01$ or 1% of the Eulerian mesh spacing. See Appendix B for the OpenIFEM keyword used to specify the normal offset parameter β.

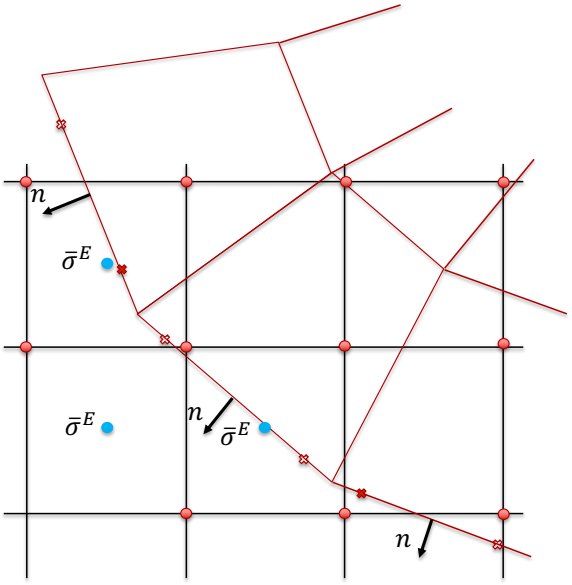

Figure 3-4 Overlapping Lagrangian and Eulerian elements used to compute the traction forces on the Lagrangian body. Surface quadrature points are indicated by x, Eulerian nodes by •, and Eulerian centroids by •.

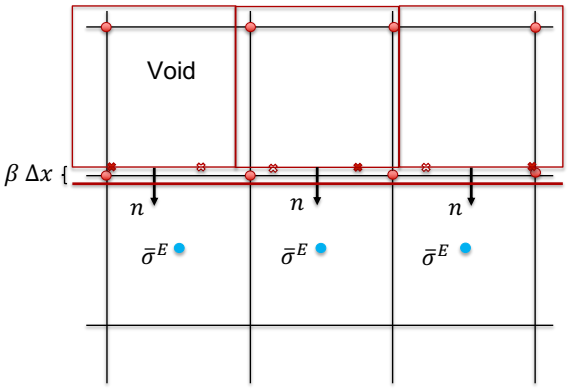

Figure 3-5 Normal offset for traction integration. Surface quadrature points are indicated by x, Eulerian nodes by •, and Eulerian centroids by •

3.5. Lagrangian Boundary Added-Mass

The so-called "added-mass" effect refers to the influence of the Eulerian mass on the motion of a Lagrangian body moving through the Eulerian domain. The added-mass term is typically added at the "wetted" surface of the Lagrangian body, and in a discrete sense is added to the Lagrangian nodal mass,

In this work, the added-mass term is approximated by interpolating the Eulerian nodal mass (not the coupling nodal mass) to the nodes of the overlapping Lagrangian mesh. This is shown schematically in Figure 3-6.

This computation requires the inverse solution of the expansion of the Eulerian nodal coordinates using the known Lagrangian coordinate in order to find the element's natural coordinates, i.e., $\boldsymbol{\xi}$.

This is a well-known process, can be implemented in closed-form for 2D quadrilateral mesh, and is only sketched out here.

Given a Lagrangian coordinate, $\boldsymbol{x}^L$, and expanding the nodal coordinates in terms of the Eulerian shape functions,

$$\boldsymbol{x}^L = \sum_{I=1}^{Nnpe} N_I \boldsymbol{x}_I^E \tag{34}$$

solve for the element natural coordinates. Armed with the natural coordinates, evaluate the Eulerian lumped mass at the intersection point, i.e.,

$$M_L^E|_{\boldsymbol{\xi}} = \sum_{I=1}^{Nnpe} N_I|_{\boldsymbol{\xi}} M_{L_I}^E \tag{35}$$

At each node I on the boundary of the Lagrangian mesh, where there is overlap with the Eulerian mesh, the Lagrangian lumped mass is augmented by the interpolated Eulerian lumped mass as

$$\tilde{M}_{L_I}^L = M_{L_I}^L + M_L^E|_{\boldsymbol{\xi}} \tag{36}$$

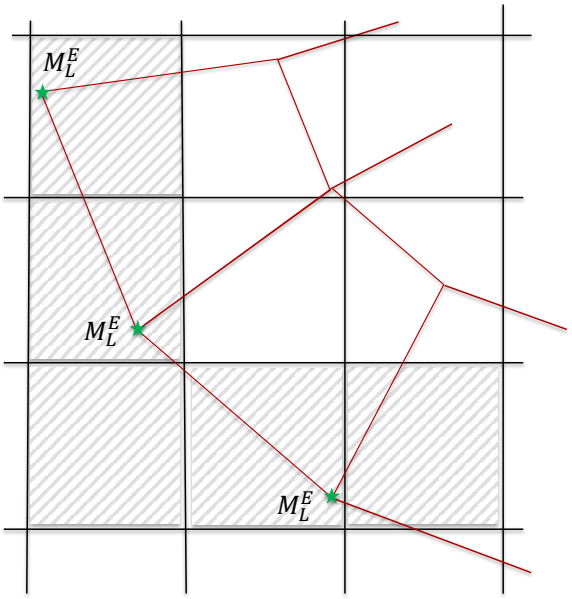

Figure 3-6 Interpolation of the Eulerian nodal mass at the nodes of the overlapping Lagrangian mesh.

3.6. Eulerian Coupling Nodal Mass

The Eulerian coupling nodal mass incorporates the effects of the Lagrangian body in the overlap region into the Eulerian mesh for the SABLE Lagrangian step. This step makes use of the Lagrangian volume fraction on the Eulerian mesh in overlap regions.

The density used to compute the coupling node mass is

$$\overline{\rho} = (1.0 - \mathcal{F}^L)\rho^E + \mathcal{F}^L \rho^L \tag{37}$$

where ρ^L is the average Lagrangian density in the Eulerian element in Eq. (26), and ρ^E is the average Eulerian density in Eq. (25).

The row-sum lumped coupling nodal mass at node I of an Eulerian element in the overlap region is computed as

$$\tilde{M}_{L_I} = \frac{1}{Nnpe}\overline{\rho}V^E \tag{38}$$

for linear finite elements.

The effect of using the coupling nodal mass is shown in Figure 3-7 with a prototypical penetrator-target geometry, the target lumped mass, and the coupling nodal mass. In effect, using the coupling nodal mass in Eq. (44) builds the Lagrangian penetrator mass into the Eulerian model, and is used during the SABLE Lagrangian step. Note that this is also the case when a background material resides where the Lagrangian penetrator overlaps with the Eulerian mesh.

At this point, it is important to note that the SABLE multimaterial formulation enforces a strict partition of unity for the material volume fractions in a given element.

$$\sum_{\alpha=1}^{Nmat} \mathcal{F}^{\alpha} = 1 \tag{39}$$

In overlap regions, this is not strictly enforced when Lagrangian material is present, i.e.,

$$\mathcal{F}^L + \sum_{\alpha=1}^{Nmat} \mathcal{F}^{\alpha} \neq 1 \tag{40}$$

Therefore, it is possible for Eulerian material and Lagrangian material to overlap to varying degrees. This is resolved for the the element and nodal mass using the definition of $\overline{\rho}$ in Eq. (37). The implications of overlap and partition of unity for the remap algorithm are discussed further in §3.14.

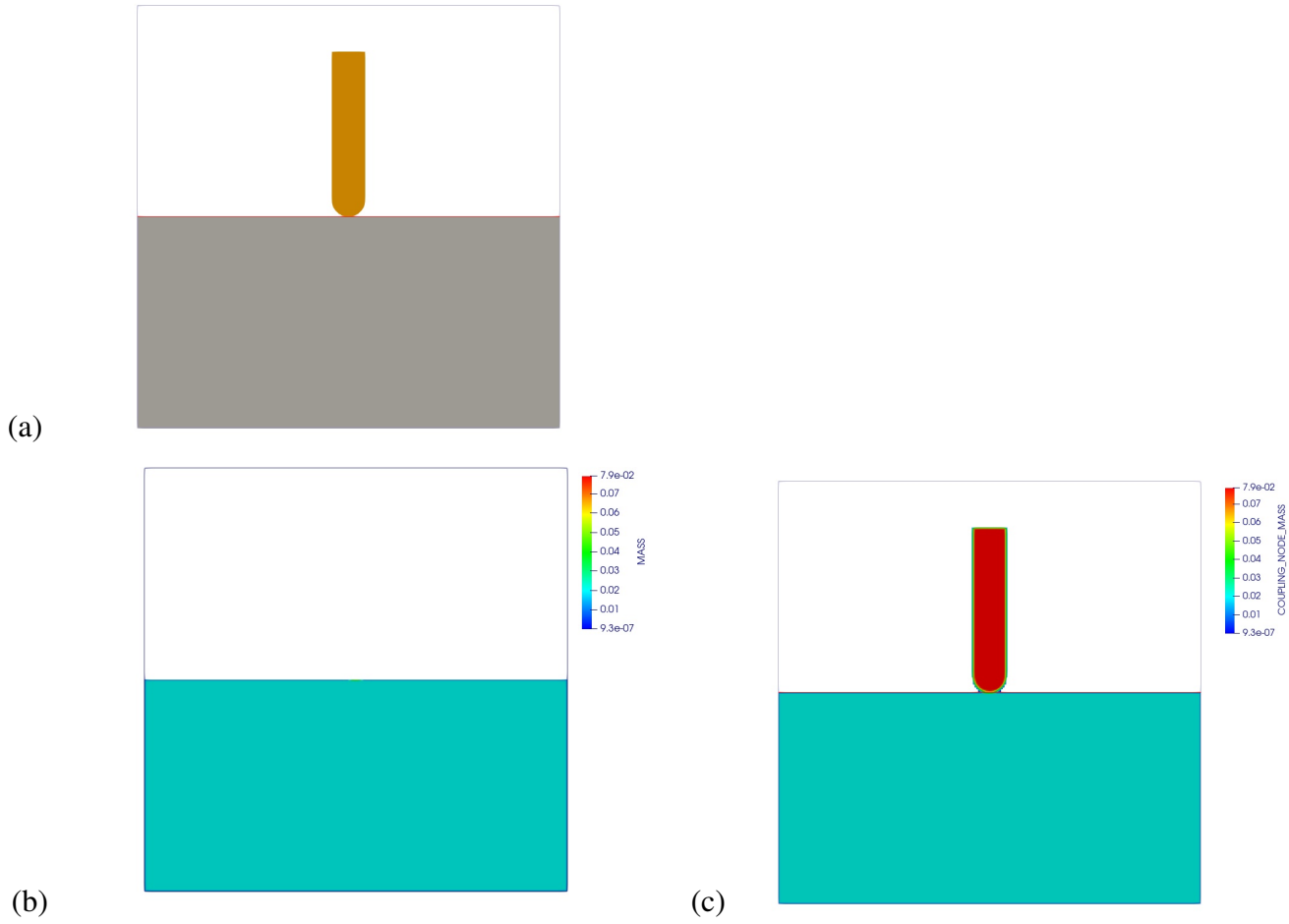

Figure 3-7 Penetrator-target model with void where the Lagrangian penetrator resides in the Eulerian mesh: (a) penetrator-target geometry, (b) Eulerian lumped mass for the target, (c) coupling lumped mass on the Eulerian mesh.

3.7. Overlap Indicator Update

The overlap indicator ϕ is used to identify those nodes and elements that overlap between the Lagrangian and Eulerian meshes. In addition, the indicator is used in the formation of the residual coupling forces.

The indicator field is defined at the element-level on the Eulerian mesh. There are two types of the indicator that have been tested, a node-based indicator and a quadrature-point indicator. Each of these has been assessed testing for all nodes/quadrature-points to be "completely inside", or "partially inside" the overlap region. Figure 3-8 shows the two overlap modes.

The "completely inside" model requires that all nodes of the element for the node-based indicator, or alternatively all quadrature points in the element for the quadrature-point indicator, be contained inside the Lagrangian mesh. In this case, the indicator is essentially binary with $\phi = 1$ when all points are inside the Lagrangian mesh, and $\phi = 0$ otherwise.

The "partially inside" model counts the number of nodes/quadrature points that are inside the Lagrangian mesh. The indicator value is then estimated based on the ratio of the number of points inside the Lagrangian mesh to the total number of points in the element. This provides discrete values of the indicator with $0 \leq \phi \leq 1$. To date, the partially inside model has not shown significant improvements relative to the completely inside model, and is not currently being pursued.

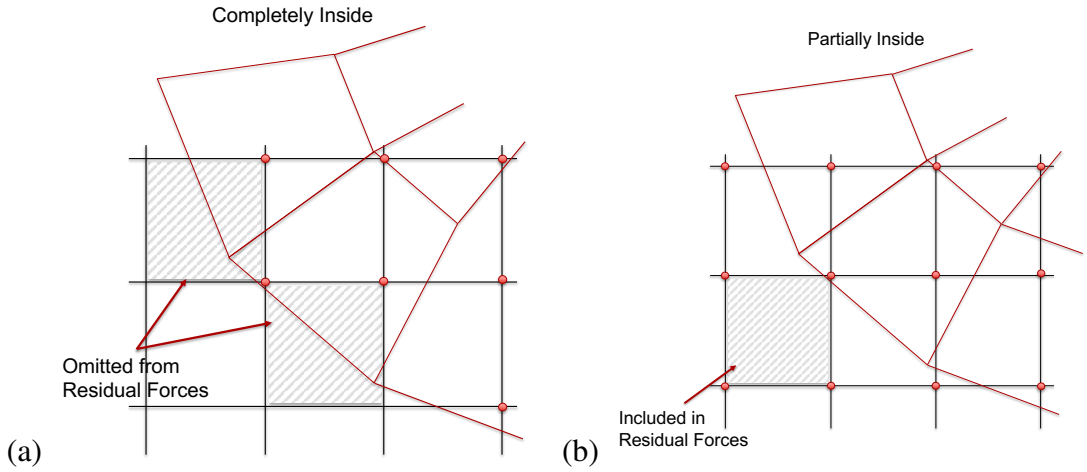

Figure 3-8 Overlap models: (a) completely inside, and (b) partially inside.

The node-based indicator uses an inside/outside test at the nodes of an Eulerian element to decide if it overlaps with the Lagrangian domain. Figure 3-9(a) shows the elements in blue where $\phi = 1$ for the completely-inside model.

The quadrature-point based indicator uses the location of the quadrature points in an element to determine if the element overlaps with the Lagrangian domain. This is shown schematically in Figure 3-9(b) where the blue elements correspond to $\phi = 1$. The quadrature points are indicated by a blue star ($\star$). The quadrature-point based indicator provides a more accurate indication of overlap elements relative to the node-based scheme, but at an increased cost. The computational

complexity scales as the number of quadrature points. Thus, the quadrature rule may vary, with more points (a higher-order quadrature rule) providing a sharper indicator, but with an increase in computational cost for the inside-outside tests.

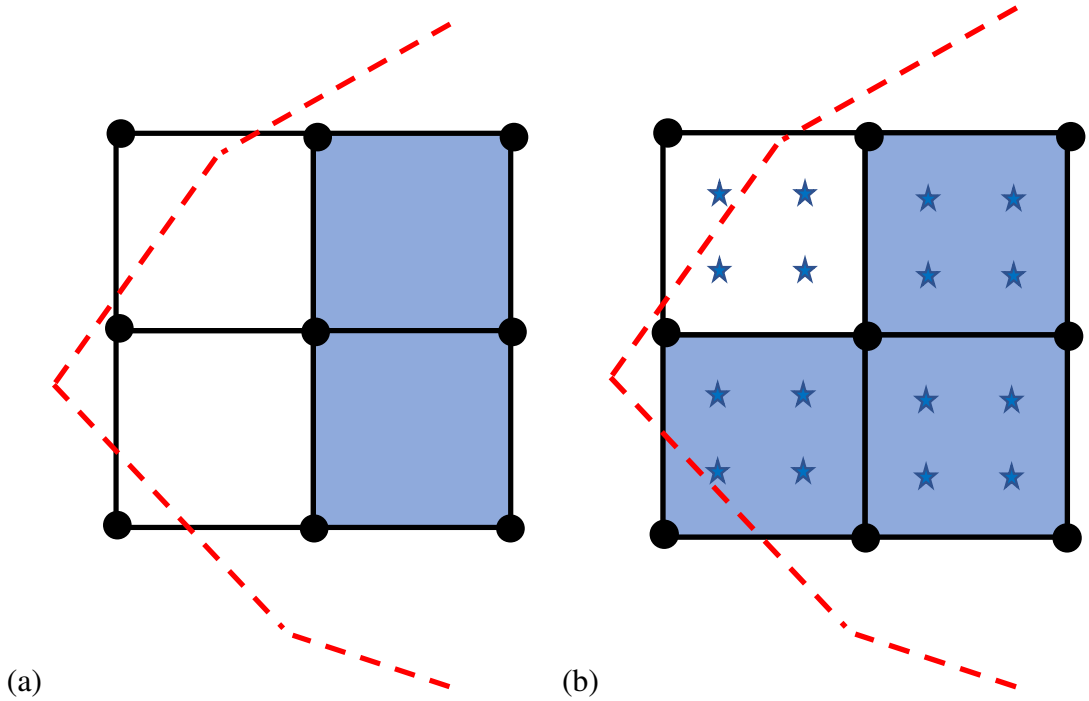

Figure 3-9 Indicator criteria: (a) node-based, and (b) quadrature-point based for completely-inside model. $\phi = 1$ **for the elements filled in blue.**

The indicator field is used for several different parts of the coupling algorithm. The indicator determines if forces will be calculated for a given Eulerian element. Using Eq. (9), this can be written as

$$f_i^{\text{int}} = \phi \left\{ \rho^{\text{L}} \left(\frac{\text{D}v_i^{\text{E}}}{\text{D}t} - \frac{\text{D}v_i^{\text{L}}}{\text{D}t} \right) + (\sigma_{ij,j}^{\text{L}} - \sigma_{ij,j}^{\text{E}}) \right\} \tag{41}$$

where

$$\phi = \begin{cases} 0 \; for \; non-overlapping \; elements \; outside \; \overline{\Omega} \\ 1 \; for \; overlapping \; elements \; in \; \overline{\Omega} \end{cases} \tag{42}$$

The indicator field is also used to identify any nodes in the overlap region that may enter into the velocity-reset algorithm (see §3.12). In this use case, all nodes attached to an element where $\phi = 1$ will be marked for velocity updates in when the velocity-reset algorithm active.

3.7.1. Lagrangian Volume Fraction

During the overlap indicator update, the Lagrangian volume fraction is updated for the current configuration of the Lagrangian mesh relative to the Eulerian mesh. The Lagrangian overlap denoted as a volume fraction, $\mathcal{F}^{\text{L}}$, provides an accurate percentage of the Lagrangian overlap for a given Eulerian cell. It is used to calculate the modified density for the Eulerian domain given by

Eq. (6), and may be used as in the future as a constraint on the material remap procedure in SABLE. More accurate value of the Lagrangian volume fraction, that is overlap volume, improves the interface location and solution on the Eulerian domain.

To calculate the Lagrangian overlap for a particular Eulerian cell, first we check if the cell is outside or completely inside (all the nodes of the Eulerian cell) in the Lagrangian solid. For these situations the Lagrangian volume fraction $\mathcal{F}^{\mathrm{L}}$ is assigned to be 0 or 1 respectively. If the cell is partially covered by the Lagrangian solid then the percentage of overlap by each Lagrangian cell is calculated separately using Algorithm 2. This process is schematically represented in Figure 3-10.

For future efforts, it would be advisable for the overlap calculation to be integrated with the Lagrangian volume fraction calculation using diatom.

Algorithm 2: Algorithm for calculation of Lagrangian overlap $\mathcal{F}^{\mathrm{L}}$.

Mesh parameters: number of Eulerian cells (n^{E}), number of Lagrangian cells (n^{L});
Eulerian cell size: h;
Eulerian cell upper and lower corner: $(u^{\mathrm{E}}, l^{\mathrm{E}})$;
for *Eulerian cells* $i = 0$ *to* n^E **do**
  Initialize $\mathcal{F}^{\mathrm{L}} = 0$;
  for *Lagrangian cells* $j = 0$ *to* n^L **do**
    (1) Get bounding box for the jth Lagrangian cell: lower corner (l^{L}) and upper corner (u^{L});
    (2) Get coordinates of the intersection box between the ith Eulerian cell and jth Lagrangian cell as follows:
    Lower corner$(l^{\mathrm{i}}) : max(l^{\mathrm{L}}, l^{\mathrm{E}})$, Upper corner$(u^{\mathrm{i}}) : min(u^{\mathrm{L}}, u^{\mathrm{E}})$;
    (3) Sample equally spaced points in the intersection box with distance $0.01h$ starting from (l^{i}) and (u^{i}) ;
    (4) Calculate number of points inside the jth Lagrangian cell (inside_cell);
    (5) Contribution to the $\mathcal{F}^{\mathrm{L}}$ from jth Lagrangian cell is:
    $\mathcal{F}^{\mathrm{L}} += \frac{\text{Area(intersection box)}}{\text{Area(Eulerian cell)}} \frac{\text{inside\_cell}}{\text{total no. of samples}}$
  end
end

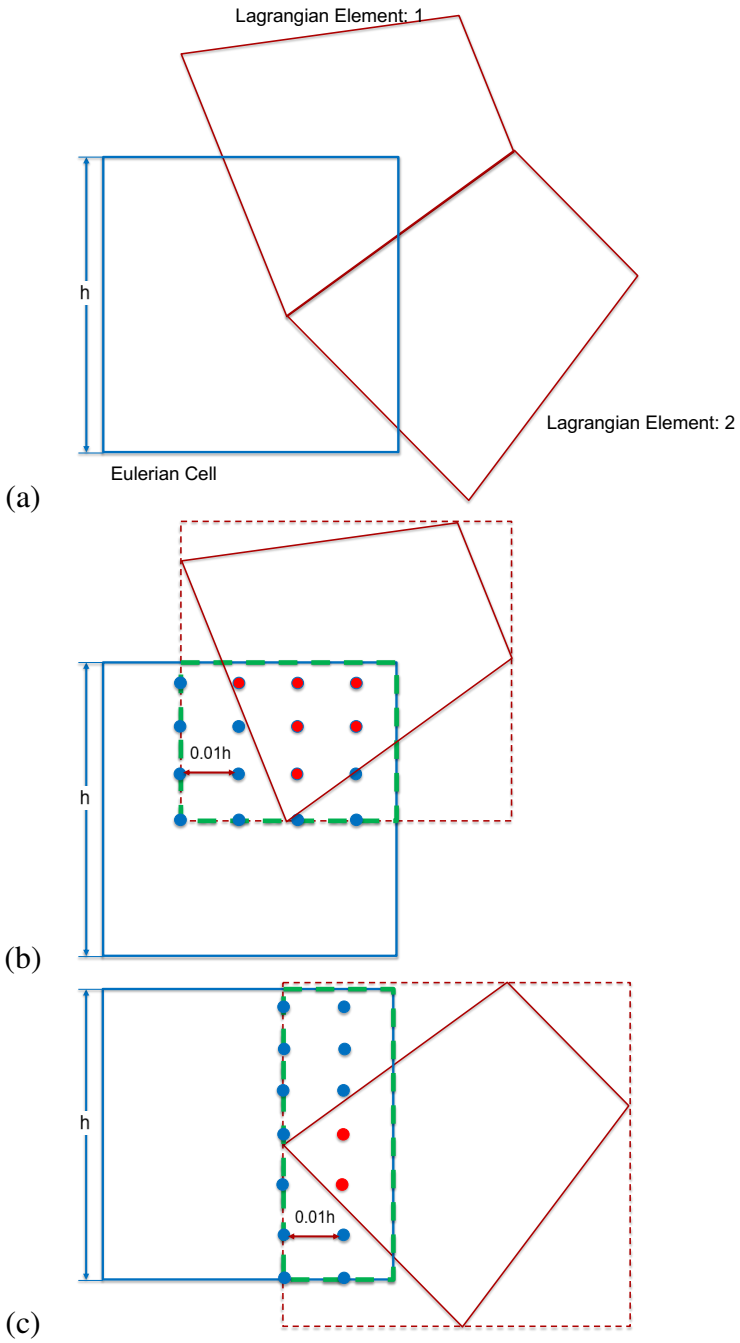

Figure 3-10 Schematic representation of Lagrangian overlap calculation (a) overlap geometry, (b) calculation for Lagrangian element:1, (c) calculation for Lagrangian element:2.

3.8. Eulerian Coupling Forces

The coupling forces, computed in OpenIFEM on the Eulerian mesh, appear as external forces in SABLE's Lagrangian step,

$$M_L^E \boldsymbol{a}^E = \boldsymbol{F}^{ext} - \boldsymbol{F}^{int} \tag{43}$$

where M_L^E is the lumped mass matrix, and $\boldsymbol{F}^{int}$ includes contributions from the stress-divergence, hourglass stabilization forces and artificial viscosity.

The coupling forces are assembled into the external forces as

$$\boldsymbol{F}^{ext} = \Delta \boldsymbol{F}_{acc} + \Delta F_{\sigma} \tag{44}$$

The acceleration coupling force, $\Delta \boldsymbol{F}_{acc}$, relies on a residual between the accelerations computed on the Eulerian nodes, and those on the Lagrangian mesh interpolated to the Eulerian nodes. The Eulerian acceleration is approximated as

$$\tilde{\boldsymbol{a}}^E = \frac{D\boldsymbol{v}^E}{Dt} \approx \frac{\boldsymbol{v}^L - \boldsymbol{v}^E}{\Delta t_{mid}} + \boldsymbol{v}^E \cdot \nabla \boldsymbol{v}^E \tag{45}$$

where Δt_{mid} is the mid-step time step from SABLE based on the stable time-step estimates. The Lagrangian velocity is interpolated from the Lagrangian mesh to the nodes of the Eulerian mesh in overlap regions as shown in Figure 3-11. The nodal interpolation procedure relies on the Lagrangian shape functions, N_I^L, and identification of the overlapping Lagrangian element with a given Eulerian node. Similar to the interpolation of the Eulerian lumped mass to the boundary nodes of the Lagrangian mesh, an inverse problem for the natural coordinates of the Lagrangian elements where Eulerian nodes reside is required. Once the natural coordinates are known, the values of the Lagrangian acceleration and velocity may be interpolated for use at the Eulerian nodes.

With the Eulerian velocity and the Lagrangian acceleration and velocity aligned on the Eulerian mesh, the Eulerian acceleration can be computed and expanded in terms of the Eulerian shape functions

$$\boldsymbol{a}^E = \sum_{J=1}^{Nnpe} N_J^E \boldsymbol{a}_J^E \tag{46}$$

where $Nnpe$ is the number of nodes per element. On the Eulerian mesh, the interpolated Lagrangian acceleration can also be expanded in terms of the Eulerian shape functions which is convenient for the subsequent numerical integration.

$$\boldsymbol{a}^L = \sum_{J=1}^{Nnpe} N_J^E \boldsymbol{a}_J^L \tag{47}$$

For node I of an Eulerian element in the overlap region, the force due to a residual in the accelerations is

$$\Delta \boldsymbol{F}_{acc_I} = \sum_{k=1}^{Nqpt} N_I^E \bar{\rho} \phi_k \left[\sum_{J=1}^{Nnpe} N_J^E \boldsymbol{a}_J^E - \sum_{J=1}^{Nnpe} N_J^E \boldsymbol{a}_J^L \right] w_k |J|_k \tag{48}$$

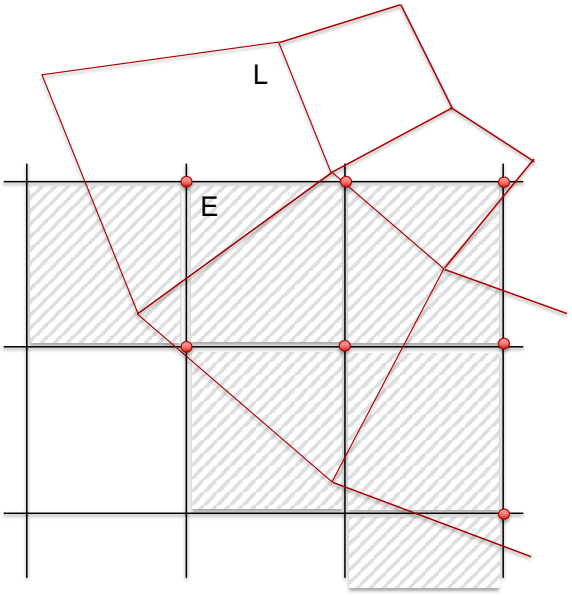

Figure 3-11 Interpolation of Lagrangian nodal values to Eulerian nodes in overlap regions.

where $Nqpt$ is the number of Guassian quadrature points, w_k is the Gaussian weight, $|J|_k$ is the determinant of the Jacobian at each quadrature point, k, and $\overline{\rho}$ is computed using Eq. (37).

The force due to the stress residual is

$$\Delta \boldsymbol{F}_{\sigma_I} = \sum_{k=1}^{Nqpt} \nabla N_I^E \phi_k \left[\boldsymbol{\sigma}^E - \boldsymbol{\sigma}^L\right] w_k |J|_k \tag{49}$$

Similar to the nodal interpolation, the Lagrangian stress is interpolated/projected onto the Eulerian mesh to obtain a consistent centering for both stresses that may be used in the numerical integration. The indicator, ϕ_k, may be either based on the nodes of an Eulerian element, or the quadrature points depending on the overlap indicator selected – see §3.7.

3.9. Uniform Strain Elements

We briefly turn attention to the use of the uniform-strain elements (see [2], used in SABLE and commonly used in explicit Lagrangian codes. Starting with Eq. (48), and row-sum lumping terms, yields

$$\Delta \boldsymbol{F}_{acc} = \tilde{M}_L(\tilde{\boldsymbol{a}}^E - \boldsymbol{a}^L) \tag{50}$$

where the row-sum lumping procedure yields a lumped mass matrix

$$\tilde{M}_{L_I} = \frac{1}{Nnpe}\overline{\rho} V^E \tag{51}$$

I is the local element node number, and V^E is the Eulerian element volume.

Using the well-known $\boldsymbol{B}$ matrix, the force due to the stress residual becomes

$$\Delta \boldsymbol{F}_{\sigma} = \boldsymbol{B}^T (\boldsymbol{\sigma}^E - \boldsymbol{\sigma}^L) \tag{52}$$

where the indicator $\phi_k = 1$ is used at the element centroid. Alternatively, this may be written as

$$\Delta \boldsymbol{F}_{\sigma} = \boldsymbol{F}^{int^E} - \boldsymbol{F}^{int^L} \tag{53}$$

Here, the internal force vectors do not include artificial viscosity or hourglass stabilization terms.

Combining terms, the coupling force terms may be written as

$$\Delta \boldsymbol{F}_{acc} + \Delta \boldsymbol{F}_{\sigma} = (\tilde{M}_L \tilde{\boldsymbol{a}}^E + \boldsymbol{F}^{int^E}) - (\tilde{M}_L \boldsymbol{a}^L + \boldsymbol{F}^{int^L}) \tag{54}$$

This form of the coupling forces provides a more intuitive view of the discrete formulation, and provides additional insights into the behavior of the coupled algorithm. For example, using this form of the coupling terms in Eq. (44) with the coupling nodal mass yields

$$\tilde{M}_L^E \boldsymbol{a}^E = (\tilde{M}_L \tilde{\boldsymbol{a}}^E + \boldsymbol{F}^{int^E}) - (\tilde{M}_L \boldsymbol{a}^L + \boldsymbol{F}^{int^L}) - \boldsymbol{F}^{int^E} \tag{55}$$

Finally, for implementation using SABLE and an explicit Lagrangian solver, it may be necessary to weight the external forces presented to SABLE using the Lagrangian volume fraction.

$$\tilde{\boldsymbol{F}}^{ext} = (1 - \mathcal{F}^L)\boldsymbol{F}^{ext^E} + \mathcal{F}^L(\Delta \boldsymbol{F}_{acc} + \Delta \boldsymbol{F}_{\sigma}) \tag{56}$$

3.10. Penalty Constraints – Eulerian Momentum Equations

The penalty terms for the Eulerian momentum equations can be broken down into the contributions in the overlap region $\bar{\Omega}$ and the contributions associated with the boundary of the Lagrangian domain in the overlap region. At the element level the respective penalty terms are

$$P_I^{E_\Omega} = \int_{\Omega^e} \chi^E N_I (v_i^E - v_i^L) d\Omega \tag{57}$$

for the elements in interior of the Eulerian overlap region $\bar{\Omega}$, and

$$P_I^{E_\Gamma} = \int_{\Omega^e} \chi^E N_I (v_i^E - v_i^L) d\Omega \tag{58}$$

for the Eulerian elements cut by the Lagrangian boundary. Here, I indicates the local node number on the element. The boundary penalty term in Eq. (58) effectively distributes the velocity constraint, in a weak sense, to the nodes of the Eulerian elements cut by the Lagrangian boundary.

First, we consider the interior penalty, P^{E_Ω}, in the Eulerian momentum equations. The assembled form of the Eulerian momentum equations used during the Lagrangian step in SABLE are

$$M_L^E \mathbf{a}^E + \mathbf{B}^T \boldsymbol{\sigma}^E - \mathbf{F}^{ext} - M_L^E (\mathbf{a}^E - \mathbf{a}^L)_{\bar{\Omega}} - \mathbf{B}^T (\boldsymbol{\sigma}^E - \boldsymbol{\sigma}^L)_{\bar{\Omega}} + \chi^E M_L^U (\mathbf{v}^E - \mathbf{v}^L)_{\bar{\Omega}} = 0 \tag{59}$$

where $\mathbf{a}^E = D\mathbf{v}^E/Dt$, $\mathbf{B}^T$ is the usual B-matrix, and the external forces are

$$\mathbf{F}_I^{ext^E} = \int_{\Gamma^E} \hat{N}_I \boldsymbol{\sigma}^E \cdot \mathbf{n} d\Gamma + \int_{\Omega^E} N_I \bar{\rho} \mathbf{g} d\Omega \tag{60}$$

The row-sum lumped mass matrix is

$$M_{L_I}^E = \frac{1}{Nnpe} \bar{\rho} V^E \tag{61}$$

The "unit" row-sum lumped mass matrix is

$$M_{L_I}^U = \frac{1}{Nnpe} V^E \tag{62}$$

The penalty multiplier is defined as

$$\chi^E = \frac{\theta \bar{\rho}}{\Delta t_{mid}} \tag{63}$$

where $\theta \geq 0$. The penalty term may be defined in an alternative, and more convenient form as

$$\chi^E M_L^U (\mathbf{v}^E - \mathbf{v}^L)_{\bar{\Omega}} = \theta M_L^E \left(\frac{\mathbf{v}^E - \mathbf{v}^L}{\Delta t_{mid}} \right)_{\bar{\Omega}} \tag{64}$$

where the time-step Δt_{mid} is based on the SABLE time integrator.

The effects of the choices for the time-centering of the Lagrangian and Eulerian velocities in the coupling algorithm and penalty constraints are considered next. First, considering that the Eulerian velocity presented to the Lagrangian solver in OPENIFEM is $\mathbf{v}^{E^{n-1/2}}$, and the acceleration computed for the coupling term is approximated as

$$\mathbf{a}^E \approx \frac{\mathbf{v}^{L^{n+1}} - \mathbf{v}^{E^{n-1/2}}}{\Delta t_{mid}} + \mathbf{v}^{E^{n-1/2}} \cdot \nabla \mathbf{v}^{E^{n-1/2}} \tag{65}$$

The choice to use $V^{L^{n+1}}$ is based, in part, on the use of the Newmark time-integrator in OPENIFEM where the Lagrangian velocity at t^{n+1} is known before the Eulerian velocity has been updated. In addition, this choice is made in order to impose the velocity continuity for the updated Eulerian velocity.

The momentum equation may be rearranged in a more traditional form as

$$\begin{aligned} M_L^{E^n} \mathbf{a}^{E^n} &= \mathbf{F}^{ext^n} - \mathbf{B}^T \boldsymbol{\sigma}^{E^n} \\ &+ M_L^{E^n} \left[(1+\theta) \left(\frac{\mathbf{v}^{L^{n+1}} - \mathbf{v}^{E^{n-1/2}}}{\Delta t_{mid}} \right) + \mathbf{v}^{E^{n-1/2}} \cdot \nabla \mathbf{v}^{E^{n-1/2}} - \mathbf{a}^{L^{n+1}} \right]_{\bar{\Omega}} \\ &+ \mathbf{B}^T (\boldsymbol{\sigma}^{E^n} - \boldsymbol{\sigma}^{L^{n+1}})_{\bar{\Omega}} \end{aligned} \tag{66}$$

where the velocities used in the penalty term are $\mathbf{v}^{L^{n+1}}$ and $\mathbf{v}^{E^{n-1/2}}$.

In this form, using $\theta = 1$ effectively doubles the magnitude of the velocity difference contribution to the residual acceleration term.

An alternative formulation based on the explicit central-differences integrator in SABLE makes use of the definition for the velocity update

$$\mathbf{a}^{E^n} = \frac{\mathbf{v}^{E^{n+1/2}} - \mathbf{v}^{E^{n-1/2}}}{\Delta t_{mid}} \tag{67}$$

Using this definition for the Eulerian acceleration, assuming $\theta = 1$, and treating the Eulerian velocity as unknown, the penalty term may be re-written as

$$\begin{aligned} M_L^E \left(\frac{\mathbf{v}^{E^{n+1/2}} - \mathbf{v}^{L^{n+1}}}{\Delta t_{mid}} \right)_{\bar{\Omega}} &= M_L^E \left(\frac{\mathbf{v}^{E^{n+1/2}} - \mathbf{v}^{L^{n+1}} + \mathbf{v}^{E^{n-1/2}} - \mathbf{v}^{E^{n-1/2}}}{\Delta t_{mid}} \right)_{\bar{\Omega}} \\ &= M_L^E \left(\mathbf{a}^{E^n} - \frac{\mathbf{v}^{L^{n+1}} - \mathbf{v}^{E^{n-1/2}}}{\Delta t_{mid}} \right)_{\bar{\Omega}} \end{aligned} \tag{68}$$

where $\mathbf{a}^{E^n}$ is considered an unknown.

Using this choice for the velocity time-centering in the penalty term in the momentum equation yields

$$\begin{aligned} M_L^{E^n} \mathbf{a}^{E^n} &= \mathbf{F}^{ext^n} - \mathbf{B}^T \boldsymbol{\sigma}^{E^n} \\ &+ M_L^{E^n} (\mathbf{a}^{E^n} - \mathbf{a}^{L^{n+1}})_{\bar{\Omega}} + \mathbf{B}^T (\boldsymbol{\sigma}^{E^n} - \boldsymbol{\sigma}^{L^{n+1}})_{\bar{\Omega}} \\ &- M_L^{E^n} (\mathbf{a}^{E^n})_{\bar{\Omega}} + M_L^{E^n} \left(\frac{\mathbf{v}^{L^{n+1}} - \mathbf{v}^{E^{n-1/2}}}{\Delta t_{mid}} \right)_{\bar{\Omega}} \end{aligned} \tag{69}$$

In this form, the Eulerian acceleration terms $M_L^E (\mathbf{a}^{E^n})_{\bar{\Omega}}$ cancel, and the final form of the momentum equation may be written as

$$\begin{aligned} M_L^{E^n} \mathbf{a}^{E^n} &= \mathbf{F}^{ext^n} - \mathbf{B}^T \boldsymbol{\sigma}^{E^n} \\ &+ M_L^{E^n} \left(\frac{\mathbf{v}^{L^{n+1}} - \mathbf{v}^{E^{n-1/2}}}{\Delta t_{mid}} - \mathbf{a}^{L^{n+1}} \right)_{\bar{\Omega}} + \mathbf{B}^T (\boldsymbol{\sigma}^{E^n} - \boldsymbol{\sigma}^{L^{n+1}})_{\bar{\Omega}} \end{aligned} \tag{70}$$

$$\tag{71}$$

This form of the momentum equations build-in the effect of the penalty term, and simplifies the residual acceleration terms.

Next, the boundary penalty constraint is formulated for the Eulerian domain. The formulation relies on interpolating the Lagrangian velocity either at integration points on the Lagrangian boundary that intersects the Eulerian elements as shown in Figure 3-12, or by interpolating the Lagrangian velocity at nodes of the Eulerian mesh.

In the first approach, the Lagrangian velocity is interpolated at the surface integration points as shown in Figure 3-12

$$\mathbf{v}^L = \sum_{j=1}^{Nnpe} \hat{N}_J \mathbf{v}_J^L \tag{72}$$

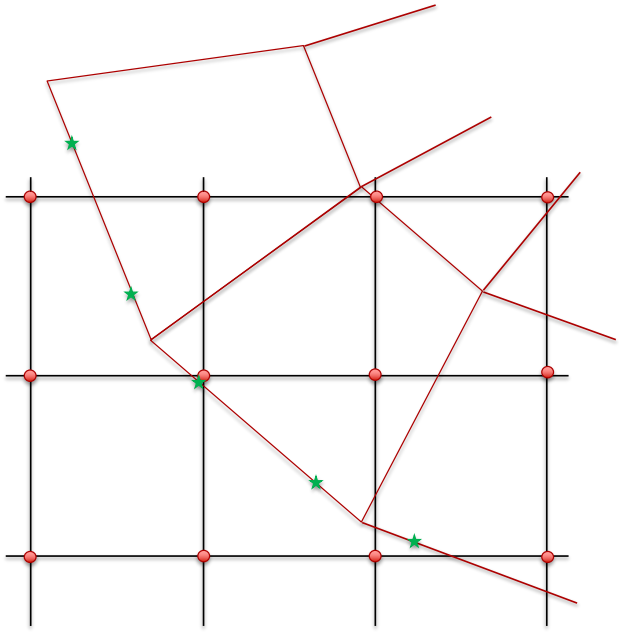

Figure 3-12 Integration points on the Lagrangian boundary relative to the Eulerian elements. Surface quadrature points are indicated by ⋆, and Eulerian nodes by ●.

The integration point is used to solve the inverse problem for the natural coordinates $\boldsymbol{\xi}$ ($\boldsymbol{\xi} = (\xi, \eta)$ in two spatial dimensions) in the intersected Eulerian element. Armed with this data, the penalty constraint becomes

$$\mathbf{P}_I^E = \int_{\Omega_E} \chi^E N_I \Big(\sum_{j=1}^{Nnpe} N_{J_\xi} \mathbf{v}_J^E - \mathbf{v}^L \Big) d\Omega \tag{73}$$

Here, the shape functions N_J are evaluated using the natural coordinates $\boldsymbol{\xi}$ in the Eulerian element associated with the integration point on the Lagrangian boundary. It is important to note that high-order quadrature rules will likely be necessary for this approach.

Turning to the time-centering for the Eulerian velocity, first consider treating the velocity as unknown at $t^{n+1/2}$. At the element level, this can be written in matrix form as

$$\begin{bmatrix} [L]^e & 0 & 0 \\ 0 & [L]^e & 0 \\ 0 & 0 & [L]^e \end{bmatrix} \begin{Bmatrix} v_x \\ v_y \\ v_z \end{Bmatrix} = \begin{Bmatrix} b_x \\ b_y \\ b_z \end{Bmatrix} \tag{74}$$

where the matrix and right-hand-side contributions for each coordinate direction i are

$$[L]^e = \int_{\Omega^E} \chi^E \begin{bmatrix} N_1 N_{1_\xi} & N_1 N_{2_\xi} & N_1 N_{3_\xi} & N_1 N_{4_\xi} \\ N_2 N_{1_\xi} & N_2 N_{2_\xi} & N_2 N_{3_\xi} & N_2 N_{4_\xi} \\ N_3 N_{1_\xi} & N_3 N_{2_\xi} & N_3 N_{3_\xi} & N_3 N_{4_\xi} \\ N_4 N_{1_\xi} & N_4 N_{2_\xi} & N_4 N_{3_\xi} & N_4 N_{4_\xi} \end{bmatrix} d\Omega \tag{75}$$

$$\left\{ \begin{array}{c} \mathbf{b}_{i_1} \\ \mathbf{b}_{i2} \\ \mathbf{b}_{i_3} \\ \mathbf{b}_{i_4} \end{array} \right\} = \int_{\Omega^E} \chi^E \left\{ \begin{array}{c} N_1 \mathbf{v}_{i_1}^L \\ N_2 \mathbf{v}_{i_2}^L \\ N_3 \mathbf{v}_{i_3}^L \\ N_4 \mathbf{v}_{i_4}^L \end{array} \right\} d\Omega \tag{76}$$

This results in a non-symmetric system that needs to be assembled for all Eulerian elements cut by the Lagrangian elements, and then solved globally. In passing, we note that it may be necessary to incorporate the effect of the Lagrangian volume-fraction represented on the Eulerian mesh in the penalty formulation. Unfortunately, there is no clear path for integrating this form of the constraint into the explicit time-integrator for the Lagrangian step in SABLE.

Turning to the second approach where the Lagrangian velocities are interpolated at the Eulerian nodes, a simpler formulation is obtained. The penalty constraint at the element level is

$$\mathbf{P}_I^E = \int_{\Omega_E} \chi^E \mathcal{F}^L N_I \sum_{J=1}^{Nnpe} N_J (\mathbf{v}_J^E - \mathbf{v}_J^L) \, d\Omega \tag{77}$$

where the Lagrangian volume-fraction $\mathcal{F}^L$ has been incorporated to reflect the effect of partially covered Eulerian cells. We note that this version of the penalty terms may be easily implemented in SABLE using a row-sum lumped mass matrix.

3.11. Penalty Constraints – Lagrangian Momentum Equations

This section addresses the treatment of the penalty constraints applied to the Lagrangian problem. Turning to the Lagrangian momentum equations, the assembled equations may be written as

$$M_L^L \mathbf{a}^L + \mathbf{B}^T \boldsymbol{\sigma}^L - \mathbf{F}^{L^{ext}} + \chi^L M_L^U (\mathbf{v}^L - \mathbf{v}^E) = 0 \tag{78}$$

where, $\mathbf{B}^T$ is the usual B-matrix, M_L^U is a unit matrix, and the external forces are

$$\mathbf{F}_I^{ext^L} = \int_{\Gamma^L} \hat{N}_I \boldsymbol{\sigma}^E \cdot \mathbf{n} d\Gamma + \int_{\Omega^L} N_I \bar{\rho} \mathbf{g} d\Omega \tag{79}$$

The penalty constraints may be applied in the volume of the Lagrangian domain, or restricted to the boundary. The choice to treat the velocity penalty constraints on the Lagrangian boundary is somewhat arbitrary, but can be made to explicitly enforce no-slip/no-penetration conditions at the interface between the Eulerian and Lagrangian domains.

The penalty multiplier is defined for the volume and the boundary with consistent dimensions as

$$\chi^L = \left\{ \begin{array}{l} \frac{h \, \rho^L}{\Delta t_{mid}} \quad on \; \Gamma^L \\ \\ \frac{\rho^L}{\Delta t_{mid}} \quad in \; \Omega^L \end{array} \right. \tag{80}$$

For simplicity, the length scale h is taken as the local Eulerian element size for the boundary penalty multiplier.

The penalty term may again be defined in an alternative, and more convenient form as

$$\chi^L M_L^U (\mathbf{v}^E - \mathbf{v}^L) = \tilde{M}_L^L \left(\frac{\mathbf{v}^E - \mathbf{v}^L}{\Delta t_{mid}} \right) \tag{81}$$

where, at the element level,

$$\tilde{M}_{L_I}^L = \begin{cases} h \int_{\Gamma^e} \rho^L \hat{N}_I d\Gamma \ \ on\ \Gamma^L \\ \\ \frac{1}{Nnpe} \rho^L V^E \ \ in\ \Omega^L \end{cases} \tag{82}$$

In the ensuing discussion, the penalty term will be written as $\tilde{M}_L^L(\mathbf{v}^E - \mathbf{v}^L)/\Delta t_{mid}$ with the understanding that it could be applied either in the Lagrangian volume or on the Lagrangian boundary.

Explicit Central Differences

Assuming an explicit central-difference integrator will be used, the penalty term in the momentum equations use Eulerian and Lagrangian velocities centered at $t^{n-1/2}$.

$$M_L^L \mathbf{a}^{L^n} = \mathbf{F}^{L^{ext^n}} - \mathbf{B}^T \boldsymbol{\sigma}^{L^n} + \tilde{M}_L^L \left(\frac{\mathbf{v}^{E^{n-1/2}} - \mathbf{v}^{L^{n-1/2}}}{\Delta t_{mid}} \right) \tag{83}$$

Here, it is assumed that added mass terms have been included in M_L^L but not in $\tilde{M}_L^L$, and that the traction forces from the Eulerian domain are included in $F^{L^{ext}}$. Once the Lagrangian acceleration is computed, the time-integration proceeds without any additional changes.

Newmark A-Form Integrator

OPENIFEM uses the so-called "a-form" of the Newmark time-integrator with parameters chosen for second-order accuracy in time and unconditional stability. There are several choices for the time-centering of the Lagrangian velocities in the Newmark integrator.

The a-form of the Newmark begins with predictors for the velocity and displacement using known data at t^n.

$$\tilde{\mathbf{d}}^{L^{n+1}} = \mathbf{d}^{L^n} + \Delta t \mathbf{v}^{L^n} + \frac{\Delta t^2}{2}(1 - 2\beta)\mathbf{a}^{L^n} \tag{84}$$

$$\tilde{\mathbf{v}}^{L^{n+1}} = \mathbf{v}^{L^n} + \Delta t(1 - \gamma)\mathbf{a}^{L^n} \tag{85}$$

Once the acceleration at t^{n+1} is known, the final displacements and velocities are computed using corrects as

$$\mathbf{d}^{Ln+1} = \tilde{\mathbf{d}}^{L^{n+1}} + \beta \Delta t^2 \mathbf{a}^{L^{n+1}} \tag{86}$$

$$\mathbf{v}^{L^{n+1}} = \tilde{\mathbf{v}}^{L^{n+1}} + \gamma \Delta t \mathbf{a}^{L^{n+1}} \tag{87}$$

Treating the velocity explicitly at t^n in the penalty constraint yields the following equation for the Lagrangian acceleration

$$[M_L^L + \beta \Delta t^2]\mathbf{a}^{L^{n+1}} = \mathbf{F}^{L^{ext^n}} - K\tilde{\mathbf{d}}^{L^{n+1}} + \tilde{M}_L^L \left(\frac{\mathbf{v}^{E^{n-1/2}} - \mathbf{v}^{L^n}}{\Delta t_{mid}} \right) \tag{88}$$

where K is the elastic stiffness matrix. Alternatively, the predicted velocity could be used, i.e.,

$$[M_L^L + \beta \Delta t^2]\mathbf{a}^{L^{n+1}} = \mathbf{F}^{L^{ext^n}} - K\tilde{\mathbf{d}}^{L^{n+1}} + \tilde{M}_L^L \left(\frac{\mathbf{v}^{E^{n-1/2}} - \tilde{\mathbf{v}}^{L^{n+1}}}{\Delta t_{mid}} \right) \tag{89}$$

Finally, in order to treat the the velocity in the penalty constraint implicitly, the velocity corrector Eq. (87) is substituted for the Lagrangian velocity in the penalty constraint. Rearranging terms yields the following momentum equation

$$\left[M_L^L + \frac{\gamma \Delta t}{\Delta t_{mid}} \tilde{M}_L + \beta \Delta t^2 \right] \mathbf{a}^{L^{n+1}} = \mathbf{F}^{L^{ext^n}} - K\tilde{\mathbf{d}}^{L^{n+1}} + \tilde{M}_L^L \left(\frac{\mathbf{v}^{E^{n-1/2}} - \tilde{\mathbf{v}}^{L^{n+1}}}{\Delta t_{mid}} \right) \tag{90}$$

Alternatively, the penalty terms can be written in terms of a damping matrix

$$\left[M_L^L + \gamma \Delta t C + \beta \Delta t^2 \right] \mathbf{a}^{L^{n+1}} = \mathbf{F}^{L^{ext^n}} - K\tilde{\mathbf{d}}^{L^{n+1}} + C(\mathbf{v}^{E^{n-1/2}} - \tilde{\mathbf{v}}^{L^{n+1}}) \tag{91}$$

where

$$C = \frac{1}{\Delta t_{mid}} \tilde{M}_L^L \tag{92}$$

Similar to the explicit time-integration method, it is assumed that the added-mass terms have been included in the lumped mass, and traction forces from the Eulerian domain are included in $\mathbf{F}^{L^{ext}}$.

3.12. Velocity Reset with Void

The use of void to represent the Lagrangian region in the Eulerian mesh can result in large artificial differences between the Lagrangian and Eulerian velocities in the overlap region. The consequence of these differences can be relatively large coupling forces due to the approximation for the Eulerian acceleration. To avoid this, the Lagrangian volume fraction, $\mathcal{F}^L$ is first lifted to the nodes with a simple L^2 projection. The nodal Lagrangian volume fraction is used to identify nodes in regions of overlap that are completely surrounded by void and then reset the velocity, i.e.,

$$\boldsymbol{v}^E = \begin{cases} \boldsymbol{v}^L & if \quad \mathcal{F}^L = 1 \\ \boldsymbol{v}^E & otherwise \end{cases} \tag{93}$$

In regions of overlap, where there is pure void, this forces the Eulerian velocity to match the Lagrangian velocity. This was found to be necessary due to the effects of remap on the Eulerian velocity in pure void regions, which caused spurious coupling forces to be generated in the void region. See Appendix A for the SABLE velocity reset keywords.

In order to further justify the choice to force the velocities to match in regions of overlap where there is pure void in the Eulerian mesh, consider the following situation for Eq. (55). As shown in §3.6, the coupling node mass has the effect of smoothly inserting the Lagrangian mass into the Eulerian mesh. In void, there is no average Eulerian stress, so that the calculation of the Eulerian acceleration during the Lagrangian step simplifies to

$$\tilde{M}_L \boldsymbol{a}^E = \tilde{M}_L(\tilde{\boldsymbol{a}}^E - \boldsymbol{a}^L) - \boldsymbol{F}^{int^L} \tag{94}$$

Expanding the Eulerian acceleration terms, and ignoring the advective term in Eq. (45),

$$\tilde{M}_L(\boldsymbol{v}^{E^{n+1/2}} - \boldsymbol{v}^{E^{n-1/2}}) = \tilde{M}_L(\boldsymbol{v}^L - \boldsymbol{v}^{E^{n-1/2}}) - \Delta t_{mid}\ (\tilde{M}_L \boldsymbol{a}^L + \boldsymbol{F}^{int^L}) \tag{95}$$

Note that the advective term has been demonstrated to be a second-order effect in prototypical calculations where void is used for the Lagrangian overlap region. In the absence of external forces, e.g., body forces for the Lagrangian problem, $\tilde{M}_L \boldsymbol{a}^L + \boldsymbol{F}^{int^L} = 0$ and the Eulerian velocities at time $t^{n-1/2}$ cancel. This yields

$$\boldsymbol{v}^{E^{n+1/2}} = \boldsymbol{v}^L \tag{96}$$

Finally, the time level for $\boldsymbol{v}^L$ is t^{n+1} for OpenIFEM due to the unconditionally stable Newmark time integrator. For an explicit Lagrangian solver, the time level is $t^{n+1/2}$.

3.13. Subcycling for Time-Integration

Subcycling time-steps may be useful when the time step for one of the coupled codes is significantly smaller than the other code. No attempt was made to subcycle SABLE with respect to OpenIFEM. However, this may be important when SABLE is coupled to an explicit Lagrangian code.

3.14. Eulerian Remap Issues

Up to this point, the emphasis has been on the Lagrangian step of the Eulerian solver. As suggested in §3.12, there are some pathologies associated with the remap procedure in SABLE. Although the Lagrangian step in SABLE is informed by the Lagrangian volume fraction for overlap, the coupling node mass and associated forces, the remap procedure does not benefit from this information.

The remap algorithm and integral interface reconstruction only sees the materials present in elements, and the Lagrangian material is not explicitly present. The only materials that correspond to overlapping Lagrangian material is void or a matched background material. This

results in a mismatch between where the Lagrangian material is located and where an Eulerian interface between void (or the background material) is located.

Several attempts to constrain the material remap in SABLE using the Lagrangian volume fraction $\mathcal{F}^L$ have been made. The first attempt adjusted the volume fluxes based on the Lagrangian volume fraction. A more refined version of this adjustment was made to the material volume flux after interface reconstruction. Unfortunately, the number of unknowns exceeds the number of equations that can be generated using a partition of unity, i.e.,

$$\mathcal{F}^L + \sum_{\alpha=1}^{Nmat} \mathcal{F}^\alpha = 1 \tag{97}$$

The consequence of the error in locating the material interface, and constraining the material remap is that leakage can occur on coarse meshes. Refinement of the Eulerian mesh relative to the Lagrangian mesh improves this situation, but can not eliminate the problem. Additional work will be required to correct this issue in the remap procedure in SABLE.

4. RESULTS

This section presents results for a series of test problems used to evaluate the code-coupling algorithms described in §2 and §3. There are essentially three basic models that have been used during the assessment of the coupling algorithms. All of the models use the residual force coupling outlined in §3. The models used for testing are

1. Force coupling with an Eulerian background material where the Lagrangian and Eulerian domains overlap. The background material may be matched to the Lagrangian material, e.g., matched elastic modulus and density. In this case, the background material stress is typically removed from the average Eulerian stress used to compute the Lagrangian traction forces.

2. Alternatively, the Eulerian background material may not be matched with the Lagrangian material. This is the case when there is a gas surrounding the Lagrangian domain, and the same gas is used as the Eulerian background material the overlap region. In this case, the average stress does not require adjustment for the background material.

3. In some cases, it may be desirable to use void in the region of Eulerian – Lagrangian overlap. In this case, a velocity reset is used to keep the Eulerian void velocities synchronized with the Lagrangian velocities at nodes that are “pure” void.

As noted in §3, a direct velocity coupling that imposed the Lagrangian velocities directly on the Eulerian mesh was tested. However, this variant of the coupling algorithm did not consistently produce physical results and was dropped from further investigation.

The stable time-step for coupled calculations is discussed in §3.3. For all results presented in this section, the additional time-step scaling is applied when void is used where the Lagrangian material resides in the Eulerian mesh.

4.1. Block-On-Air

The block-on-air test model is used for testing a variety of algorithmic options. The block-on-air Eulerian domain is a 10×10 *cm* region discretized with $(\Delta x, \Delta y) = (1.0, 1.0)$ *cm* elements as shown in Figure 4-1. Air is in the region below the Lagrangian block, and void is above the block. Initially, the air pressure is $P = 2.0 \times 10^6 dynes/cm^2$. Zero normal displacement conditions are prescribed on the left, right and bottom boundaries of the Eulerian domain.

The Lagrangian domain is a 4×10 *cm* domain also discretized with $(\Delta x, \Delta y) = (1.0, 1.0)$ *cm* elements. The block is initially at rest in a stress-free state. The left/right sides of the copper block are constrained in the x-direction.

The material model for the Lagrangian block is linear-elastic copper with $\rho = 8.93\ g/cm^3$, Young's modulus $E = 1.076 \times 10^{12}\ dynes/cm^2$, and Poisson's ratio $\nu = 0.355$. The KEOS Sesame model is used for the air.

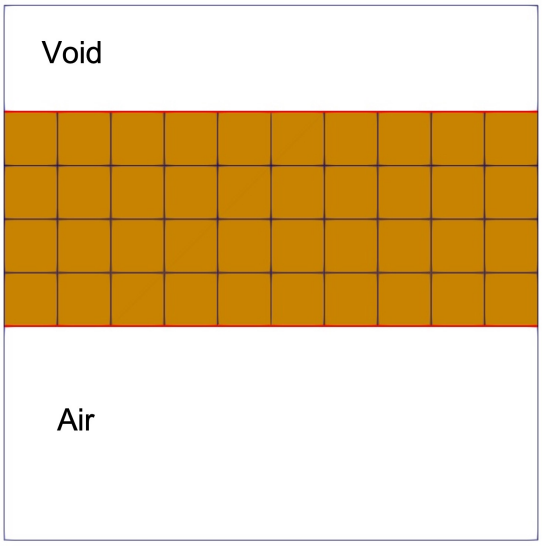

Figure 4-1 Block-on-air geometry.

4.1.1. Baseline Calculations

Two different baseline calculations are used to evaluate the behavior of the coupled Lagrangian-Eulerian algorithm. The first is simply a rigid-body computation using a constant-pressure boundary condition, and the second is a pure Eulerian calculation using the problem specification above. In the Eulerian calculation, copper material is inserted in the location of the Lagrangian copper block. For the initial comparisons, all simulations were run for a time period of $50\mu s$. Figure 4-2 shows a snapshot of the block velocity for the Eulerian case with isolines of the copper volume-fraction that approximate the material interface location.

For the coupled block-on-air tests where void is used in the Eulerian model for the region occupied by the Lagrangian block, stability requires that the time-step scale factor be adjusted based on the relative wave-speeds of the Eulerian and Lagrangian materials. Here, the scale factor is $\beta = 0.1069$ resulting in an overall time-step scale factor $\alpha = 0.0909$. This scale factor is used for all block-on-air calculations. The stability requirements for the coupled calculations are discussed in §3.3.

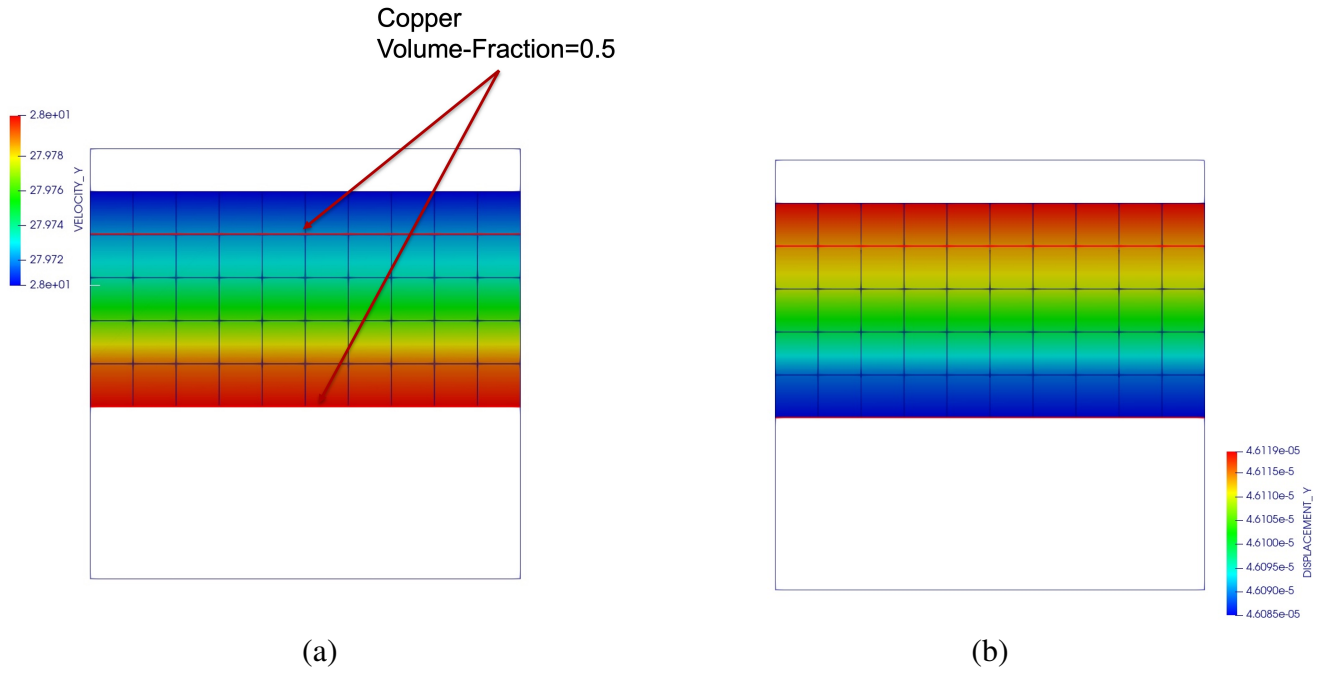

Figure 4-2 Snapshot of (a) the Eulerian velocity and (b) the Eulerian displacement at $50\mu s$.

Figure 4-3 shows the time history of y-momentum for the copper block. For the $50\mu s$ time-scale, the Eulerian and rigid-body results are essentially identical. For longer time-scales, the constant pressure driving force for the rigid-body test, and the driving pressure for the coupled case diverge. Figure 4-4 shows the kinetic energy time history for the Eulerian and rigid-body cases. Again, the Eulerian and rigid-body results are essentially identical for the time-scale considered.

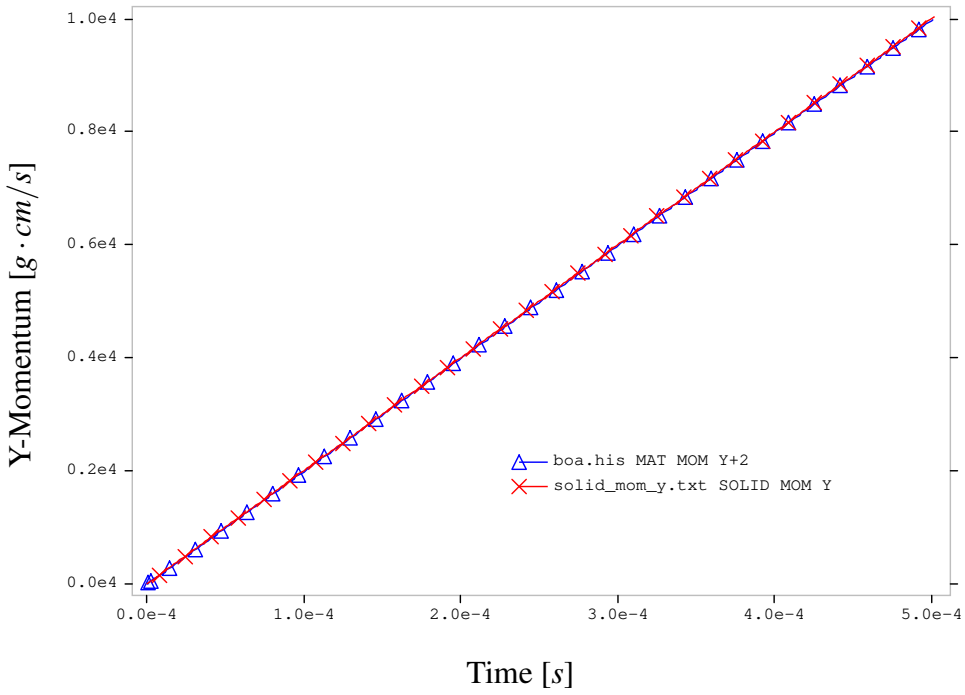

Figure 4-3 Y-momentum time histories for rigid-body (×) and Eulerian (△) calculations.

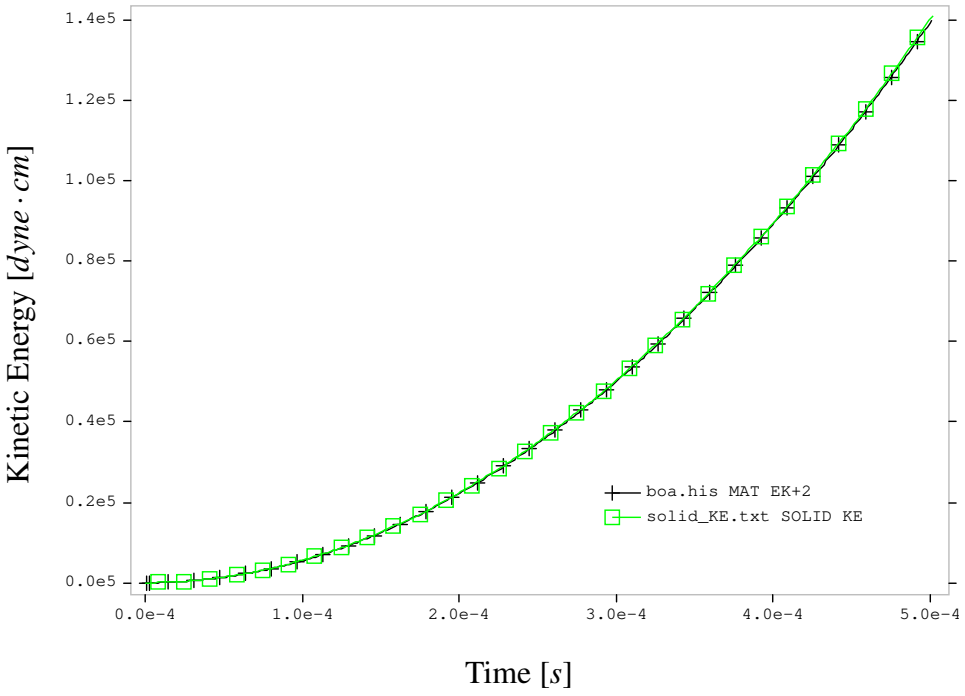

Figure 4-4 Kinetic energy time histories for rigid-body (□) and Eulerian (+) calculations.

4.1.2. *Coupled, Matched Background Material*

This case uses a background material inserted in the Eulerian mesh that matches the Lagrangian block. The SABLE material model uses a linear elastic constitutive model with a Mie Grüneisen equation of state for the copper block. Due to slight differences between the air-copper interface and the boundary of the Lagrangian block, a normal offset of $\delta = 0.01\ \Delta y$ is used for the application of the traction conditions on the Lagrangian block. In addition, the background material stress is removed from the average Eulerian stress used to compute the Lagrangian traction on the block (see the *background coupling material* keyword in A).

Note: The added-mass terms were not included in this comparison. Including them retards the motion of the block in a way that requires further investigation.

Figure 4-5 shows snapshots of the Lagrangian velocity and displacement at $50\mu s$.

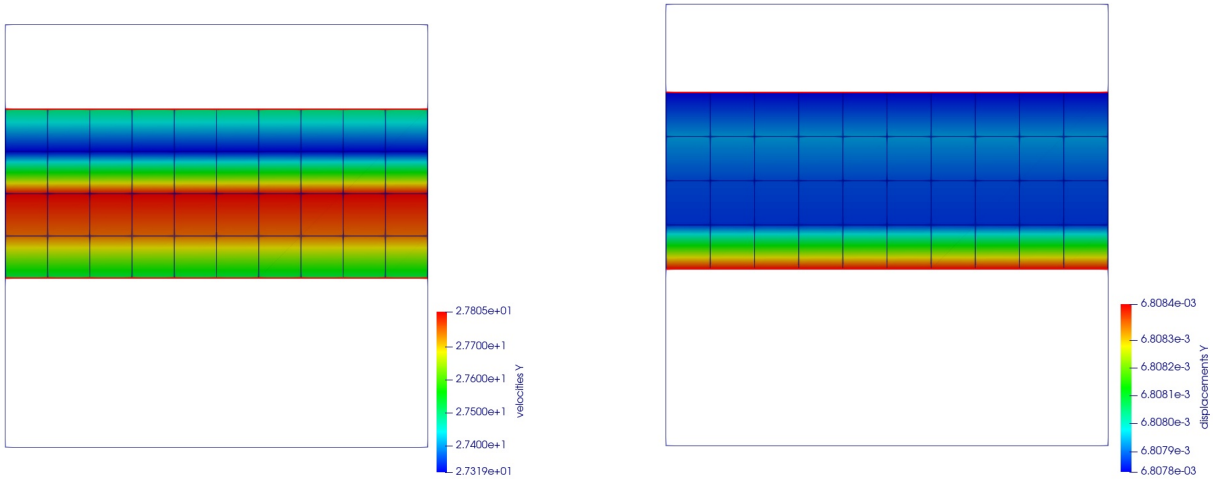

Figure 4-5 Snapshot of (a) the Lagrangian velocity and (b) the Lagrangian displacement at $50\mu s$.

Figure 4-6 shows the time history of y-momentum for the copper block. For the $50\mu s$ time-scale, the Eulerian, rigid-body, and coupled results are essentially identical. Figure 4-7 shows the kinetic energy time history for the Eulerian, rigid-body, and coupled cases. Again, the Eulerian, rigid-body, and coupled results are essentially identical over the simulated time scale.

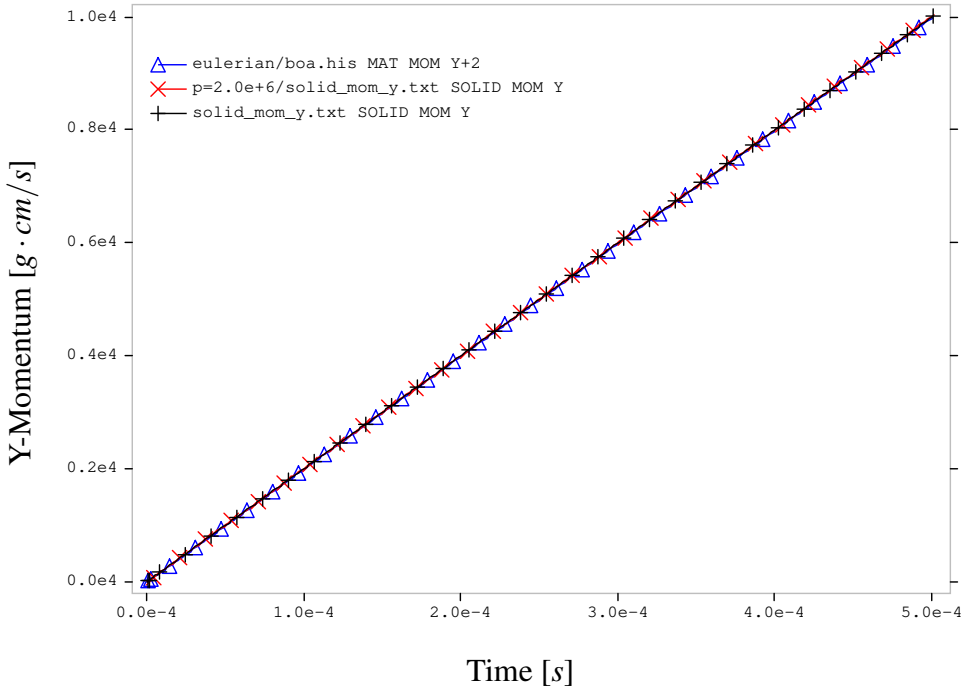

Figure 4-6 Y-momentum time histories for rigid-body (×), Eulerian (△), and coupled (+) calculations.

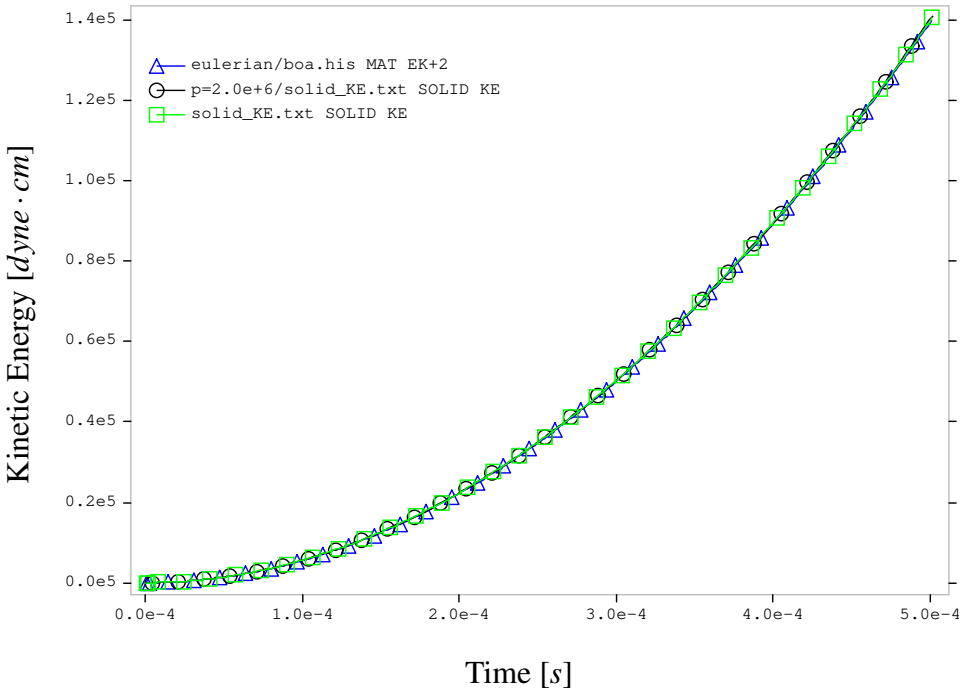

Figure 4-7 Kinetic energy time histories for rigid-body (◯), Eulerian (△), and coupled (□) calculations.

4.1.3. Coupled, Void Background Material

In this test, force-coupling is used with void in the region occupied by the Lagrangian block. Note that there is no initial overlap between the gas volume and the Lagrangian block.

Figure 4-8 shows snapshots of the Lagrangian velocity and displacement at $50\mu s$. Figure 4-9 shows the time history of y-momentum for the copper block. For the $50\mu s$ time-scale, the Eulerian, rigid-body, and coupled results are essentially identical. Figure 4-10 shows the kinetic energy time history for the Eulerian, rigid-body, and coupled cases. Again, the Eulerian, rigid-body, and coupled results are essentially identical.

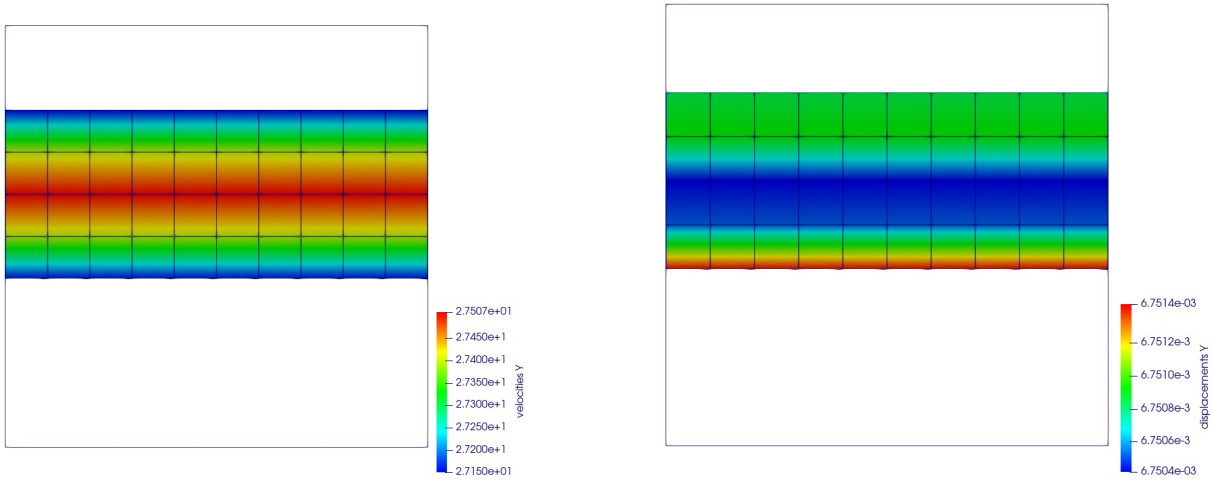

(a) (b)

Figure 4-8 Snapshot of (a) the Lagrangian velocity and (b) the Lagrangian displacement at $50\mu s$.

4.1.4. Leakage Issues

In the current OPENIFEM – SABLE coupling, there is an inherent mismatch between the Lagrangian boundary of the block and the Eulerian interface between the gas and void. This issue was outlined in §3.14. To illustrate the issue, the block-on-air problem was run for a total simulated time of 7.0×10^{-3} s. Snapshots of the gas/void material location and corresponding block location and velocities are shown in Figure 4-11. Although the coupling algorithm is functioning correctly, the interface reconstruction and material remap is not constrained by the location of the Lagrangian block and the associated Lagrangian volume fraction. In addition, there is no explicit enforcement of the kinematic conditions $\mathbf{v}^E = \mathbf{v}^L$ at the gas-solid interface.

The apparent leakage issue may be reduced by refining the Eulerian mesh relative to the Lagrangian mesh. However, mesh refinement studies showed that the leakage problem persists even when the Eulerian element size is reduced by a factor of 8 in each spatial direction relative to the Lagrangian element size. The leakage behavior is not observed in all test problems considered, but is particularly apparent in the block-on-air test.

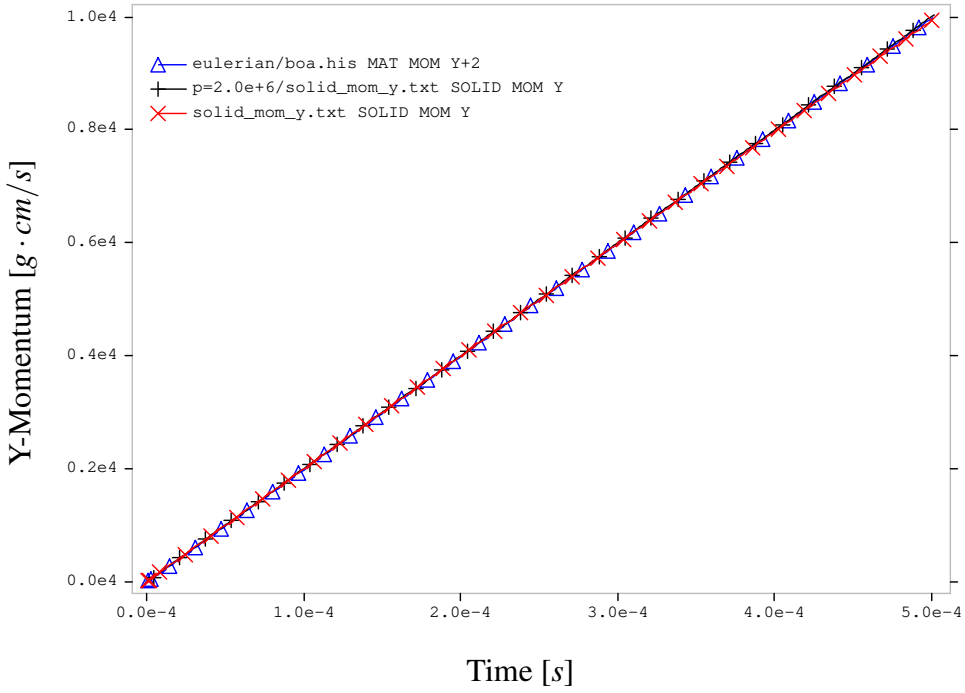

Figure 4-9 Y-momentum time histories for rigid-body (×), Eulerian (△), and coupled (+) calculations.

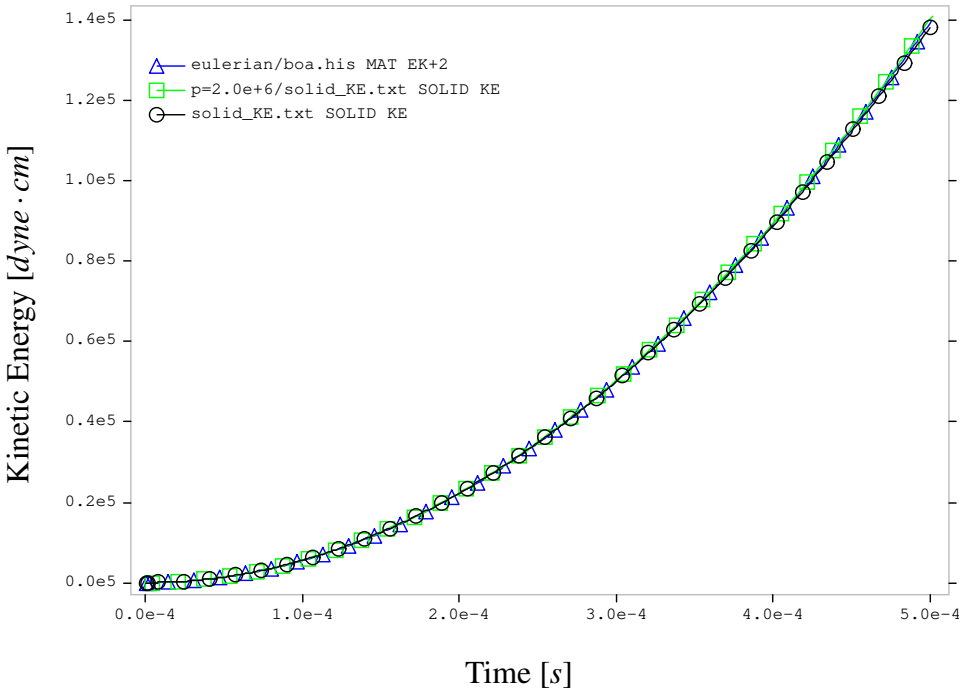

Figure 4-10 Kinetic energy time histories for rigid-body (◯), Eulerian (△), and coupled (□) calculations.

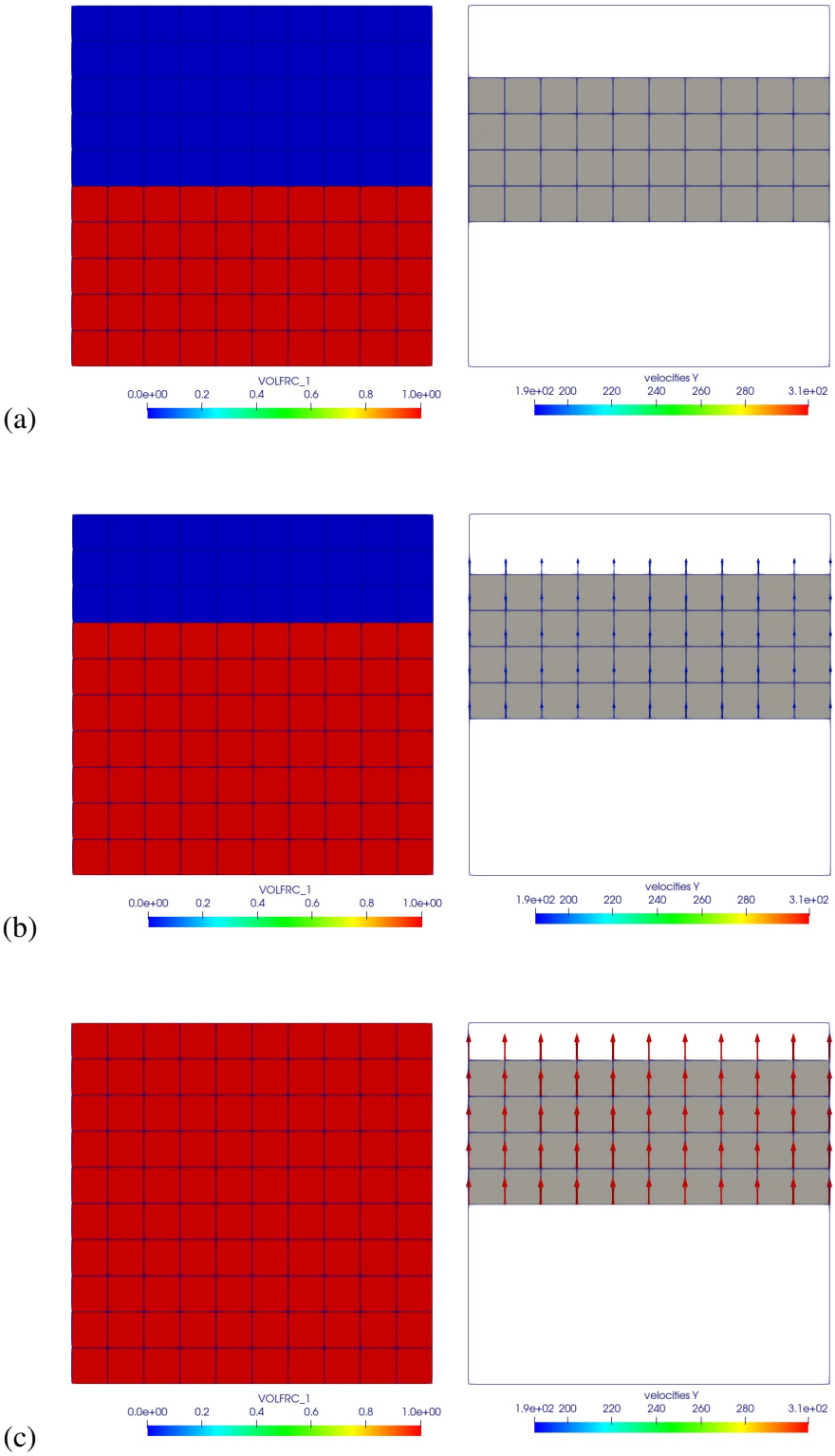

Figure 4-11 Snapshots of the Eulerian gas (red) and void volume fraction (blue) on the left and the Lagrangian block and velocities on the right at (a) $t = 0\ s$, (b) $t = 3.75 \times 10^{-3}\ s$, and (c) $t = 7.0 \times 10^{-3}\ s$.

4.1.5. Static Case, Matched Background Material

A simple, but important limiting case is where the Lagrangian block is fully constrained remaining static despite the pressurized air. In this test, the gas volume does not overlap with the region occupied by the Lagrangian body, and a matched background material in the Eulerian mesh is used. Here, all quantities should remain fixed, and there should be no leakage of gas under the Lagrangian block into the void region.

Figure 4-12 shows snapshots of the Eulerian gas velocity and volume fraction at $t = 50\ \mu s$. Here, the gas has been moved into the region occupied by the Lagrangian solid. This is due, in part, to the remap issues outlined in §3.14. Note that mesh refinement does reduce the amount of gas that moves under the Lagrangian block, but do not stop this from occurring. The coupling forces attempt to slow the progress of the gas, but do not directly enforce any form of kinematic, i.e., no-slip/no-penetration conditions at the wetted interface.

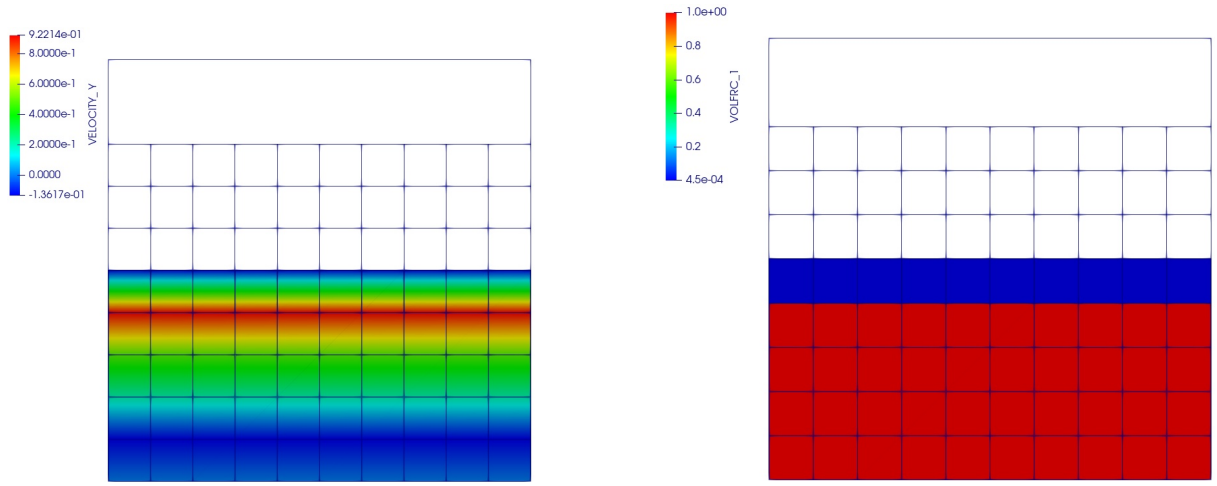

(a) (b)

Figure 4-12 Snapshot of (a) the Eulerian gas velocity and (b) the gas volume fraction at $50\mu s$.

Figure 4-13 shows the time history of y-momentum for the Eulerian gas, and Figure 4-14 shows the associated kinetic energy time history. Although the leakage is limited, there are velocities induced in the gas resulting in oscillatory behavior in the y-momentum and kinetic energy.

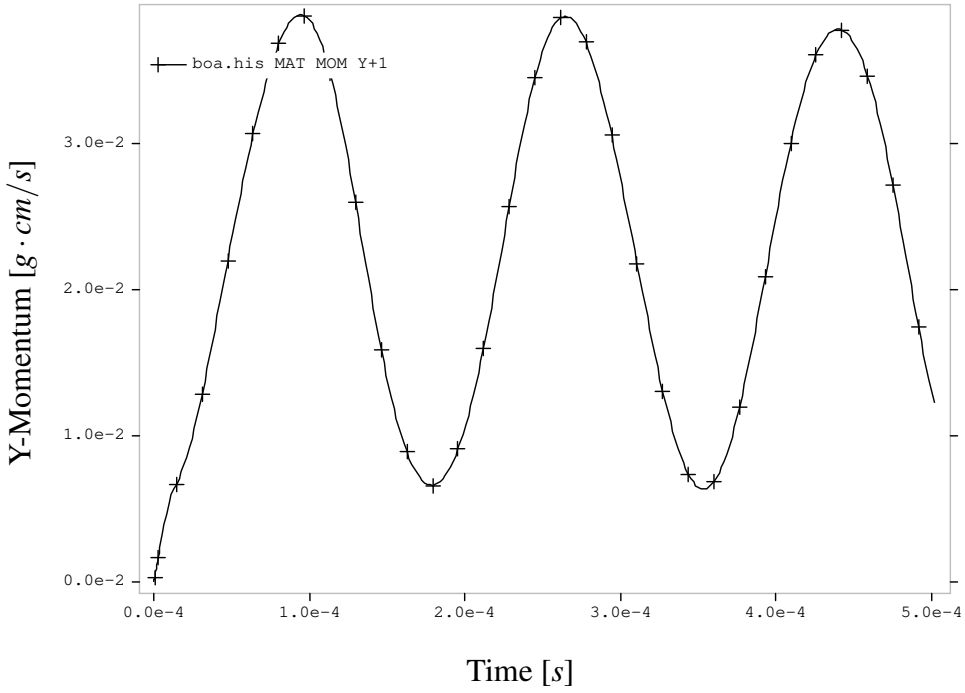

Figure 4-13 Y-momentum time history for the Eulerian gas.

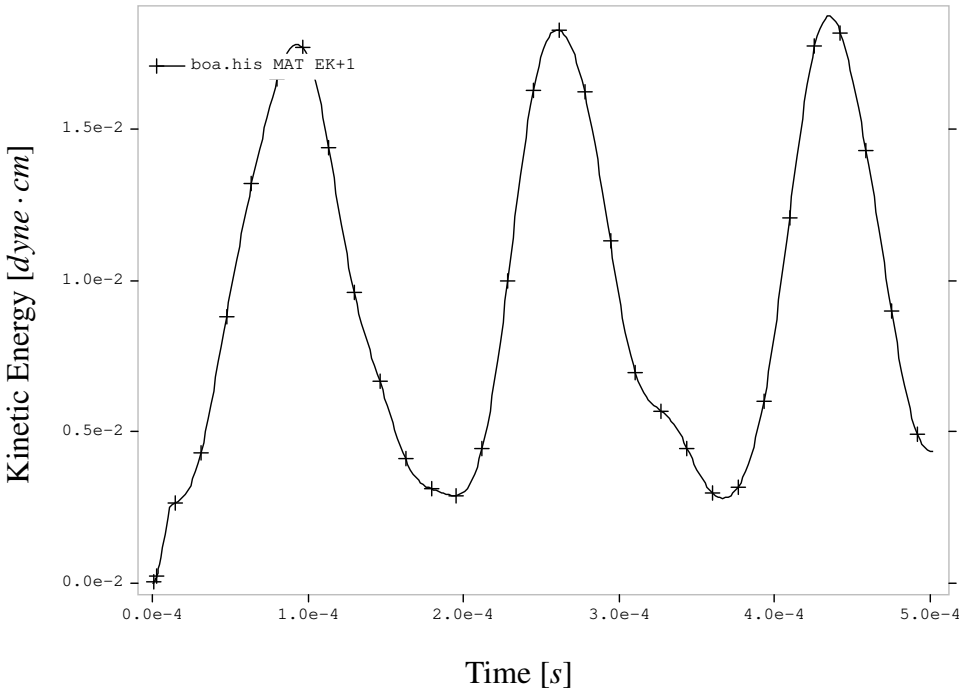

Figure 4-14 Kinetic energy time history for the Eulerian gas.

4.1.6. Static Case, Void Background Material

In this test, void is used as the Eulerian background material, and does not overlap with the region occupied by the Lagrangian body. Figure 4-15 shows snapshots of the Eulerian gas velocity and volume fraction at 50μs. In this period of time, there has been some leakage of gas into the void region where the Lagrangian block resides. This illustrates the nature of the coupling algorithm at the gas-solid interface. The restoring forces slow the progress of the gas, but does not directly enforce any form of no-penetration conditions at the wetted interface. *Similar results are obtained with the quadrature-point method,* **V3-quadrature**.

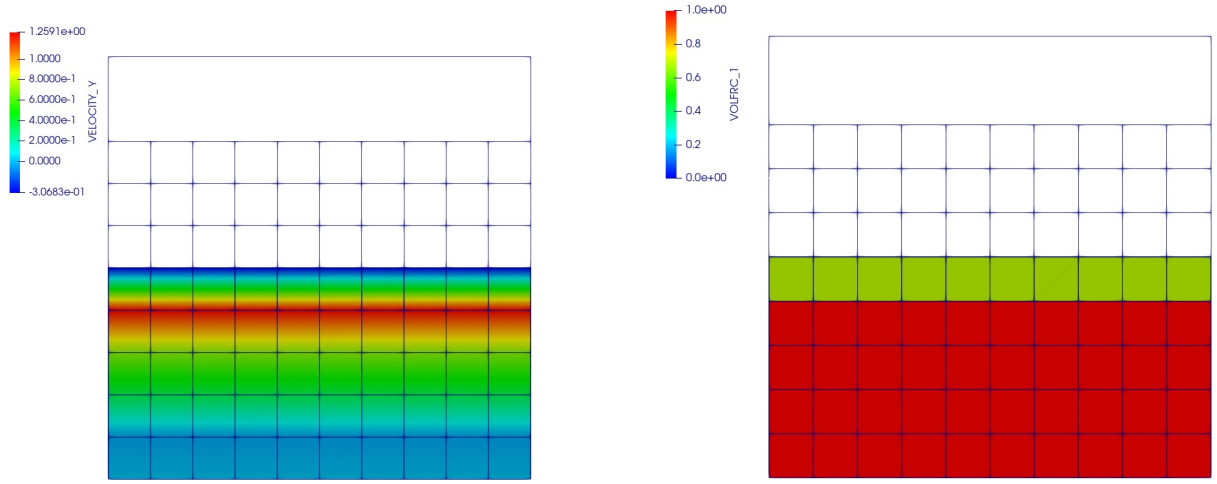

(a) (b)

Figure 4-15 Snapshot of (a) the Eulerian gas velocity and (b) the gas volume fraction at 50μs**.**

Figure 4-16 shows the time history of y-momentum for the Eulerian gas, and Figure 4-17 shows the associated kinetic energy time history. Although the leakage is limited, there are velocities induced in the gas resulting in oscillatory behavior in the y-momentum and kinetic energy.

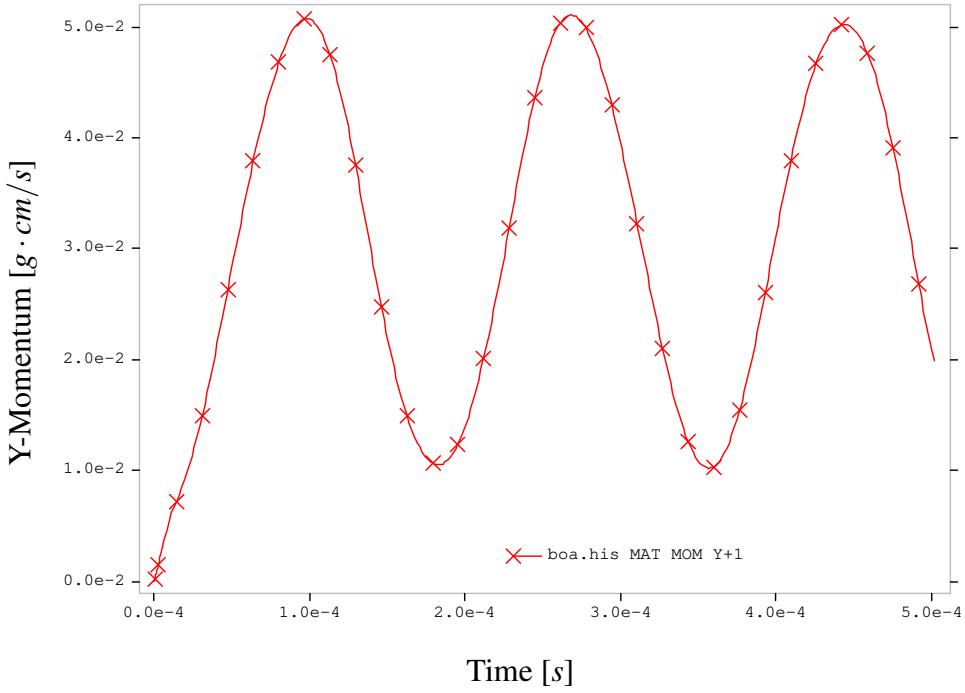

Figure 4-16 Y-momentum time history for the Eulerian gas.

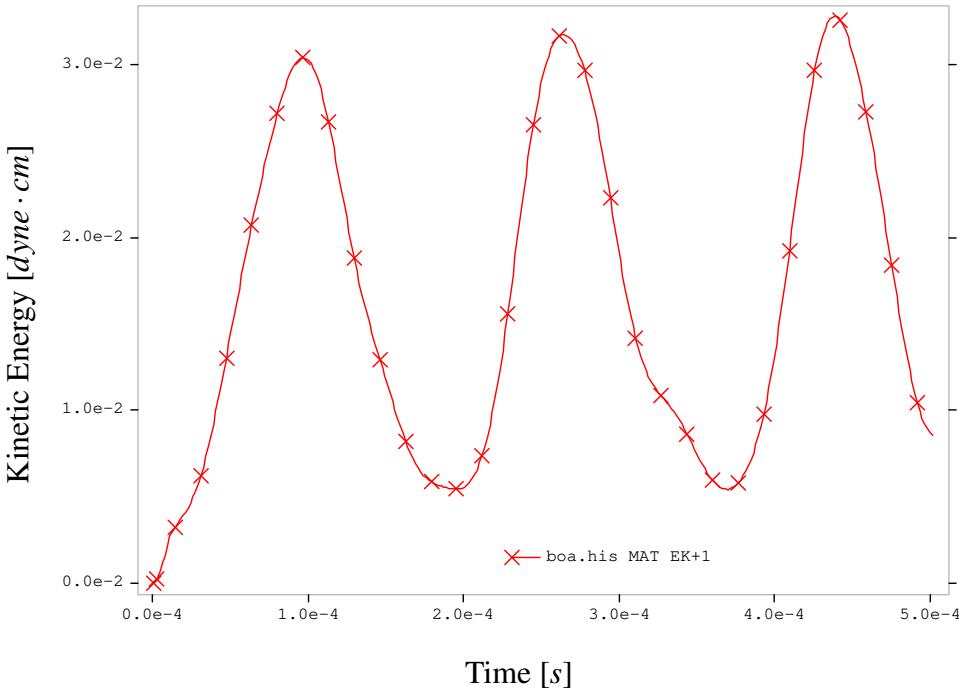

Figure 4-17 Kinetic energy time history for the Eulerian gas.

4.2. Two Ball Impact Test

The two ball impact test model examines a number of different algorithmic aspects of both the Lagrangian-Eulerian coupling, and the inter-material fracture in SABLE. The problem is shown schematically in Figure 4-18. There are two 2.5 cm diameter copper balls. The lower ball has an initial velocity of $50,000$ cm/s, and the upper ball is initially at rest. The Eulerian domain is comprised of void and either one or two copper balls depending on the specific problem configuration.

The material model for the copper balls is linear-elastic with $\rho = 8.83$ g/cm^3, Young's modulus $E = 1.076 \times 10^{12}$ $dynes/cm^2$, and Poisson's ratio $\nu = 0.355$. The KEOS Sesame model is used for the copper equation of state in SABLE.

The Eulerian and coupled solution algorithms permit the use of inter-material fracture. Under tension, the two balls can separate in regions where the Eulerian material exists for both balls. Here, a fracture pressure $P_{frac} = 0$ is used as the criteria for inter-material fracture. For the coupled problems, the x-displacement in the upper ball is constrained at 3 points along the ball center line at the bottom $(4.9, 10.0)$, the middle $(4.9, 12.5)$, and the top $(4.9, 15.0)$.

The different algorithmic cases considered for the two ball impact problem are listed in Table 4-1. Note that only the Eulerian and the coupled case with a matched background material admit inter-material fracture. In the other cases, the impact is purely inelastic, i.e., the spheres stick together after impact.

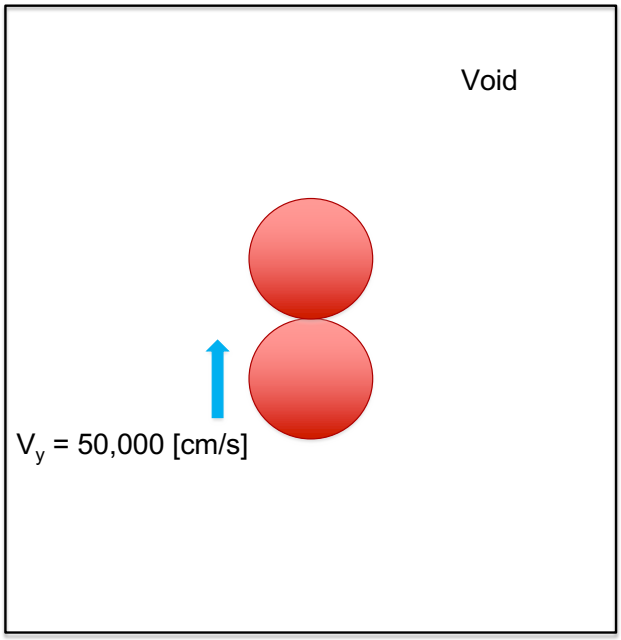

Figure 4-18 Two ball impact geometry.

Case	Background Material	Inter-material Fracture
Eulerian	N/A	No
Eulerian	N/A	Yes
Coupled	Matched	No
Coupled	Matched	Yes
Coupled	Void	No

Table 4-1 Cases considered for the two ball impact problem.

4.2.1. Eulerian

The first Eulerian baseline case does not include inter-material fracture. The y-momentum time histories for the two balls is shown in Figure 4-19. The two balls do not separate, but instead the y-momentum is exchanged between the two balls which together move upward at the average y-momentum. The associated kinetic energy for the inelastic impact is shown in Figure 4-20.

For this problem, Lagrangian tracers were positioned at the center of each ball. Figure 4-21 shows the y-position history, and Figure 4-22 shows the associated y-velocity.

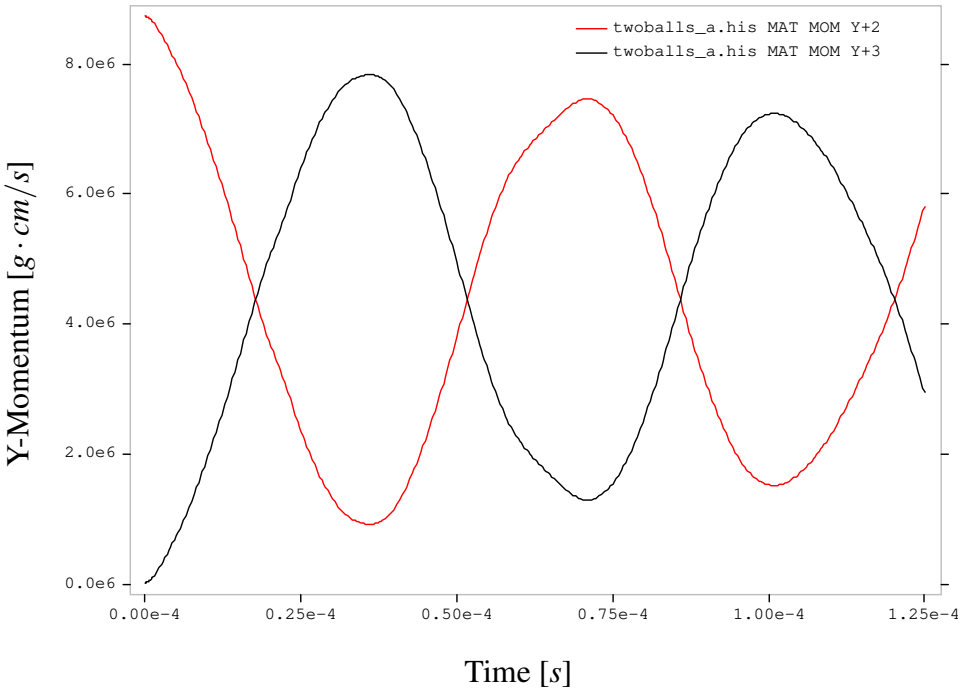

Figure 4-19 Y-momentum time histories for lower (–) and upper (–) copper balls.

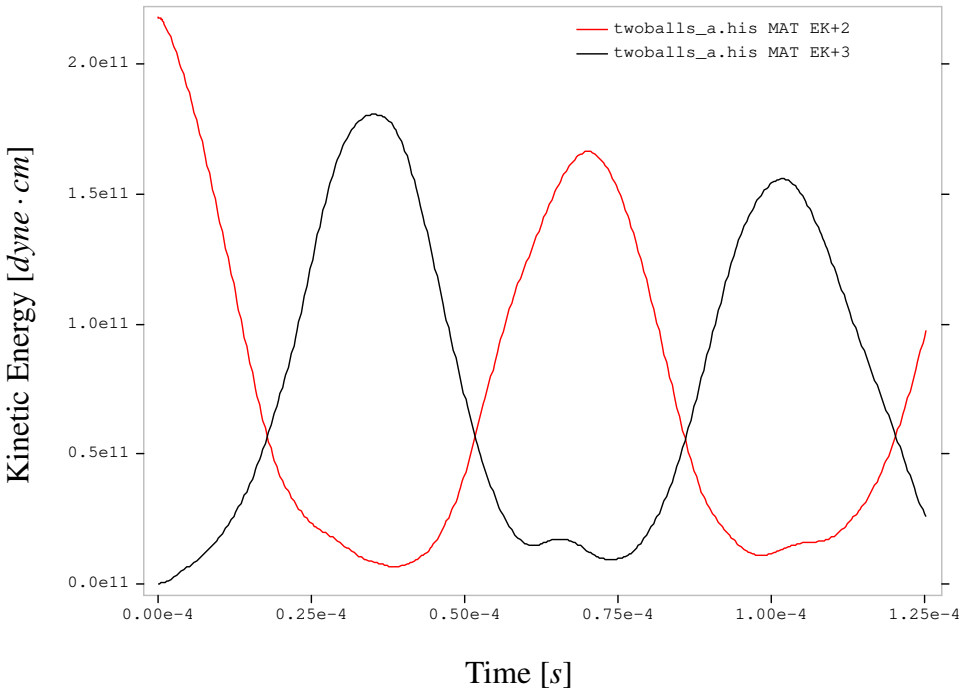

Figure 4-20 Kinetic energy time histories for lower (–) and upper (–) copper balls.

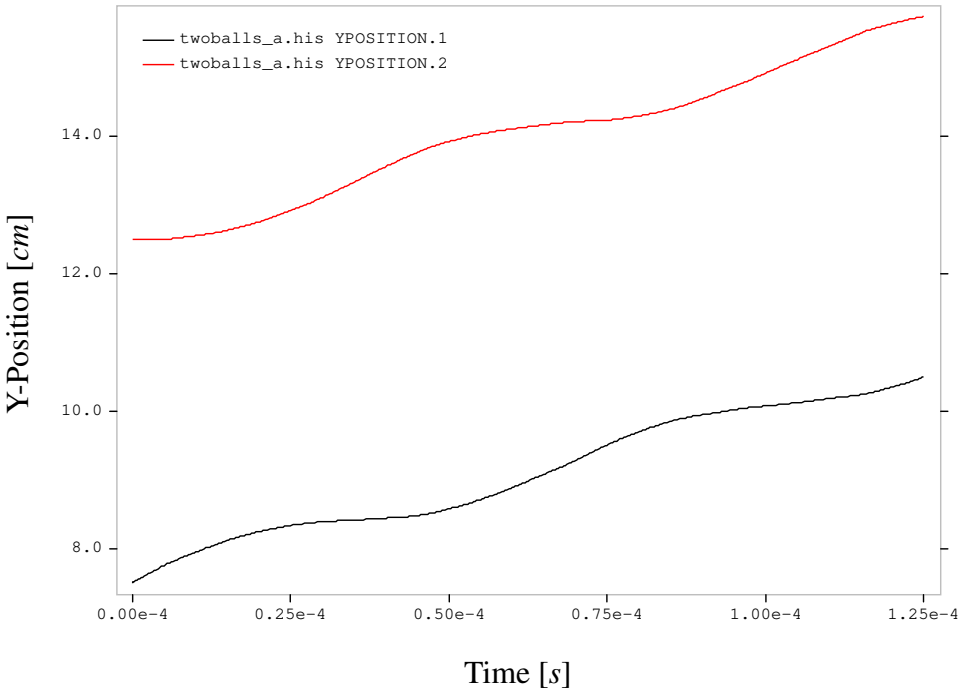

Figure 4-21 Y-position time histories for lower (–) and upper (–) copper balls.

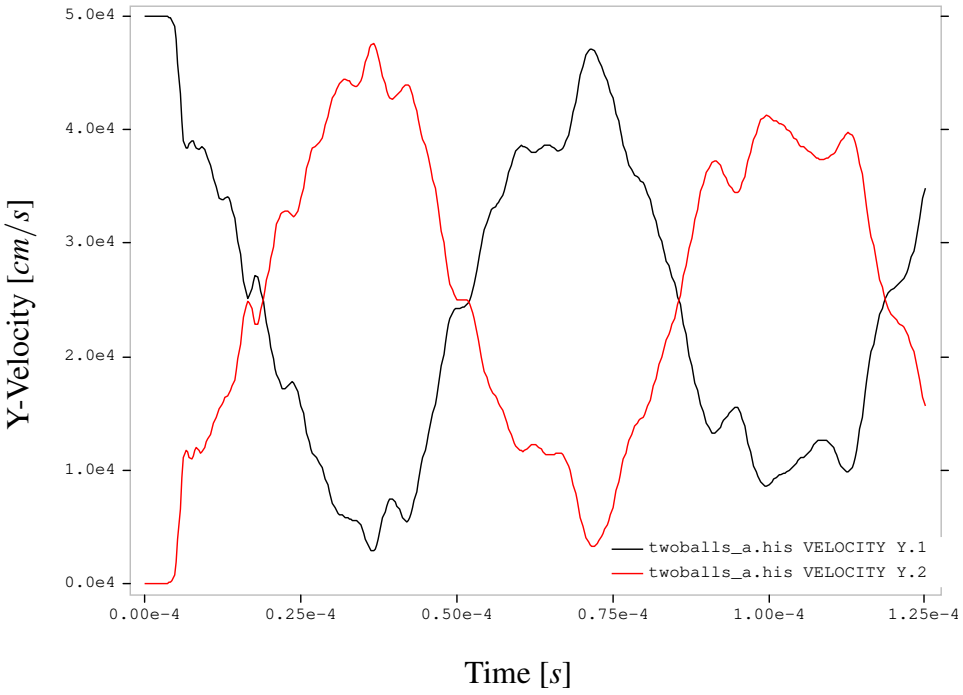

Figure 4-22 Y-velocity time histories for lower (–) and upper (–) copper balls.

4.2.2. *Eulerian – with Inter-material Fracture*

The second Eulerian baseline uses inter-material fracture between the copper balls. This permits post-impact separation, albeit with noticeable inelastic features. Figure 4-23 shows the y-momentum time-histories for this case. The post-impact rigid-body translation for each ball is clearly seen starting at $t \approx 0.5 \times 10^{-4}\ s$. The kinetic energy time-histories are shown in Figure 4-24. The tracer time-histories for y-position and y-velocity are shown in Figures 4-25 and 4-26 respectively

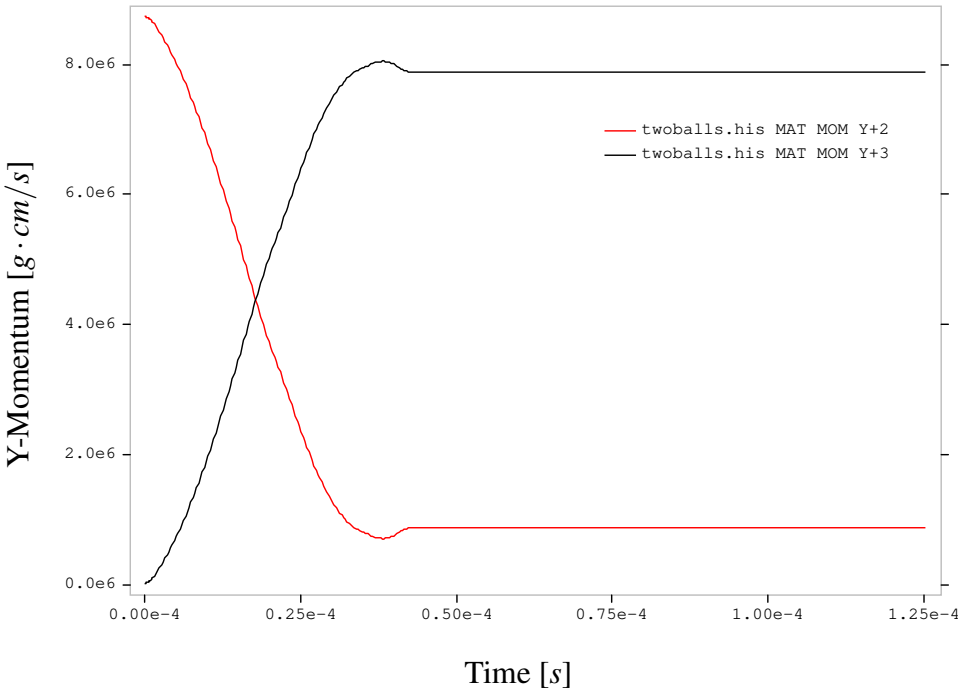

Figure 4-23 Y-momentum time histories for lower (–) and upper (–) copper balls.

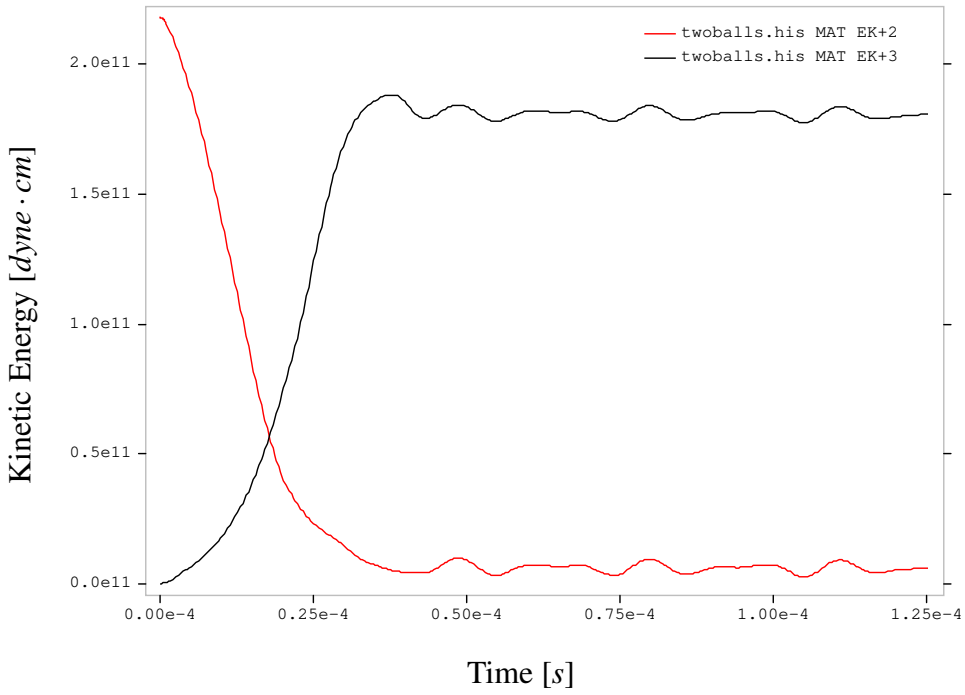

Figure 4-24 Kinetic energy time histories for lower (–) and upper (–) copper balls.

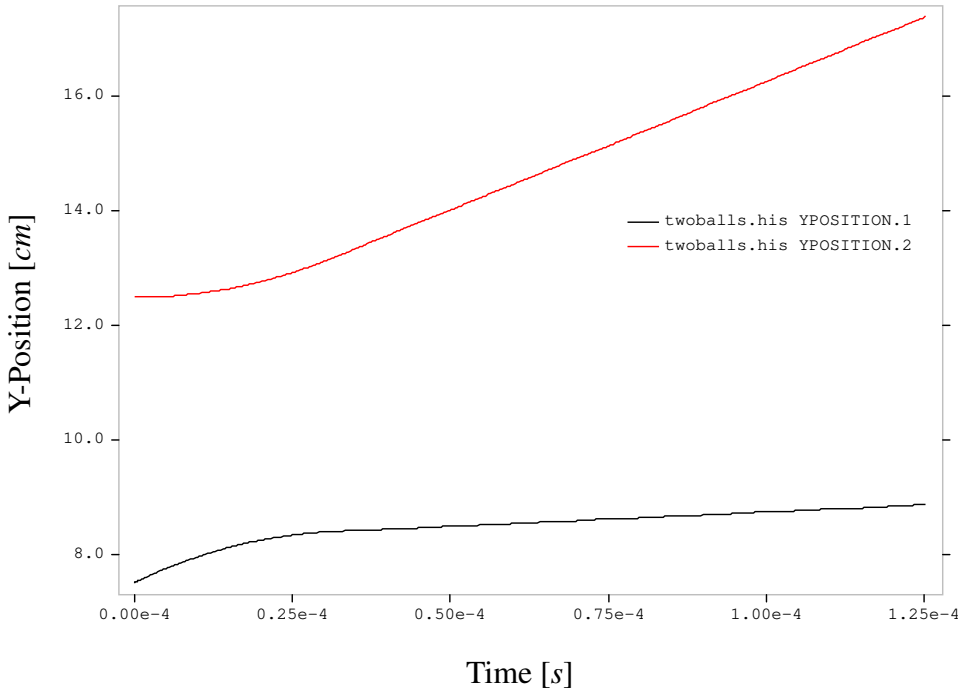

Figure 4-25 Y-position time histories for lower (–) and upper (–) copper balls.

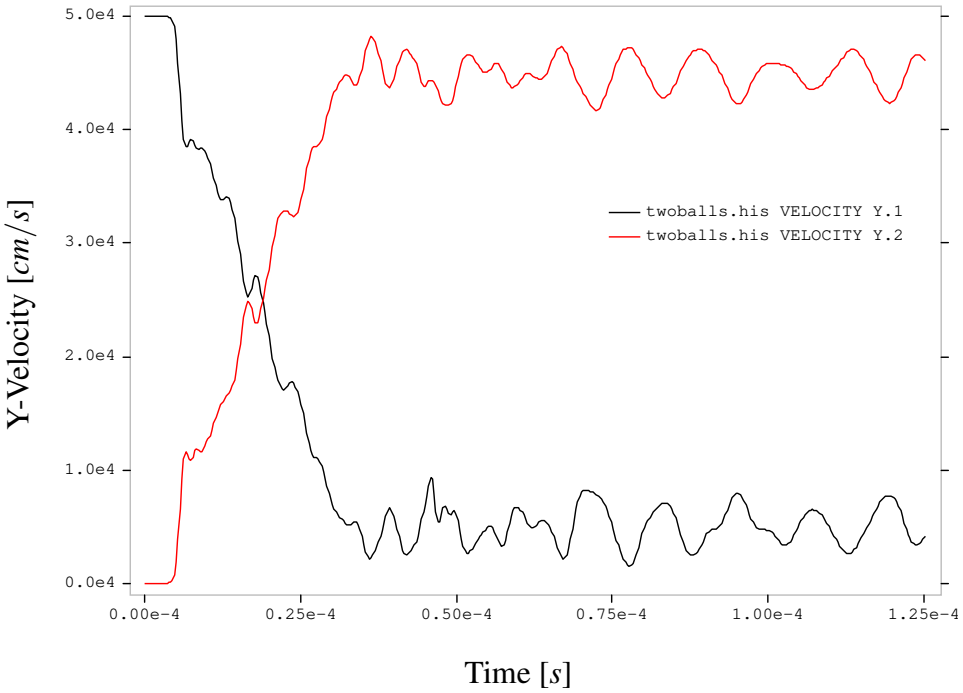

Figure 4-26 Y-velocity time histories for lower (–) and upper (–) copper balls.

4.2.3. Coupled, Matched Background Material

Turning to the coupled simulations, this case uses a matched background material in the Eulerian mesh where the upper Lagrangian ball is located. Inter-material fracture is not included in this problem, so the impact is purely inelastic.

Figures 4-27 and 4-28 show the y-momentum and kinetic energy time histories for the coupled and Eulerian simulations. Figures 4-29 and 4-30 show the y-position and y-velocity time histories for the coupled and Eulerian simulations. There is a surprising divergence between the overall dynamic response for the coupled and Eulerian baseline calculations. In general, the Lagrangian dynamic response is more energetic with higher post-impact peak velocities. At this time, a clear explanation for the differences between the coupled and Eulerian baseline calculation has not been determined.

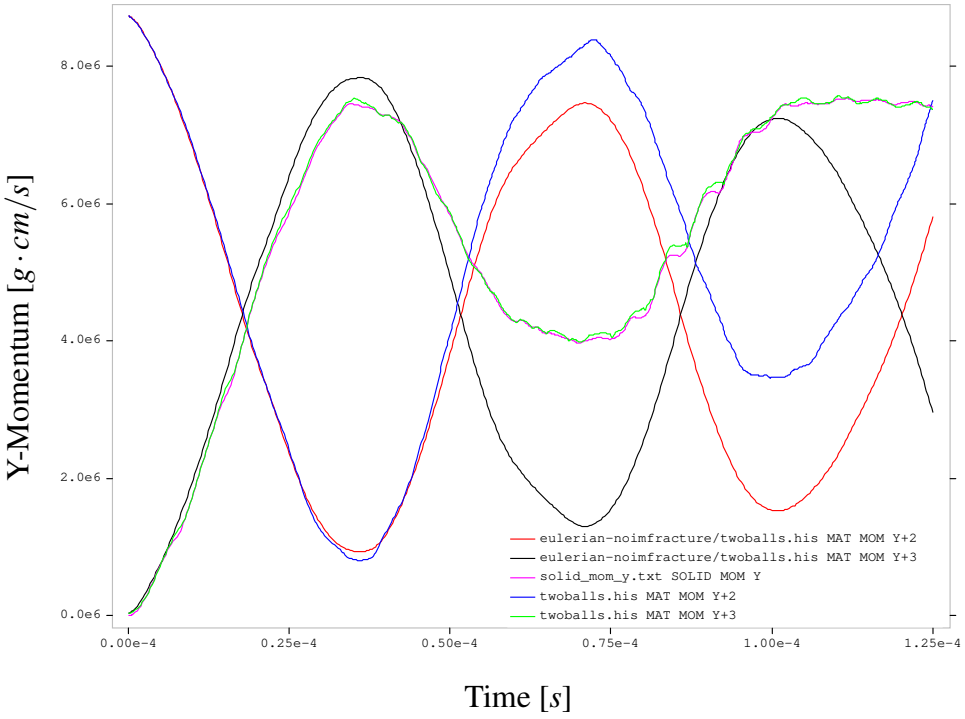

Figure 4-27 Y-momentum time histories for the lower (–) and upper Eulerian (–) balls and the Lagrangian (–) copper ball in the coupled calculation. The baseline Eulerian y-momentum histories are shown for the lower (–) and upper (–) balls.

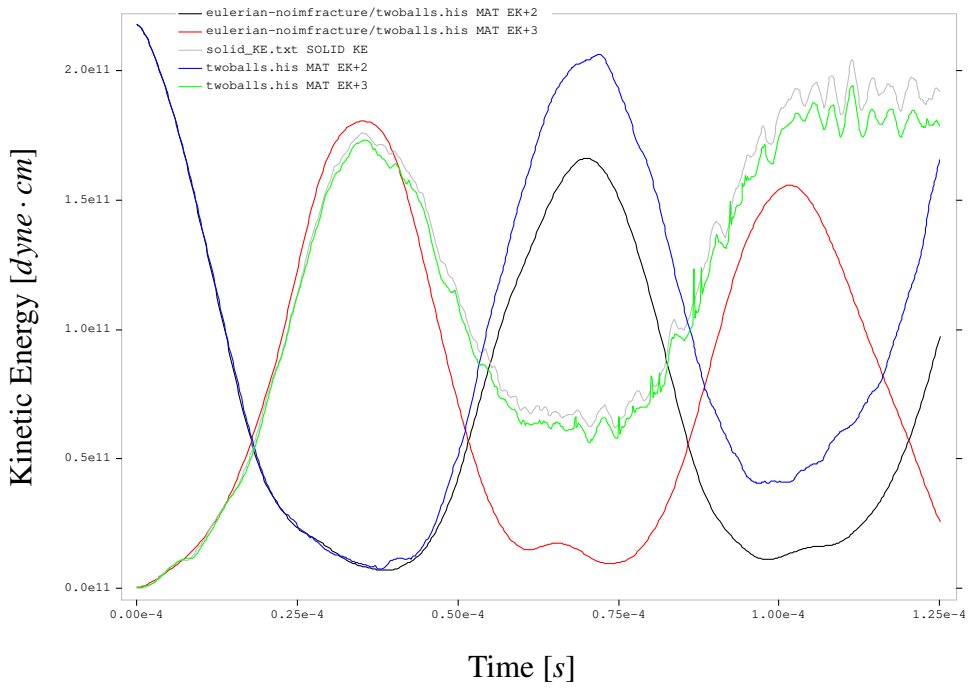

Figure 4-28 Kinetic energy time histories for the lower (–), upper Eulerian (–) and Lagrangian (–) copper balls in the coupled calculation. The Eulerian baseline histories are shown for the lower (–) and upper (–) balls.

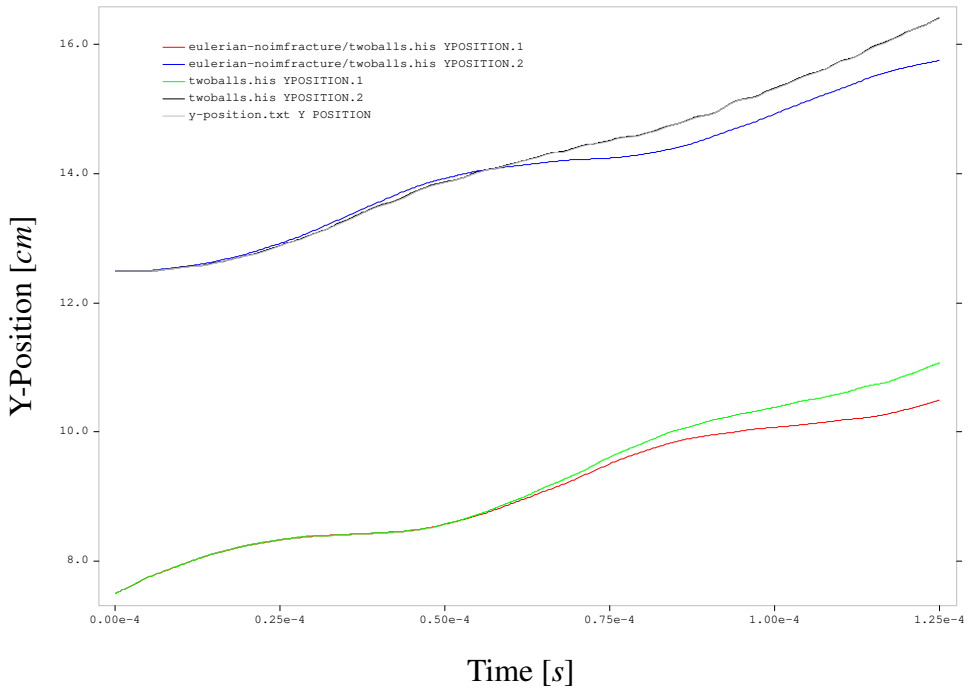

Figure 4-29 Y-position time histories for the lower (–), upper Eulerian (–) and Lagrangian (–) copper balls in the coupled calculation. The Eulerian baseline histories are shown for the lower (–) and upper (–) balls.

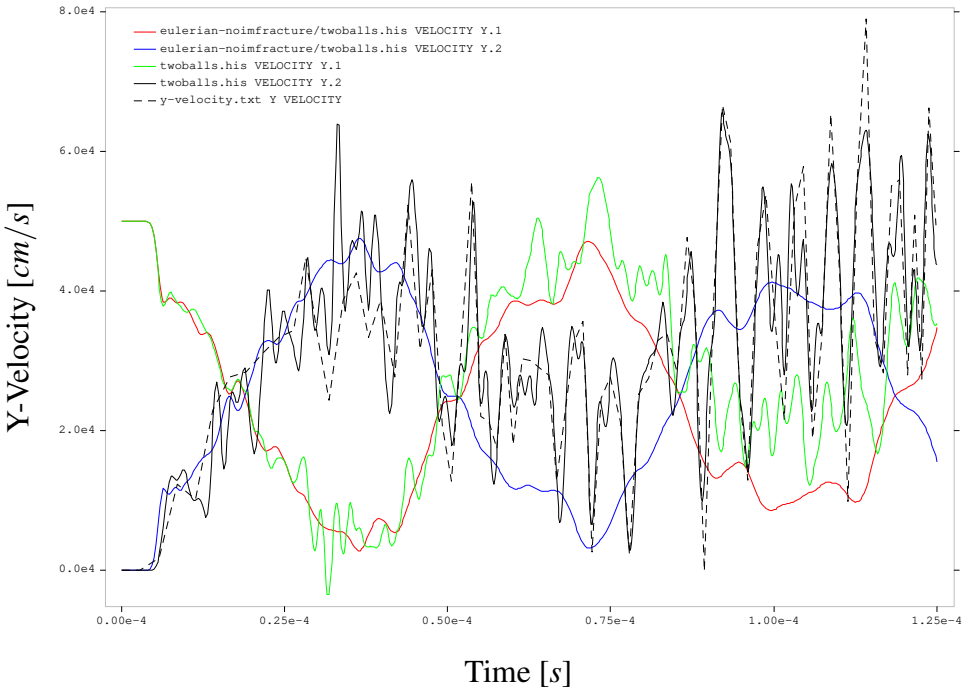

Figure 4-30 Y-velocity time histories for the lower (–), upper Eulerian (–) and Lagrangian (- -) copper balls in the coupled calculation. The Eulerian baseline histories are shown for the lower (–) and upper (–) balls.

4.2.4. Coupled, Matched Background Material, Inter-material Fracture

This coupled case uses a matched background material in the Eulerian mesh where the upper Lagrangian ball is located. Inter-material fracture is used to permit post-impact separation of the copper balls.

Figures 4-31 and 4-32 show the y-momentum and kinetic energy time histories for the coupled and Eulerian simulations. The y-momentum reveals the post-impact separation between the balls, but also shows a lower post-impact momentum for the Lagrangian ball. In addition, the post-impact Lagrangian momentum is noisy, and the cause for this has not been determined. The kinetic energy for the Lagrangian ball shows similar behavior.

Figures 4-33 and 4-34 show the y-position and y-velocity time histories for the coupled and Eulerian simulations. The y-position shows that bulk vertical motion of the Lagrangian ball is slightly slower than the corresponding Eulerian motion. Figure 4-34 shows that both the Lagrangian and Eulerian (background) balls have significantly higher frequency content with larger amplitude variations. The primary source for this behavior has not been identified.

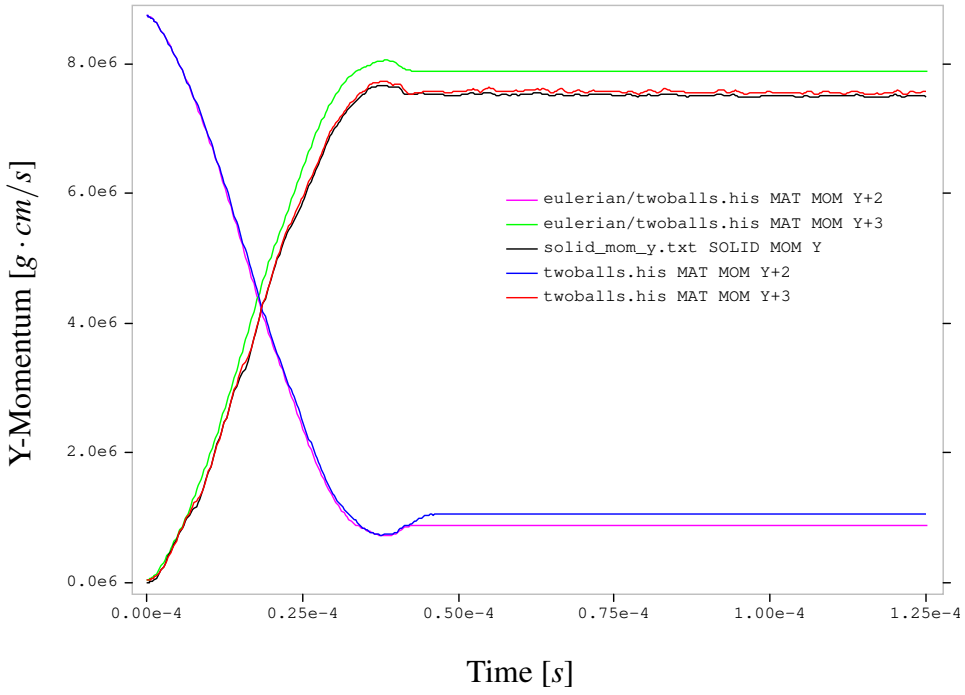

Figure 4-31 Y-momentum time histories for the lower (–), upper Eulerian (–) and Lagrangian (–) copper balls with the Eulerian baseline histories for the lower (–) and upper (–) balls.

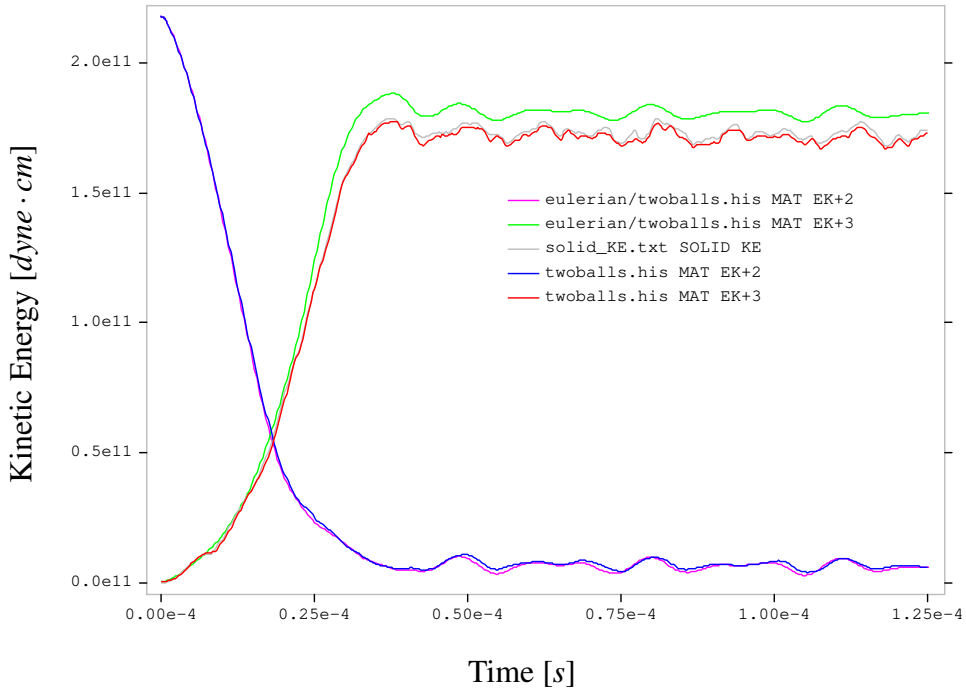

Figure 4-32 Kinetic energy time histories for the lower (–), upper Eulerian (–) and Lagrangian (–) copper balls with the Eulerian baseline histories for the lower (–) and upper (–) balls.

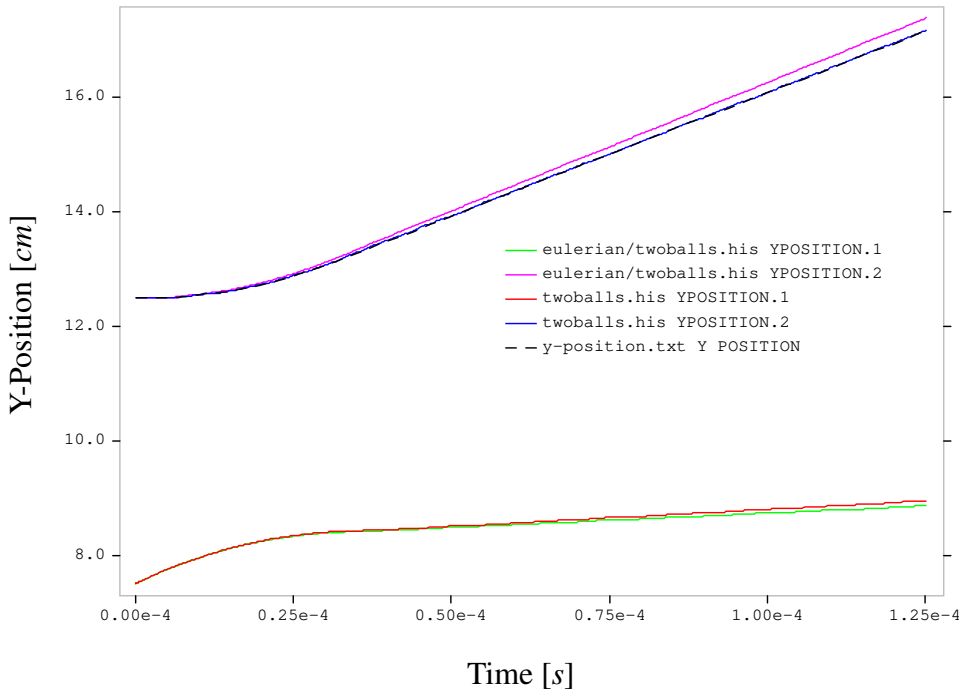

Figure 4-33 Y-position time histories for the lower (–), upper Eulerian (–) and Lagrangian (- -) copper balls with the Eulerian baseline histories for the lower (–) and upper (–) balls.

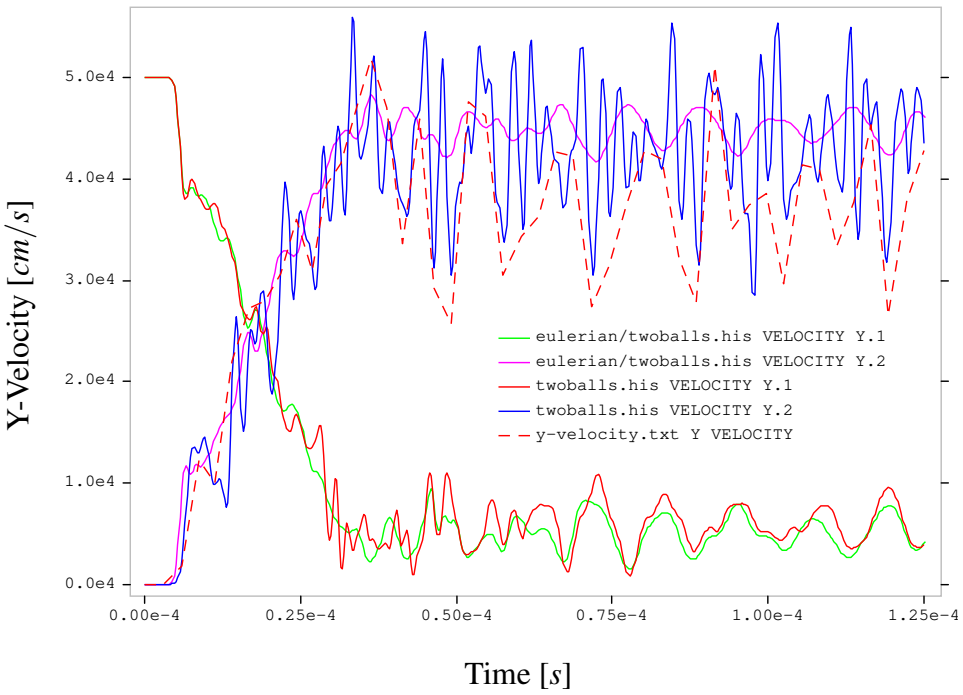

Figure 4-34 Y-velocity time histories for the lower (–), upper Eulerian (–) and Lagrangian (- -) copper balls with the Eulerian baseline histories for the lower (–) and upper (–) balls.

4.2.5. Coupled, Void Background Material

This coupled case uses void for the background material in the Eulerian mesh where the upper Lagrangian ball is located. Inter-material fracture can not be used, so the impact is inelastic.

Figures 4-35 and 4-36 show the y-momentum and kinetic energy time histories for the coupled and Eulerian simulations. Although the y-momentum for the Lagrangian ball appears to behave better relative to the coupled case with a matched background material, the kinetic energy for the Lagrangian ball deviates significantly from its Eulerian counterpart. In addition, the high-frequencies super-imposed on the overall periodic behavior is clear. The cause of this behavior has not been clearly identified.

Figures 4-37 and 4-38 show the y-position and y-velocity time histories for the coupled and Eulerian simulations. Again, the dynamic response of the Lagrangian ball is much more energetic, and diverges from the Eulerian counterpart.

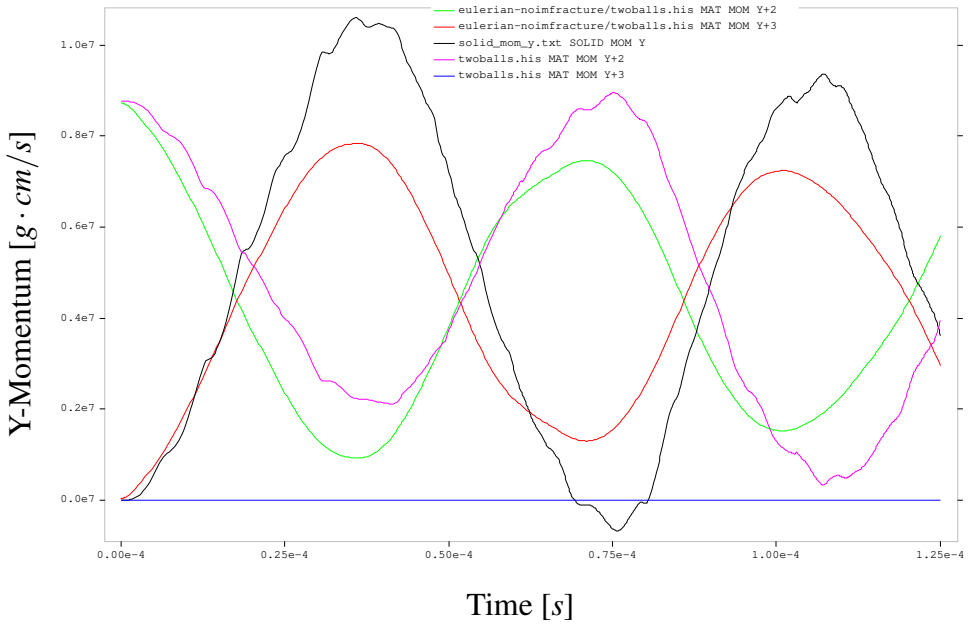

Figure 4-35 Y-momentum time histories for the lower (–), void (–) and Lagrangian (–) copper balls with the Eulerian baseline histories for the lower (–) and upper (–) balls.

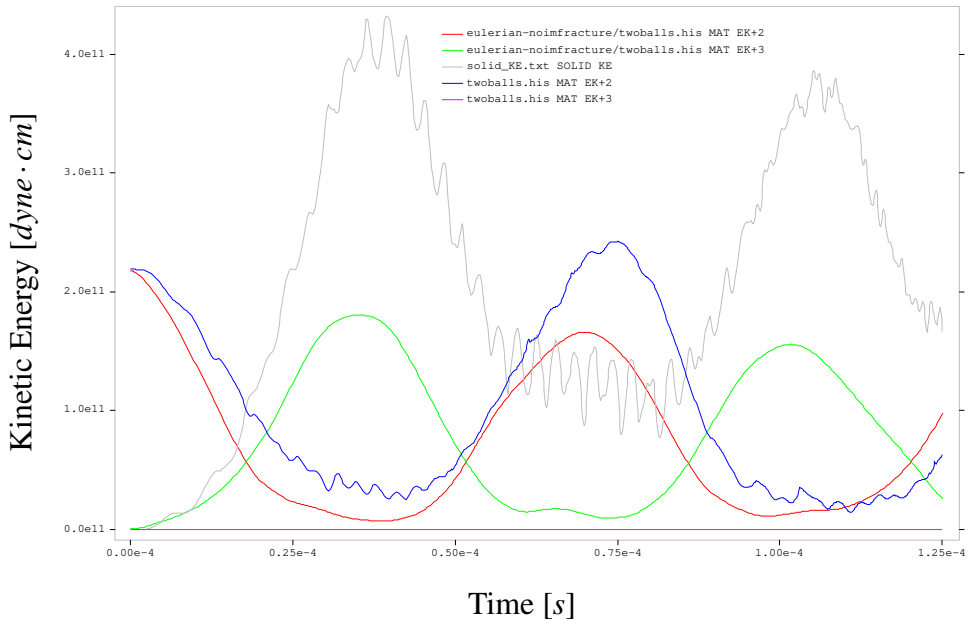

Figure 4-36 Kinetic energy time histories for the lower (–), void (–) and Lagrangian (–) copper balls with the Eulerian baseline histories for the lower (–) and upper (–) balls.

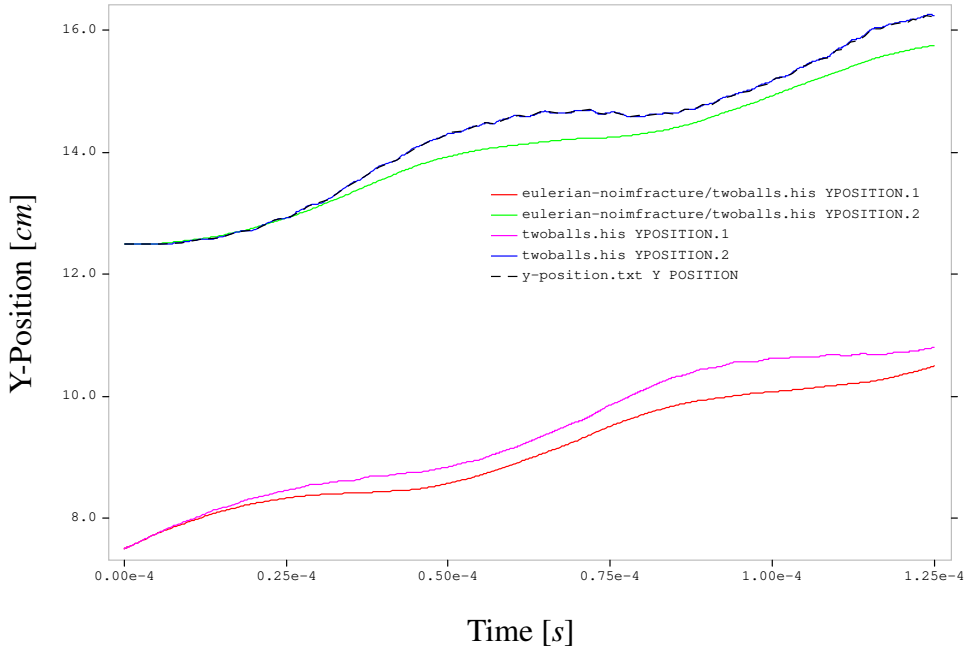

Figure 4-37 Y-position time histories for the lower (–), upper Eulerian (–) and Lagrangian (- -) copper balls with the Eulerian baseline histories for the lower (–) and upper (–) balls.

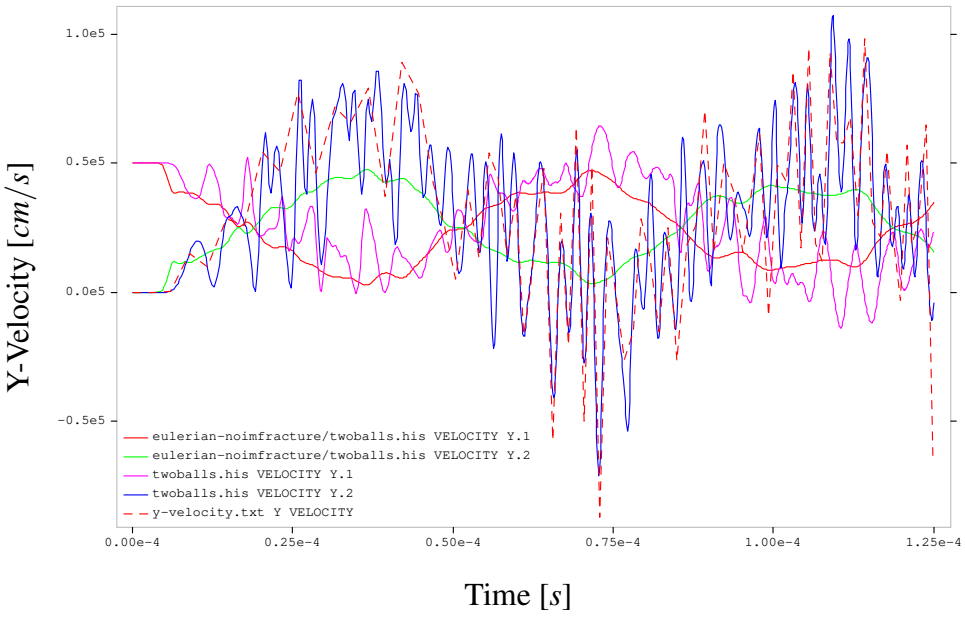

Figure 4-38 Y-velocity time histories for the lower (–), upper Eulerian (–) and Lagrangian (- -) copper balls with the Eulerian baseline histories for the lower (–) and upper (–) balls.

4.3. Normal Hemispherical Penetrator

The hemispherical penetrator problem geometry is shown in Figure 4-39. The penetrator is 4340 steel with density $\rho = 7.8724\ g/cm^3$, Young's modulus $E = 2 \times 10^{12}\ dynes/cm^2$, and Poisson's ratio $\nu = 0.28$. The target material is a 23 MPa concrete with density $\rho = 2.040\ g/cm^3$, yield stress $Y = 4.189 \times 10^{10}\ dynes/cm^2$, Poisson's ratio $\nu = 0.345$, and a fracture pressure $P_{frac} = -2.0 \times 10^9\ dynes/cm^2$.

The overall Eulerian domain uses a mesh size of $0.1\ cm$, and spans a square domain $(-12.8, -12.8) \leq (x, y) \leq (12.8, 12.8)\ cm$. For the Eulerian calculation, the penetrator uses the "K and C" SESAME equation of state, and the target uses a KEOS Mie Gruüneisen EOS. The target yield model uses the "CTH GEO" model and associated void insertion model for fracture. In the first calculation, void is used in the region above the target, and in the subsequent case, air is used in the region above the target.

The target material has no-displacement conditions prescribed on the bottom and vertical sides and is initially at rest. The normal-impact penetrator has an initial downward velocity $v_y = -50,000\ cm/s$. A total simulation time of $500\mu s$ is used for all simulations. For the Eulerian calculations, a Lagrangian tracer is placed at the tip of the penetrator to measure the overall penetration depth.

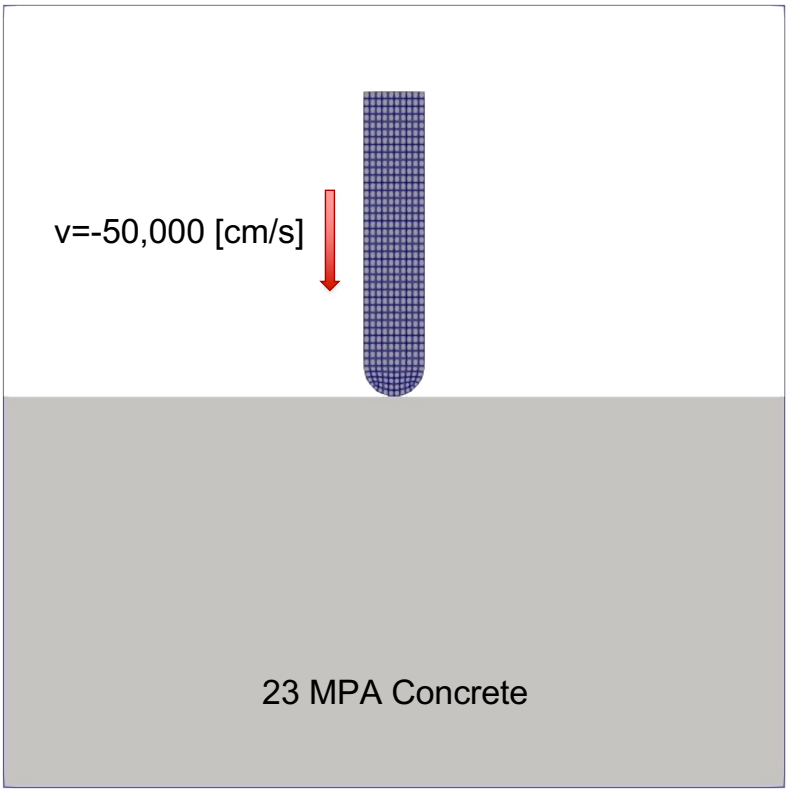

Figure 4-39 Hemispherical penetrator and concrete target.

4.3.1. Force-Coupling, Void Background

This case uses a void background where the Lagrangian penetrator overlaps the Eulerian mesh. The penetration depth, measured at the tip of the penetrator, is shown in Table 4-2 for the Eulerian and coupled simulations. The coupled simulation over-predicts the penetration depth relative to the Eulerian calculation by 7.0%.

Figures 4-40 and 4-41 show the time-histories for the penetrator momentum and kinetic energy for the Eulerian and coupled simulations. The momentum time-history shows that the Lagrangian penetrator loses slightly less momentum, i.e., is moving faster over the course of the simulation. This correlates with the kinetic energy histories where the Lagrangian penetrator has slightly higher kinetic energy values over the course of the coupled simulation.

The concrete target time histories for y-momentum and kinetic energy are shown in Figures 4-42 and 4-43. The coupled calculation captures all of the primary features of the Eulerian y-momentum and kinetic energy histories. Here, there is a somewhat noticeable time shift with the coupled results slightly lagging the Eulerian calculation. Although less pronounced in the velocity and kinetic energy histories, this effect is due to the fact that the coupling forces (stress and acceleration) require some small overlap between the Eulerian and Lagrangian meshes. This results in a slight delay in time for the penetrator and target to begin interacting.

Figure 4-44 shows the snapshots of the velocity field at $t = 50\mu s$ for the Eulerian and coupled Eulerian-Lagrangian simulations. The coupled simulation predicts a peak velocity magnitude 28% larger than the Eulerian simulation. The 7.0% larger penetration depth for the coupled simulation is also clear in Figure 4-44. Surprisingly, the boundary of the target surrounding the penetrator is qualitatively more symmetric than its Eulerian counterpart.

Simulation	Penetration Depth [cm]
Eulerian	8.1590
Coupled	8.7308

Table 4-2 Penetration depth based on the tip of the penetrator for Eulerian and coupled simulations at $t = 500\mu s$.

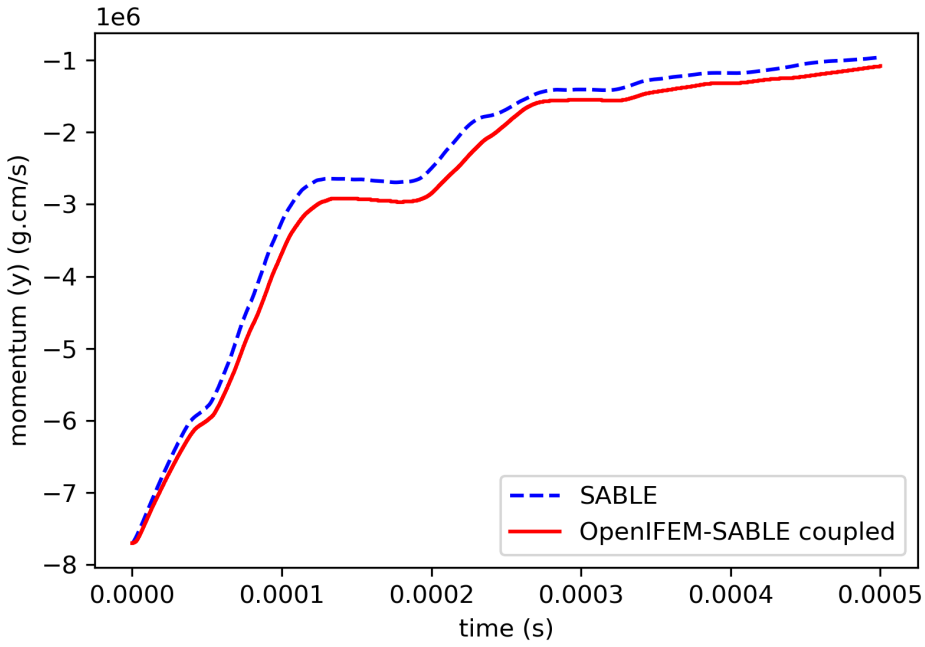

Figure 4-40 Penetrator y-momentum time history for the Eulerian (- -) and coupled Eulerian-Lagrangian (–) calculations.

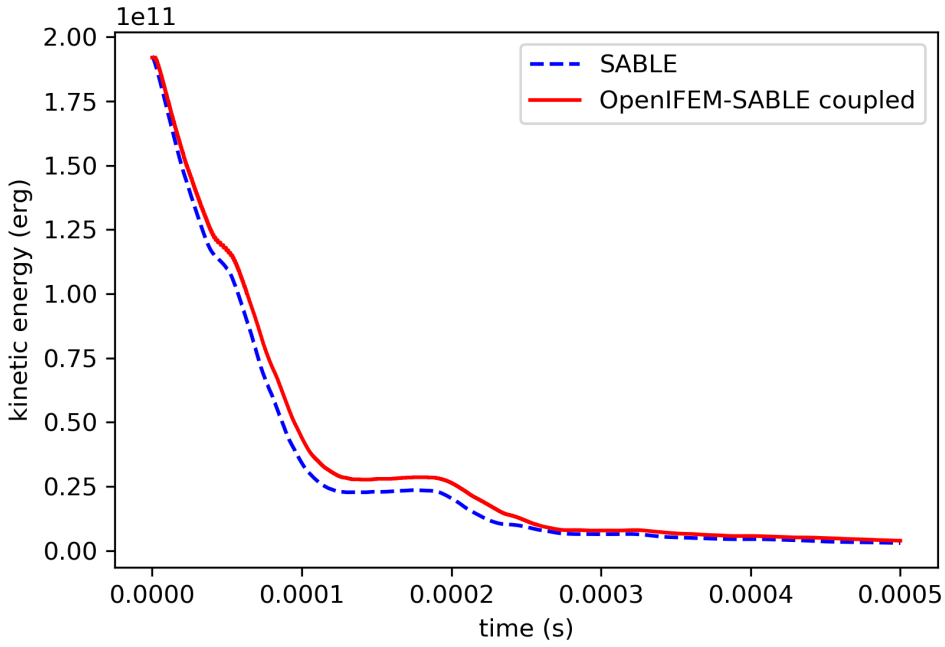

Figure 4-41 Penetrator kinetic energy time history for the Eulerian (- -) and coupled Eulerian-Lagrangian (–) calculations.

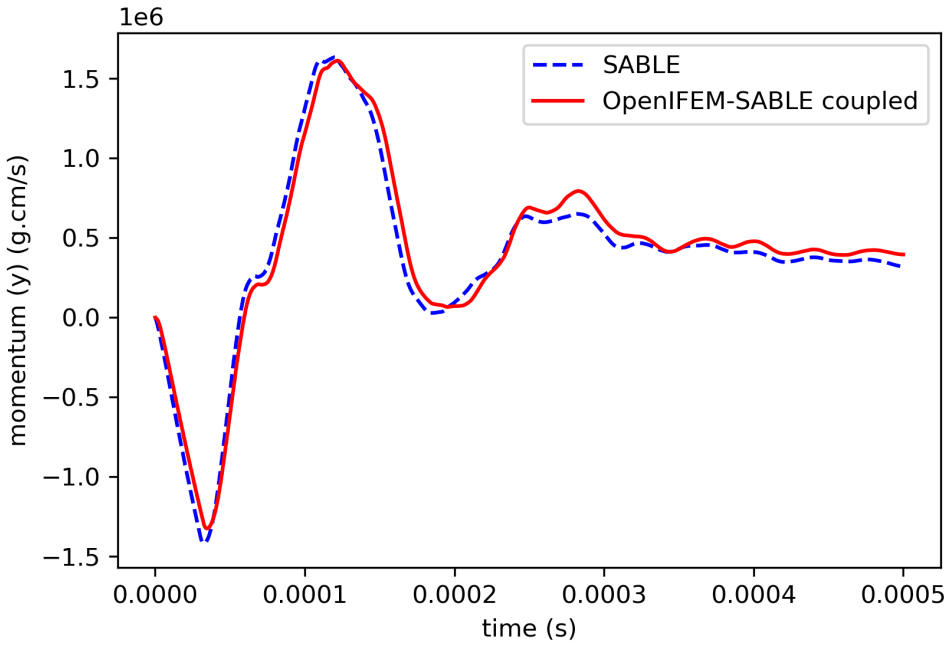

Figure 4-42 Target y-momentum time history for the Eulerian (- -) and coupled Eulerian-Lagrangian (–) calculations.

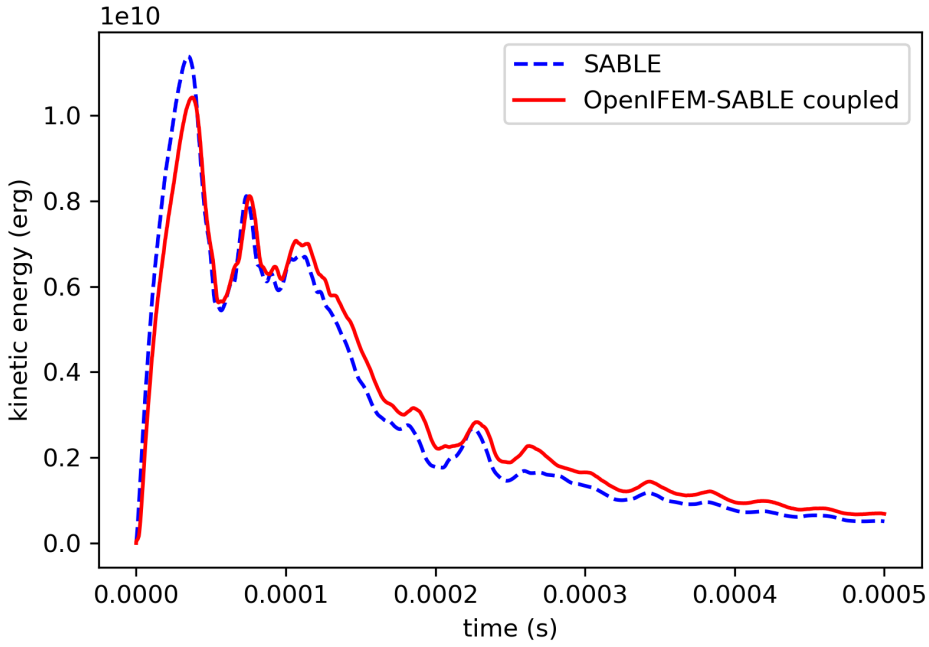

Figure 4-43 Target kinetic energy time history for the Eulerian (- -) and coupled Eulerian-Lagrangian (–) calculations.

(a)

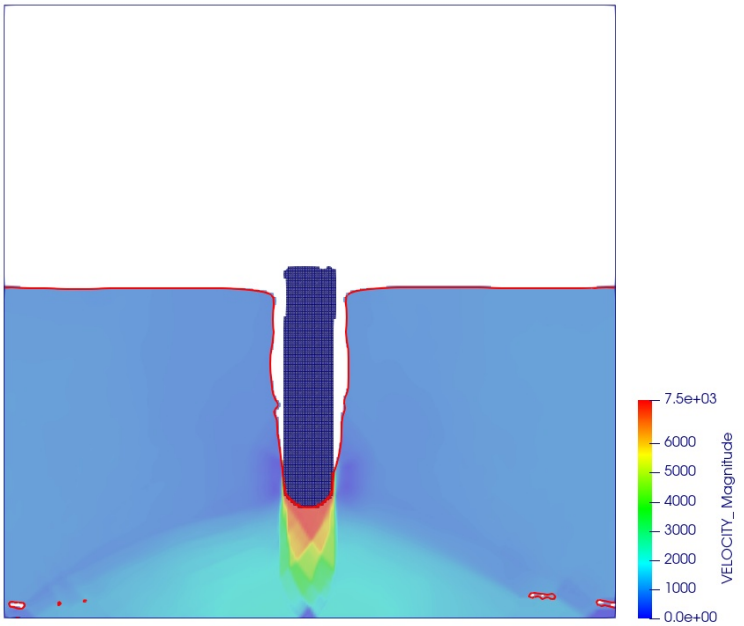

(b)

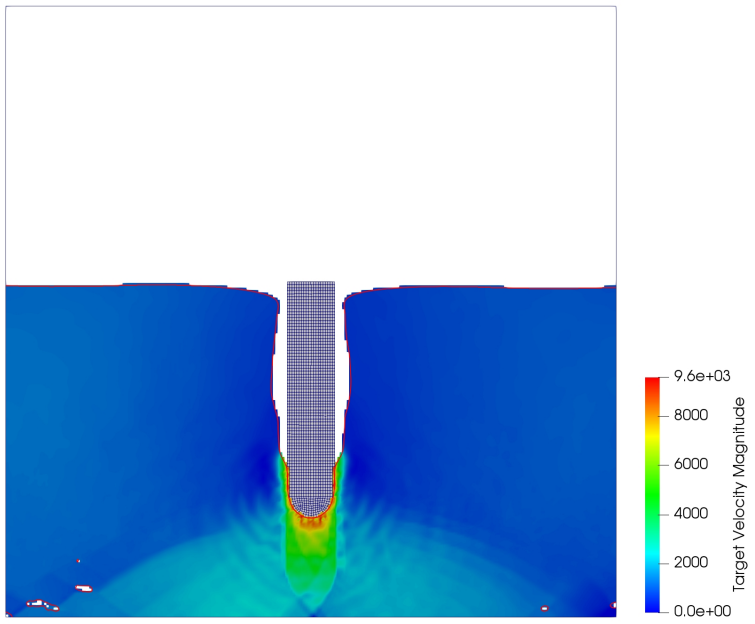

Figure 4-44 Target velocity magnitude at $t = 50\mu s$ for (a) the Eulerian, and (b) the coupled Eulerian-Lagrangian calculations.

4.3.2. Force-Coupling, Air Background

The coupled simulation presented here uses air as the background material in the overlap region between the penetrator and the Eulerian domain. In addition, air is used rather than void in the region above the concrete target. The penetration depths for the Eulerian and coupled simulations are shown in Table 4-3 and are unchanged relative to the values reported in Table 4-2

Figures 4-45 and 4-46 show the time-histories for the penetrator momentum and kinetic energy for the Eulerian and coupled simulations. The momentum time-history shows that the Lagrangian penetrator loses slightly less momentum, i.e., is moving faster over the course of the simulation. This correlates with the kinetic energy histories where the Lagrangian penetrator has slightly higher kinetic energy values over the course of the coupled simulation.

The concrete target time histories for y-momentum and kinetic energy are shown in Figures 4-47 and 4-48. The coupled calculation captures all of the primary features of the Eulerian y-momentum and kinetic energy histories. Here, there is a somewhat noticeable time shift with the coupled results slightly lagging the Eulerian calculation. Although less pronounced in the velocity and kinetic energy histories, this effect is due to the fact that the coupling forces (stress and acceleration) require some small overlap between the Eulerian and Lagrangian meshes. This results in a slight delay in time for the penetrator and target to begin interacting.

Figures 4-49 and 4-50 show snapshots of the x- and y-velocity fields at $t = 50\mu s$ for the Eulerian and coupled Eulerian-Lagrangian simulations.

Simulation	Penetration Depth [cm]
Eulerian	8.1590
Coupled	8.7308

Table 4-3 Penetration depth based on the tip of the penetrator for Eulerian and coupled simulations at $t = 500\mu s$.

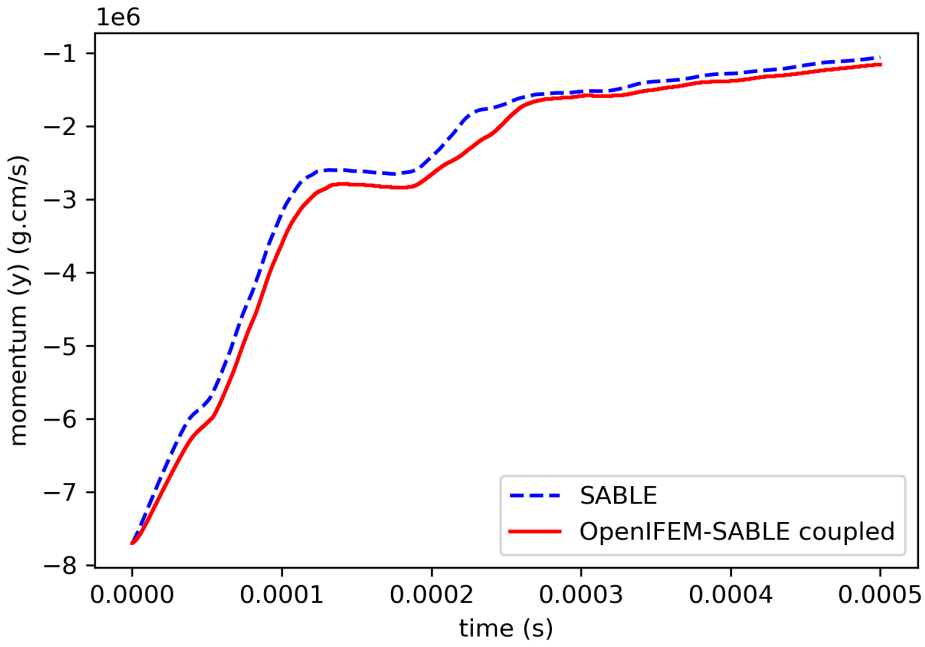

Figure 4-45 Penetrator y-momentum time history for the Eulerian (- -) and coupled Eulerian-Lagrangian (–) calculations.

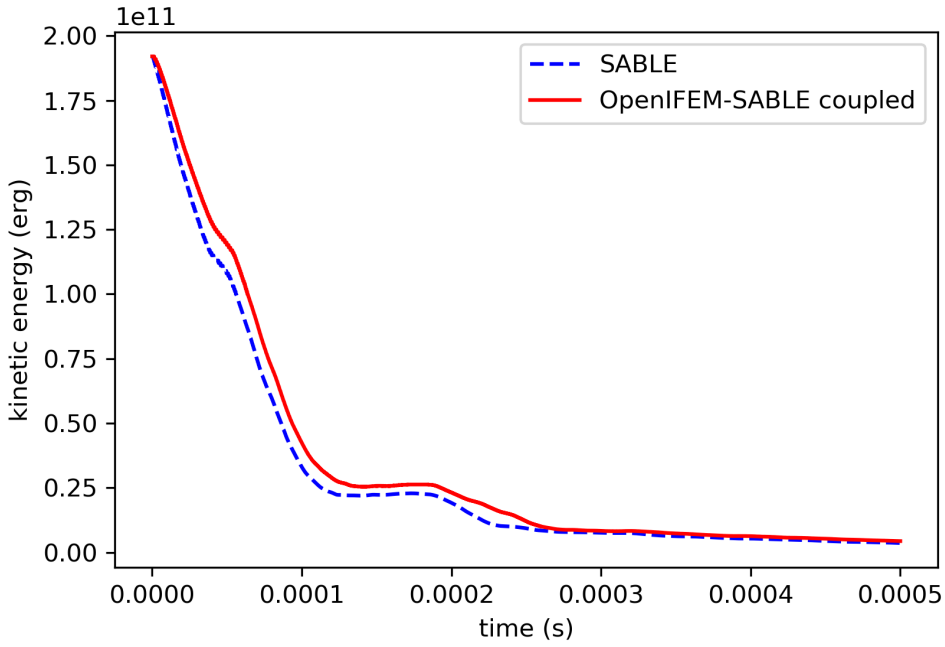

Figure 4-46 Penetrator kinetic energy time history for the Eulerian (- -) and coupled Eulerian-Lagrangian (–) calculations.

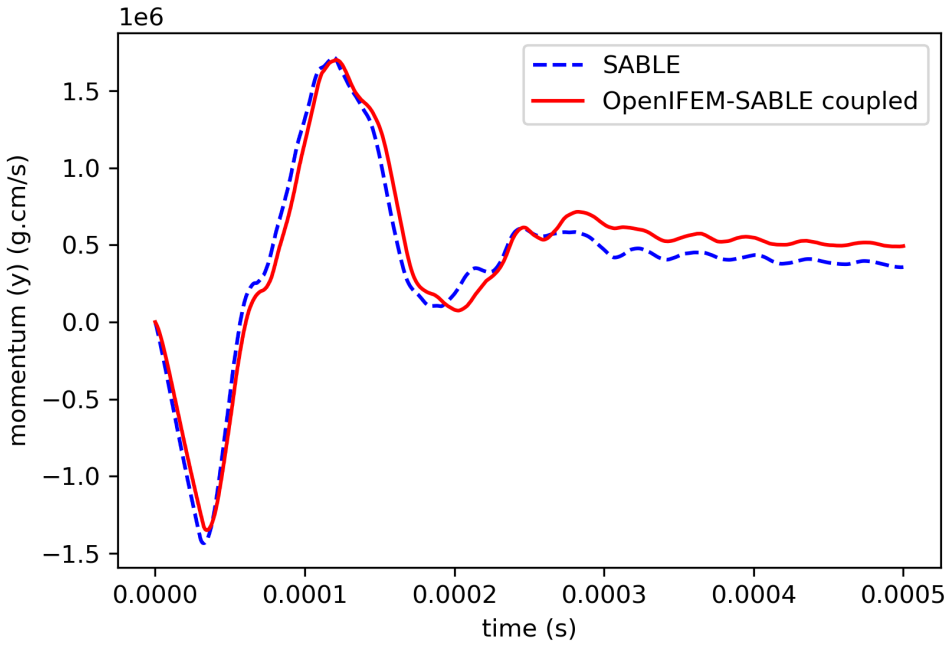

Figure 4-47 Target y-momentum time history for the Eulerian (- -) and coupled Eulerian-Lagrangian (–) calculations.

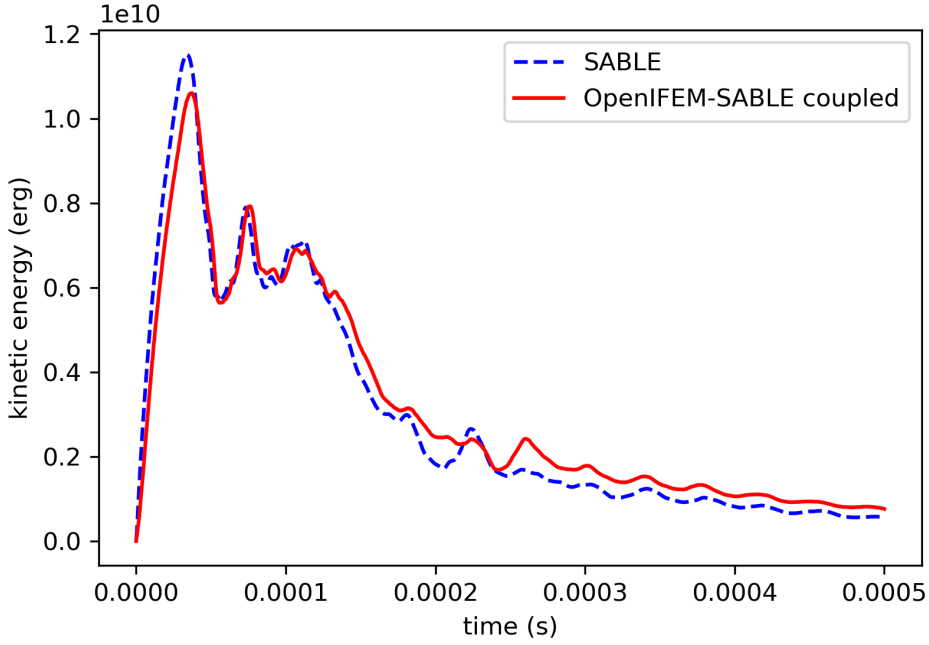

Figure 4-48 Target kinetic energy time history for the Eulerian (- -) and coupled Eulerian-Lagrangian (–) calculations.

(a)

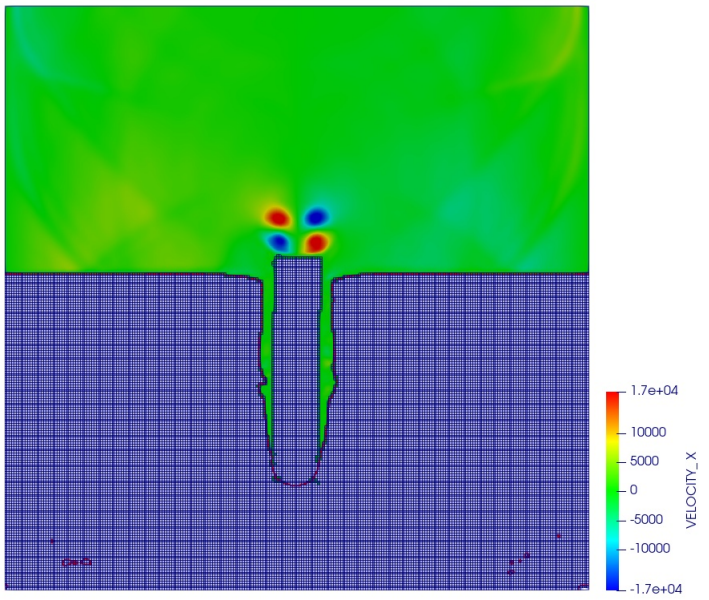

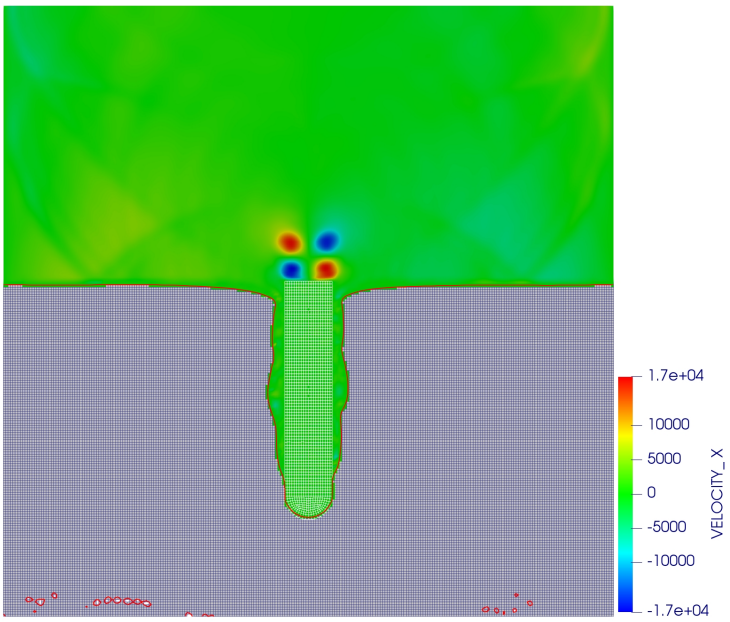

(b)

Figure 4-49 Air x-velocity at $t = 50\mu s$ for the Eulerian and coupled Eulerian-Lagrangian calculations.

(a)

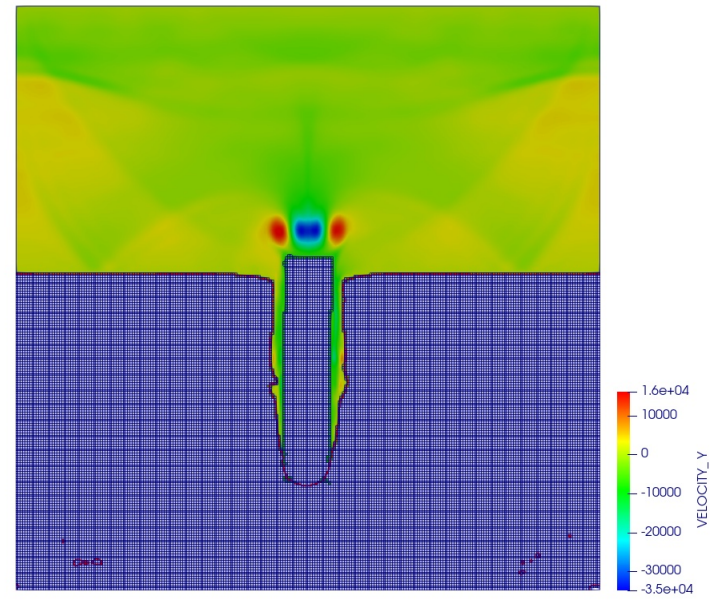

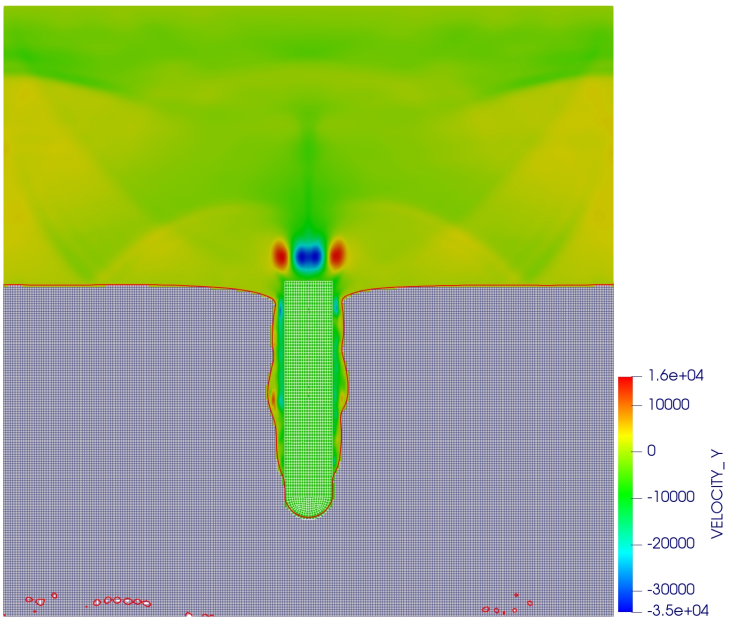

(b)

Figure 4-50 Air y-velocity at $t = 50\mu s$ for the Eulerian and coupled Eulerian-Lagrangian calculations.

4.3.3. Preliminary Penalty Assessment

This section presents a brief demonstration/assessment of the penalty enforcement of kinematic conditions for the coupled problem. The Lagrangian and Eulerian boundary overlap terms are exercised on the normal-impact hemispherical penetrator problem. The penalty scale factor is varied between 0.0 and 1.0 for each of the penalty terms in their respective momentum equations as shown in Table 4-4. The Eulerian domain uses a mesh size of 0.2 *cm* for the calculations presented below.

Group-1 (LP,EP)	Group-2 (LP,EP)	Group-3 (LP,EP)
(0.0,0.0)	(0.0,0.5)	(0.0,1.0)
(0.5,0.0)	(0.5,0.5)	(0.5,1.0)
(1.0,0.0)	(1.0,0.5)	(1.0,1.0)

Table 4-4 Matrix of Lagrangian (LP) and Eulerian (EP) penalty scale factors.

The group-1 results are presented in Figures 4-51 – 4-54. The best overall results appear to be for (LP,EP) = (0.5,0.0) with the tip position comparing very well with the Eulerian results in Figure 4-53.

Group-2 calculations hold EP=0.5 constant, with the Lagrangian penalty varying from 0.0 to 1.0. The results for group-2 are presented in Figures 4-55 – 4-58. In comparison to group-1, the effect of the Eulerian (boundary overlap) penalty terms is of second-order relative to the Lagrangian penalty. In comparison to group-1, the group-2 results are somewhat degraded with the tip position showing significant differences relative to the Eulerian calculation.

The group-3 results are presented in Figures 4-59 – 4-62. Here, the coupled calculations hold EP=1.0 constant. Similar to the group-2 results, EP=1.0 appears to do little to improve the calculations relative to the group-1 EP=0.0 results.

In general, using penalty scale factors greater than 0.5 appears to be a bit heavy-handed for the penetrator problem. The overall best results are obtained with (LP,EP) = (0.5,0.0) – particularly in terms of the penetrator tip position and kinetic energy. The Eulerian penalty terms provide second-order corrections on the penetrator problem, but may be important in other problems. Addition work is required to extend the penalty terms for problems with non-void background materials.

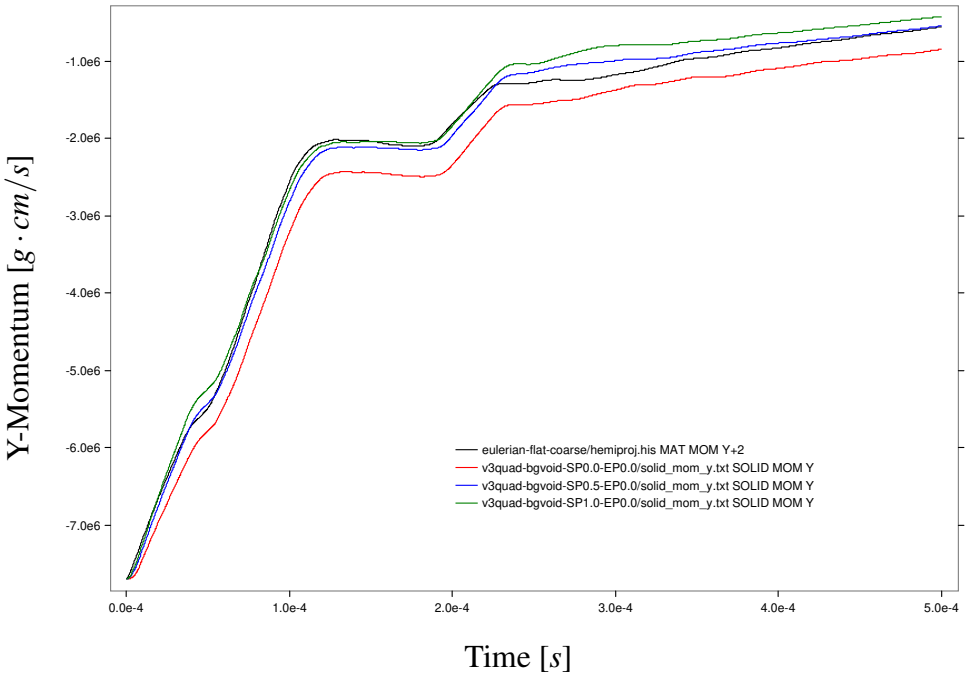

Figure 4-51 Penetrator y-momentum time history for the Eulerian (–) and coupled Eulerian-Lagrangian calculations with (LP,EP) = (0.0,0.0) (–), (LP,EP) = (0.5,0.0) (–), (LP,EP) = (1.0,0.0) (–).

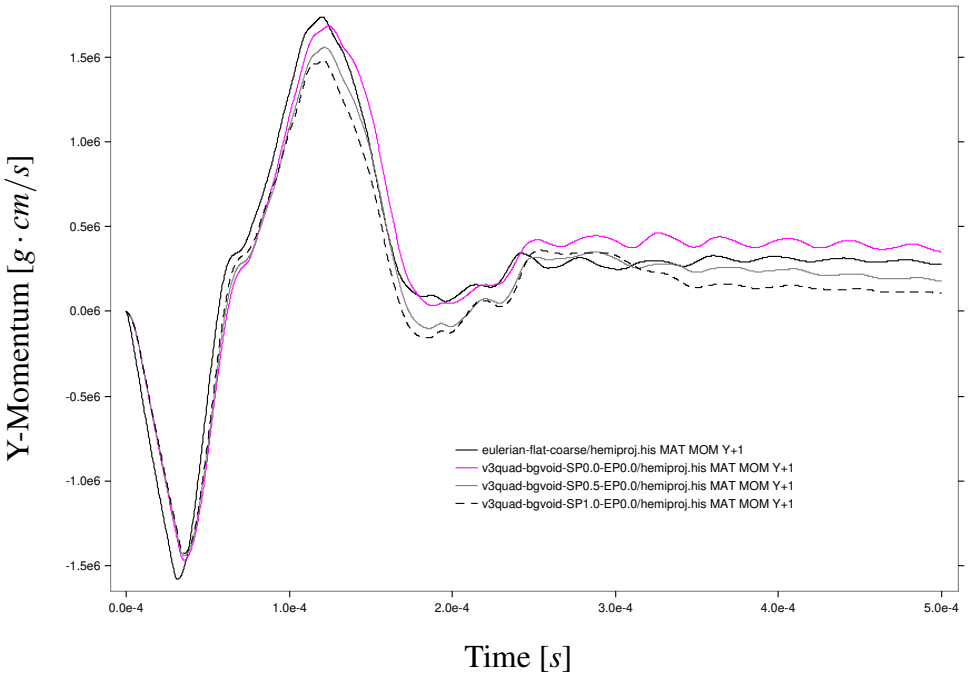

Figure 4-52 Target y-momentum time history for the Eulerian (–) and coupled Eulerian-Lagrangian calculations with (LP,EP) = (0.0,0.0) (–), (LP,EP) = (0.5,0.0) (–), (LP,EP) = (1.0,0.0) (- -).

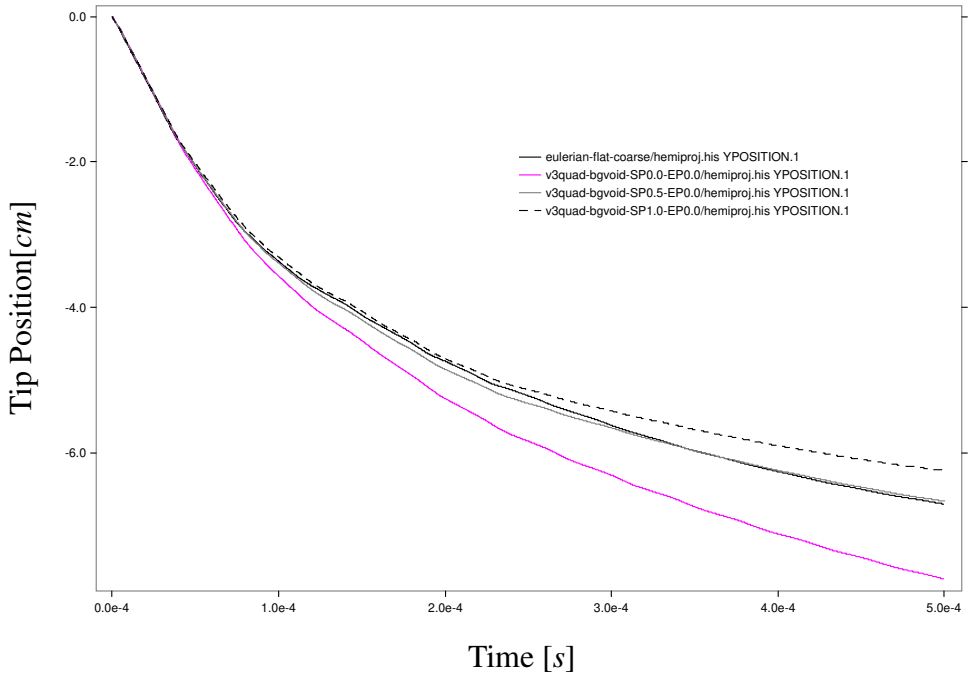

Figure 4-53 Penetrator tip position time history for the Eulerian (–) and coupled Eulerian-Lagrangian calculations with (LP,EP) = (0.0,0.0) (–), (LP,EP) = (0.5,0.0) (–), (LP,EP) = (1.0,0.0) (- -).

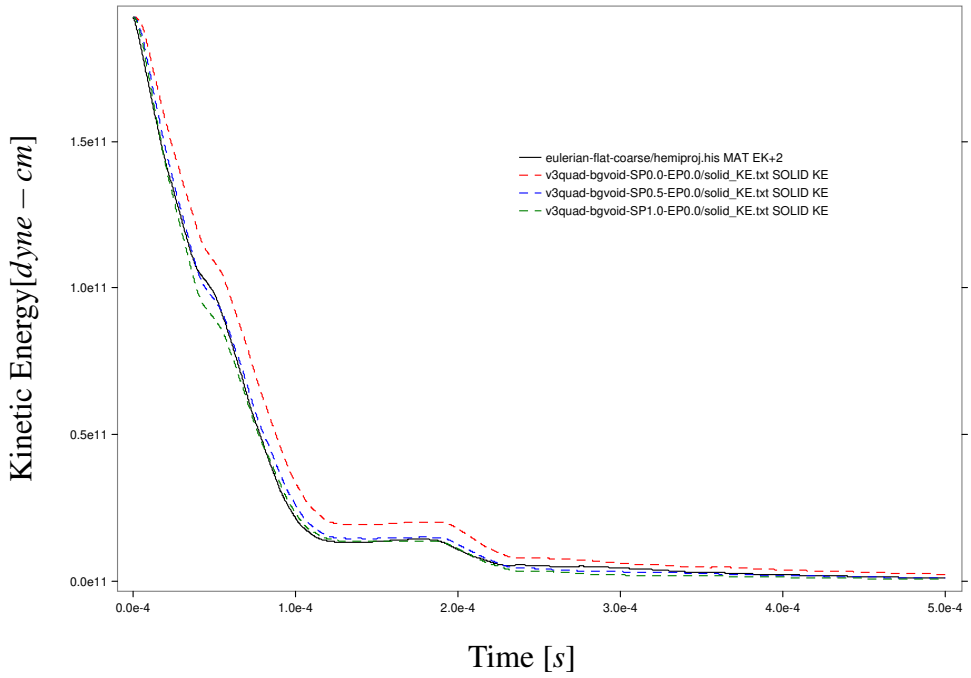

Figure 4-54 Penetrator kinetic energy time history for the Eulerian (–) and coupled Eulerian-Lagrangian calculations with (LP,EP) = (0.0,0.0) (- -), (LP,EP) = (0.5,0.0) (- -), (LP,EP) = (1.0,0.0) (- -).

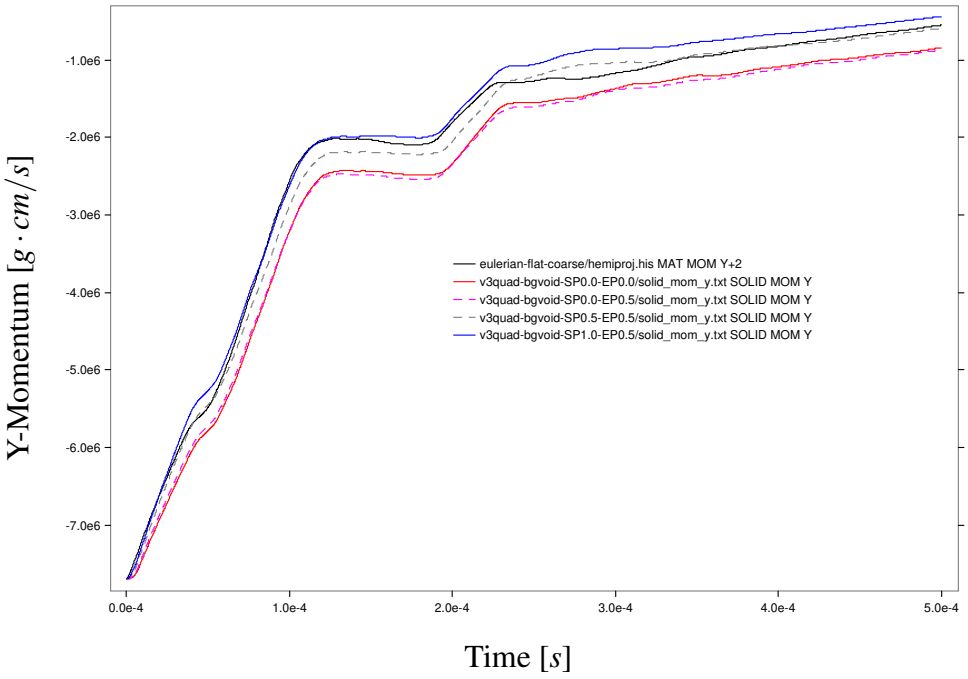

Figure 4-55 Penetrator y-momentum time history for the Eulerian (–) and coupled Eulerian-Lagrangian calculations with (LP,EP) = (0.0,0.0) (–), (LP,EP) = (0.0,0.5) (– –), (LP,EP) = (0.5,0.5) (- -), (LP,EP) = (1.0,0.5) (–).

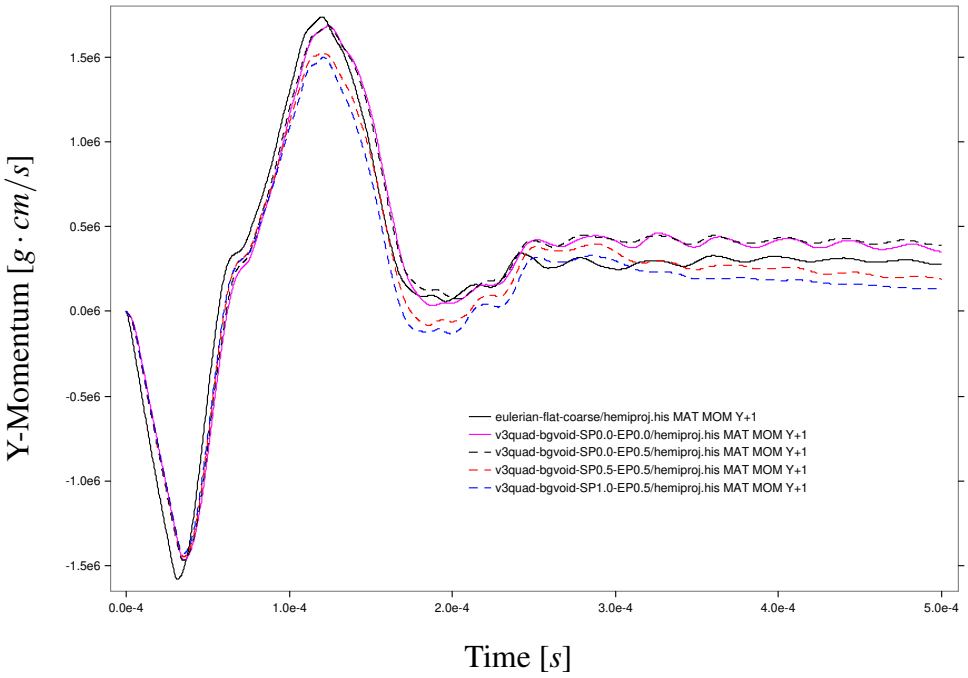

Figure 4-56 Target y-momentum time history for the Eulerian (–) and coupled Eulerian-Lagrangian calculations with (LP,EP) = (0.0,0.0) (–), (LP,EP) = (0.0,0.5) (- -), (LP,EP) = (0.5,0.5) (- -), (LP,EP) = (1.0,0.5) (- -).

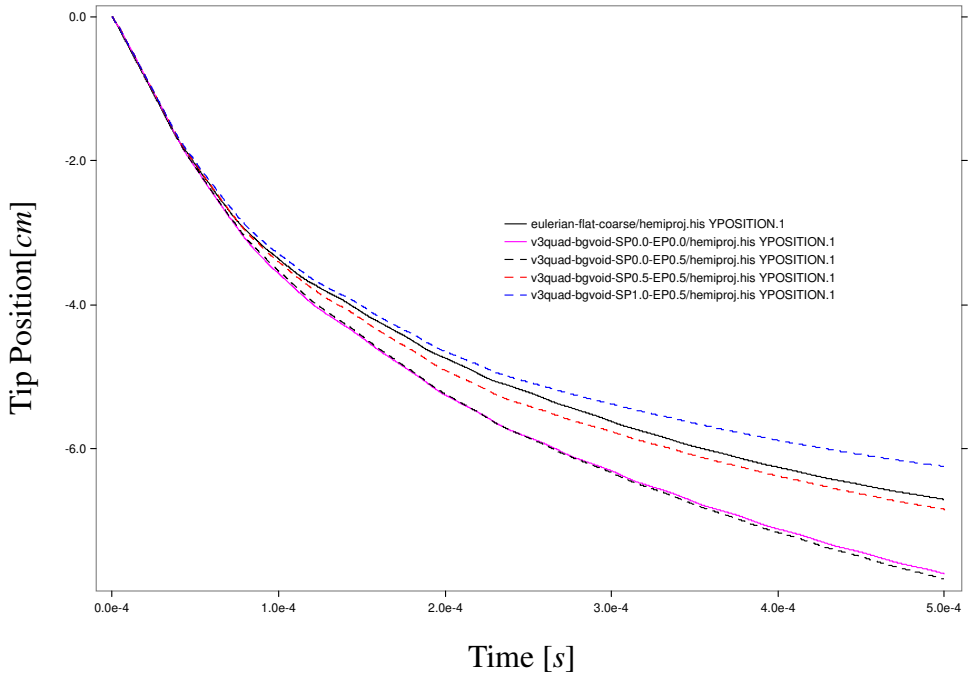

Figure 4-57 Penetrator tip position time history for the Eulerian (–) and coupled Eulerian-Lagrangian calculations with (LP,EP) = (0.0,0.0) (–), (LP,EP) = (0.0,0.5) (- -), (LP,EP) = (0.5,0.5) (- -), (LP,EP) = (1.0,0.5) (- -).

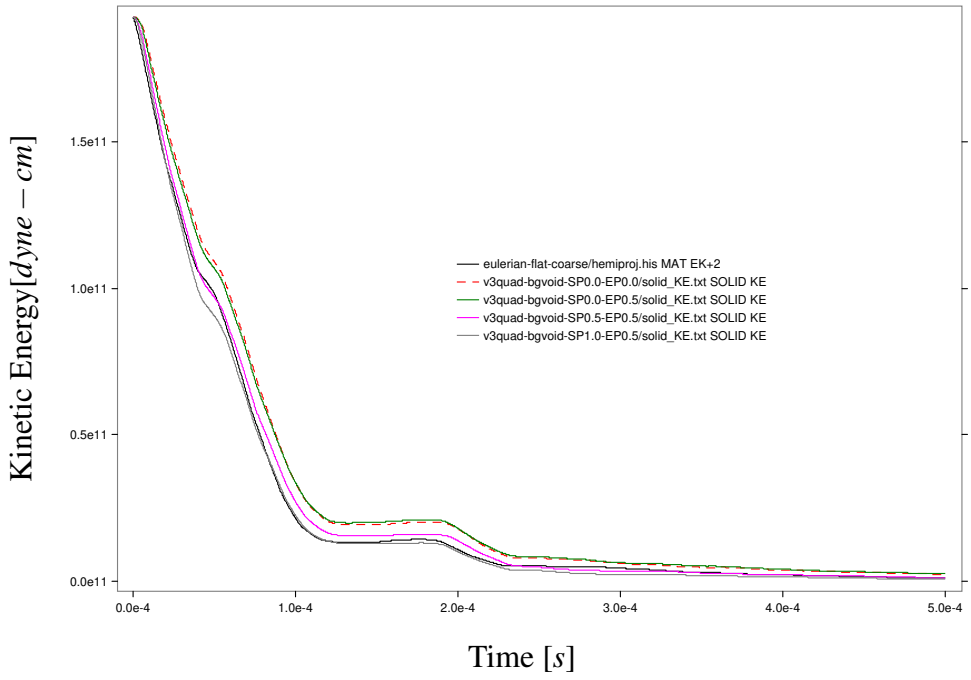

Figure 4-58 Penetrator kinetic energy time history for the Eulerian (–) and coupled Eulerian-Lagrangian calculations with (LP,EP) = (0.0,0.0) (- -), (LP,EP) = (0.0,0.5) (–), (LP,EP) = (0.5,0.5) (–), (LP,EP) = (1.0,0.5) (–).

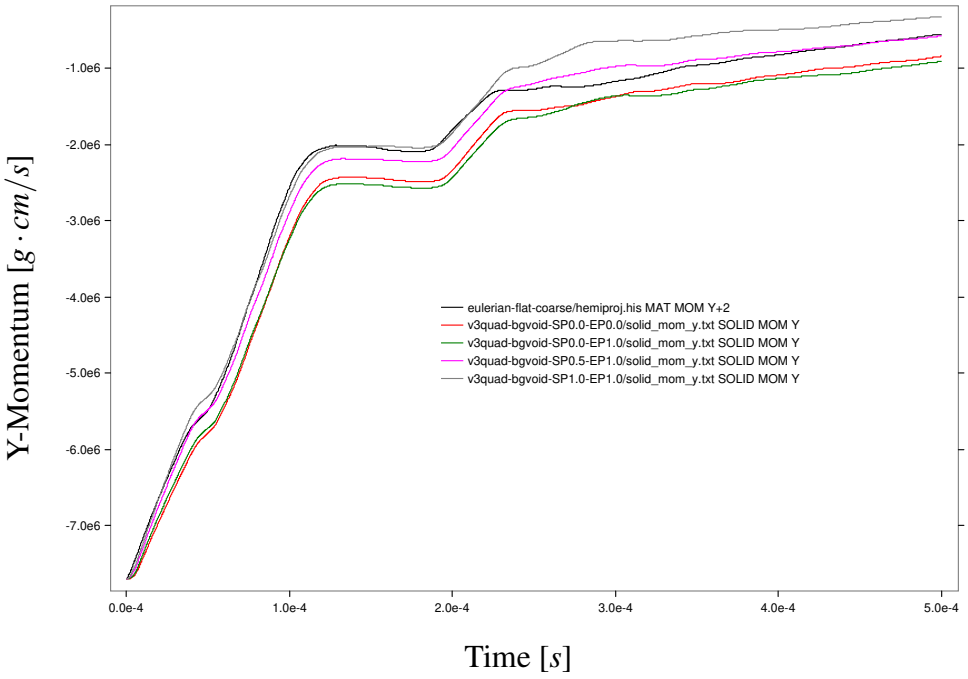

Figure 4-59 Penetrator y-momentum time history for the Eulerian (–) and coupled Eulerian-Lagrangian calculations with (LP,EP) = (0.0,0.0) (–), (LP,EP) = (0.0,1.0) (–), (LP,EP) = (0.5,1.0) (–), (LP,EP) = (1.0,1.0) (–).

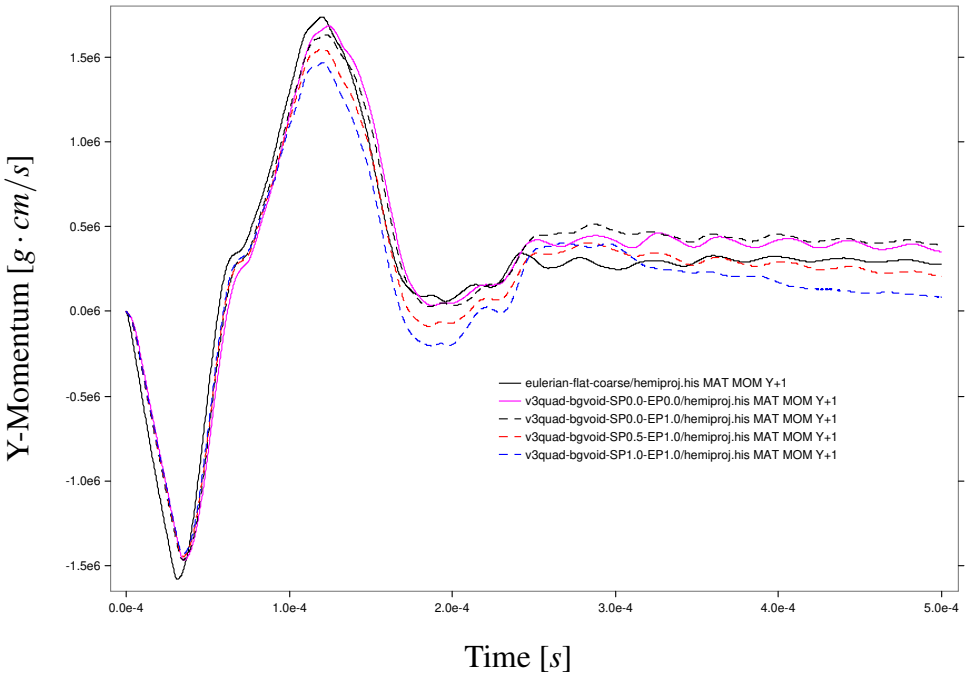

Figure 4-60 Target y-momentum time history for the Eulerian (–) and coupled Eulerian-Lagrangian calculations with (LP,EP) = (0.0,0.0) (–), (LP,EP) = (0.0,1.0) (- -), (LP,EP) = (0.5,1.0) (- -), (LP,EP) = (1.0,1.0) (- -).

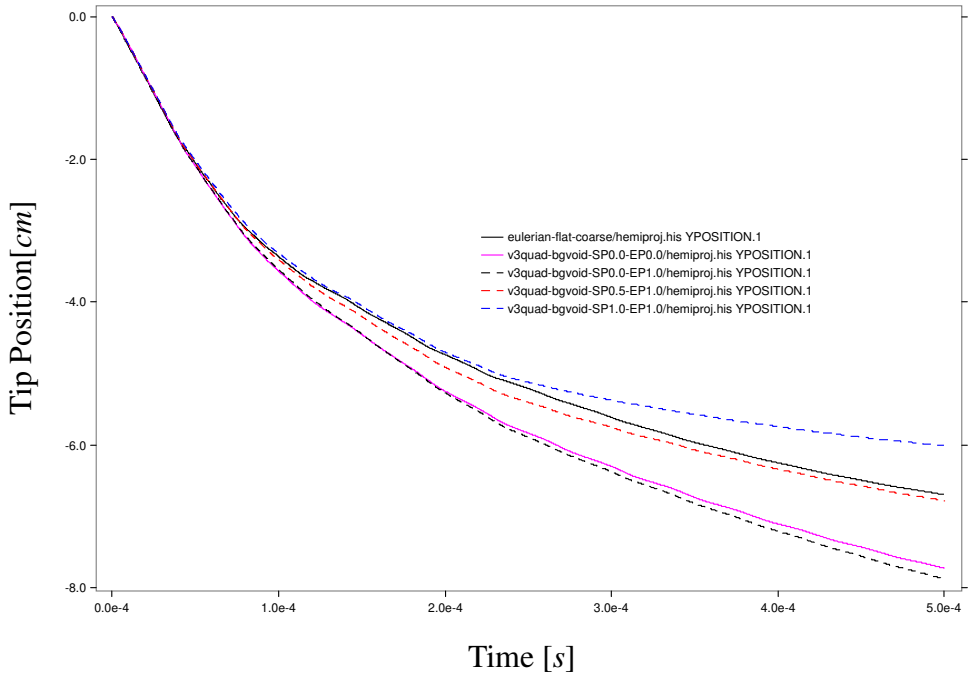

Figure 4-61 Penetrator tip position time history for the Eulerian (–) and coupled Eulerian-Lagrangian calculations with (LP,EP) = (0.0,0.0) (–), (LP,EP) = (0.0,1.0) (- -), (LP,EP) = (0.5,1.0) (- -), (LP,EP) = (1.0,1.0) (- -).

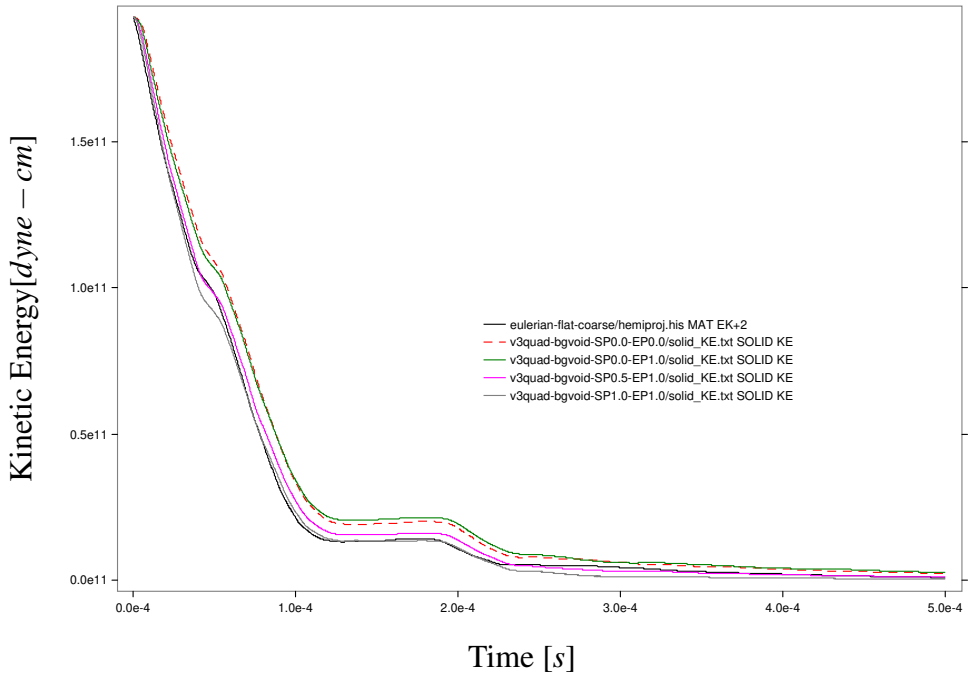

Figure 4-62 Penetrator kinetic energy time history for the Eulerian (–) and coupled Eulerian-Lagrangian calculations with (LP,EP) = (0.0,0.0) (- -), (LP,EP) = (0.0,1.0) (–), (LP,EP) = (0.5,1.0) (–), (LP,EP) = (1.0,1.0) (–).

4.4. Oblique Hemispherical Penetrator

The oblique impact hemispherical penetrator problem geometry is shown in Figure 4-63. The impact angle relative to the target surface is 25^o. The penetrator is 4340 steel with density $\rho = 7.8724\ g/cm^3$, Young's modulus $E = 2 \times 10^{12}\ dynes/cm^2$, and Poisson's ratio $\nu = 0.28$. The target material is a 23 MPa concrete with density $\rho = 2.040\ g/cm^3$, yield stress $Y = 4.189 \times 10^{10}\ dynes/cm^2$, Poisson's ratio $\nu = 0.345$, and a fracture pressure $P_{frac} = -2.0 \times 10^9\ dynes/cm^2$.

The overall Eulerian domain uses a mesh size of $0.1\ cm$, and spans a square domain $(-12.8, -12.8) \leq (x, y) \leq (12.8, 12.8)\ cm$. For the Eulerian calculation, the penetrator uses the "K and C" SESAME equation of state, and the target uses a KEOS Mie Gruüneisen EOS. The target yield model uses the "CTH GEO" model and associated void insertion model for fracture.

The target material has no-displacement conditions prescribed on the bottom and vertical sides and is initially at rest. The penetrator has an initial downward velocity $v_y = -50,000\ cm/s$. Force-coupling with a void background material is used with a total simulated time of $500\mu s$.

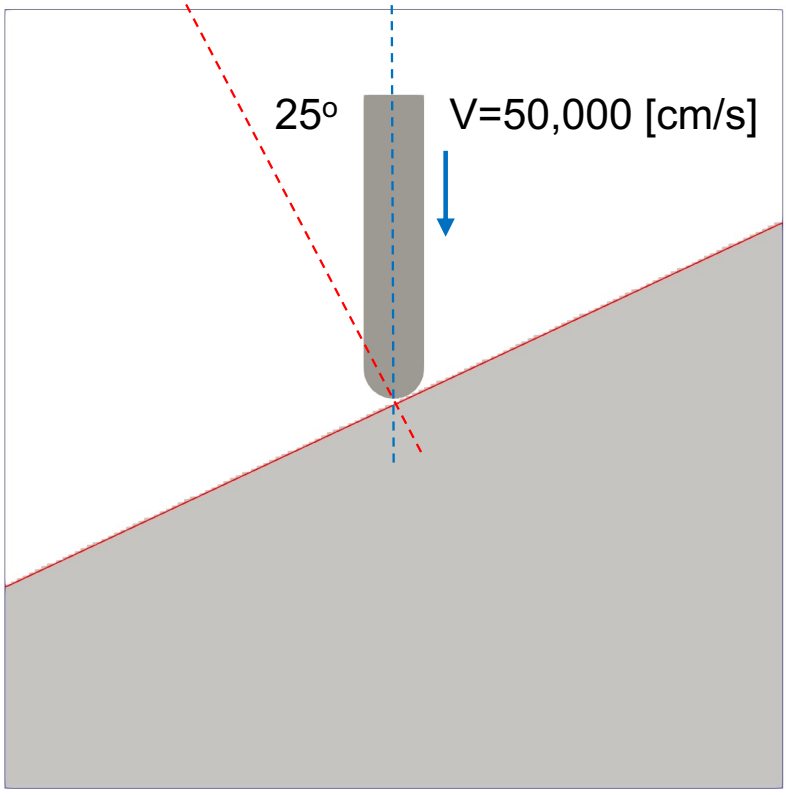

Figure 4-63 Oblique impact hemispherical penetrator and concrete target.

Figures 4-64 – 4-66 show the time-histories for the penetrator momentum and kinetic energy for the Eulerian and coupled simulations. The x-momentum time-history shows a large difference that corresponds to the amount of contact between the side of the penetrator and the target as

shown in Figure 4-70(a). The y-momentum time-history shows that the Lagrangian penetrator loses slightly less momentum, i.e., is moving faster over the course of the simulation. This correlates with the kinetic energy histories where the Lagrangian penetrator has slightly higher kinetic energy values over the course of the coupled simulation.

The concrete target time histories for momentum and kinetic energy are shown in Figures 4-67 – 4-43. The coupled calculation captures all of the primary features of the Eulerian momentum and kinetic energy histories. However, there is a somewhat noticeable time shift with the coupled results slightly lagging the Eulerian calculation. Although less pronounced in the velocity and kinetic energy histories, this effect is due to the fact that the coupling forces (stress and acceleration) require some small overlap between the Eulerian and Lagrangian meshes. This results in a slight delay in time for the penetrator and target to begin interacting.

Figure 4-71 shows the target material at $t = 50\ \mu s$ for the Eulerian and coupled calculations. Here, the way the tail/side of the penetrator interacts with the target material is quite different in the Eulerian and coupled calculations. The default Eulerian behavior for multiple materials in an element is that they are essentially stuck together, i.e, do not permit relative motion. In contrast, the coupled simulation applied traction forces from the target to the penetrator in the normal and tangential directions. This permits some degree of "slip" between the penetrator and target that the Eulerian calculation can not represent. This effects the final orientation of the penetrator, and the overall depth of penetration.

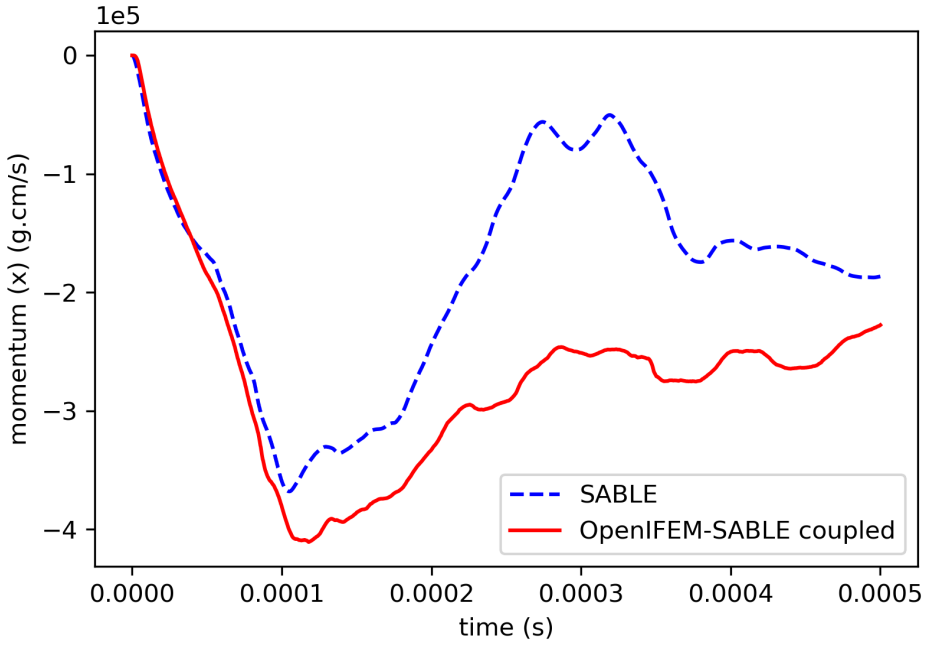

Figure 4-64 Penetrator x-momentum time history for the Eulerian (- -) and coupled Eulerian-Lagrangian (–) calculations.

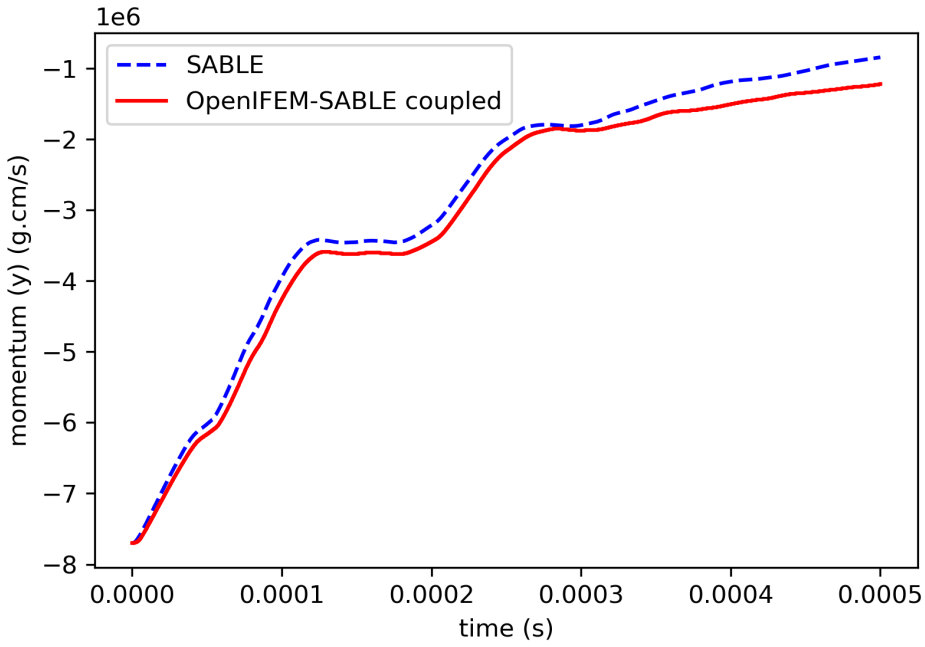

Figure 4-65 Penetrator y-momentum time history for the Eulerian (- -) and coupled Eulerian-Lagrangian (–) calculations.

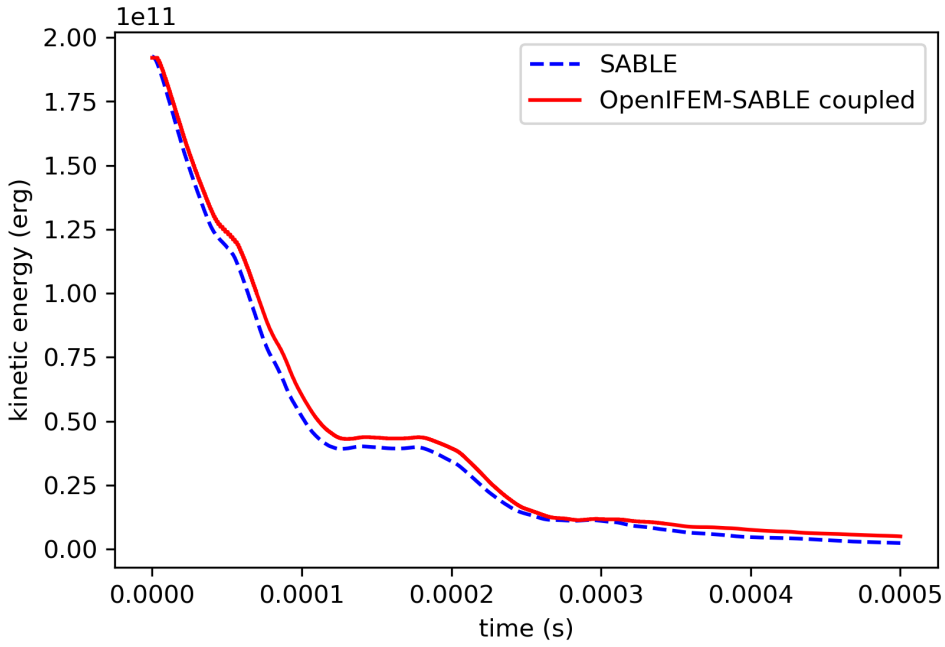

Figure 4-66 Penetrator kinetic energy time history for the Eulerian (- -) and coupled Eulerian-Lagrangian (–) calculations.

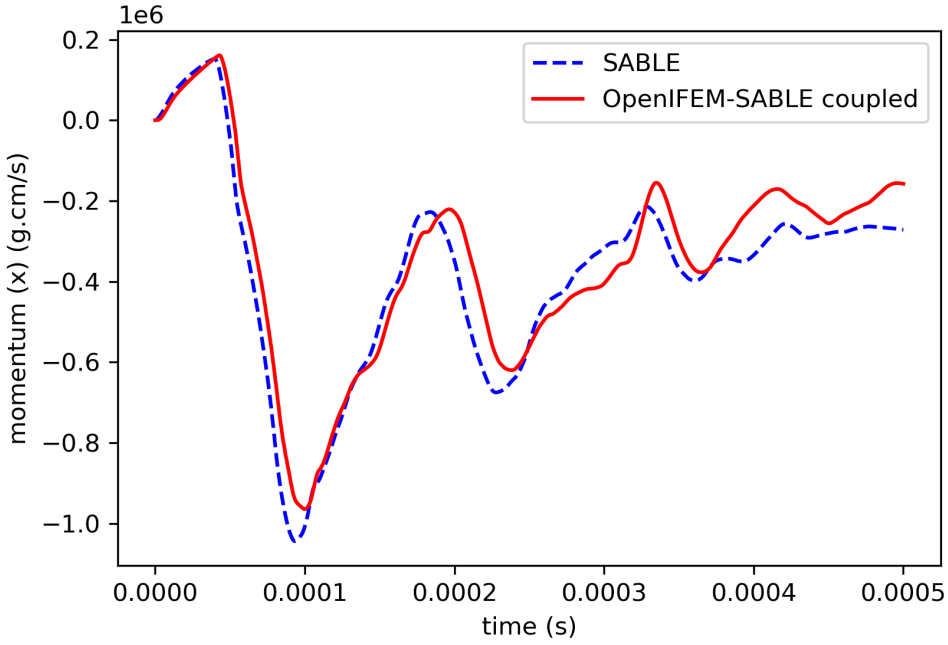

Figure 4-67 Target x-momentum time history for the Eulerian (- -) and coupled Eulerian-Lagrangian (–) calculations.

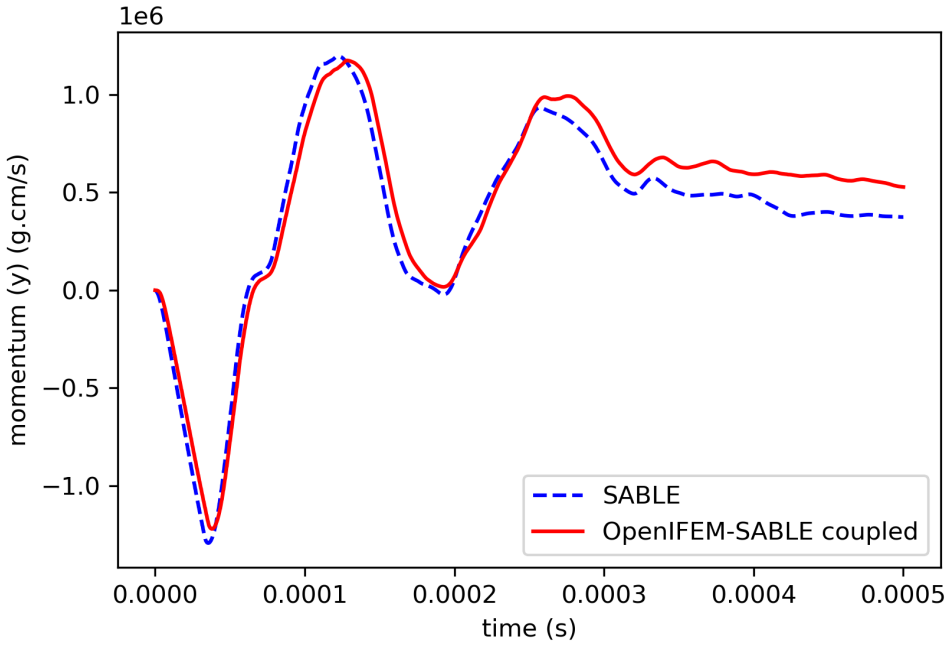

Figure 4-68 Target y-momentum time history for the Eulerian (- -) and coupled Eulerian-Lagrangian (–) calculations.

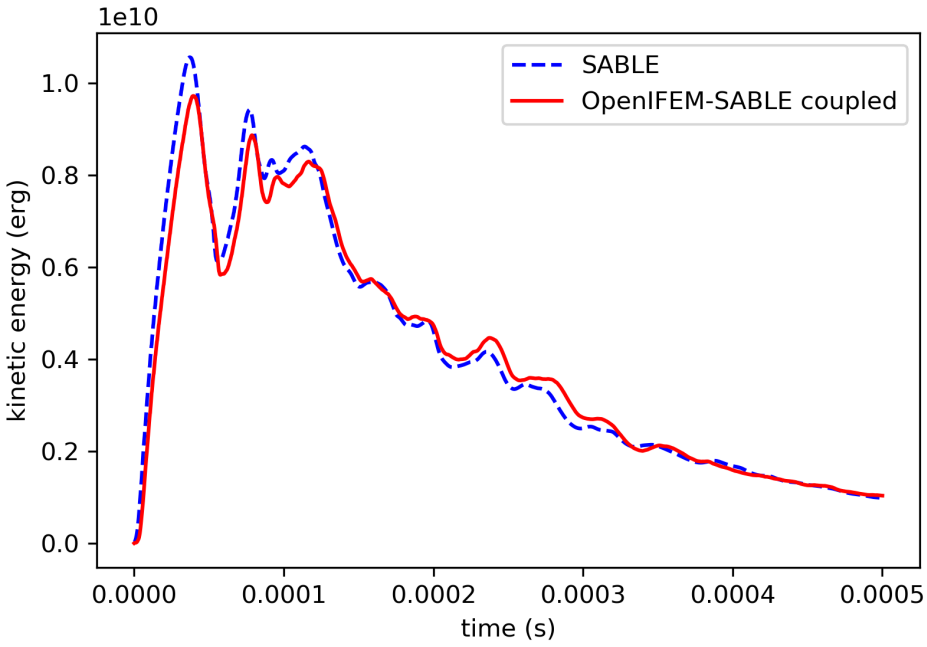

Figure 4-69 Target kinetic energy time history for the Eulerian (- -) and coupled Eulerian-Lagrangian (–) calculations.

(a)

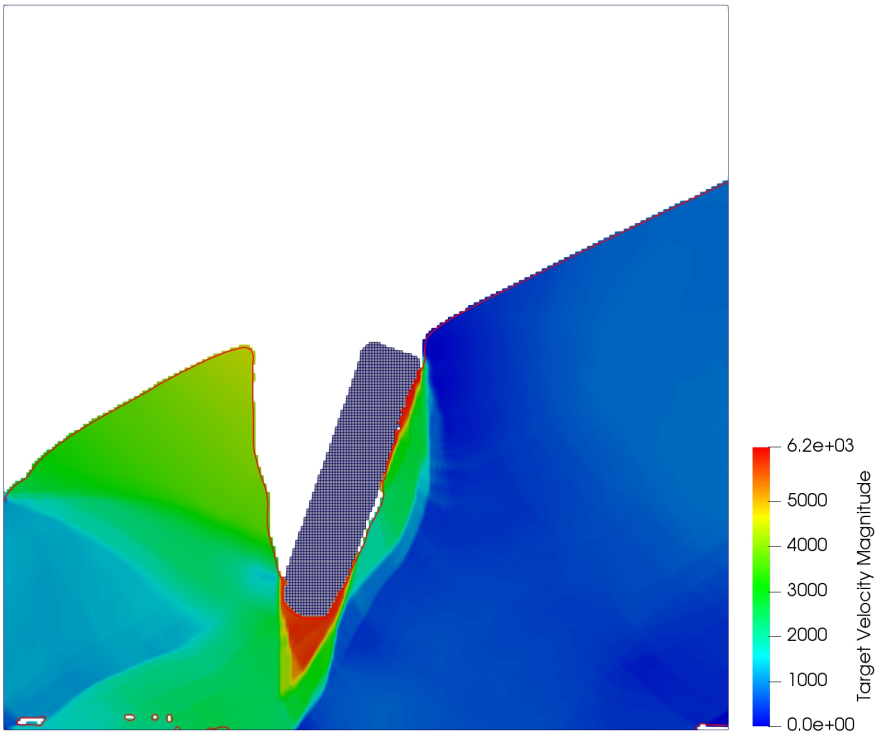

(b)

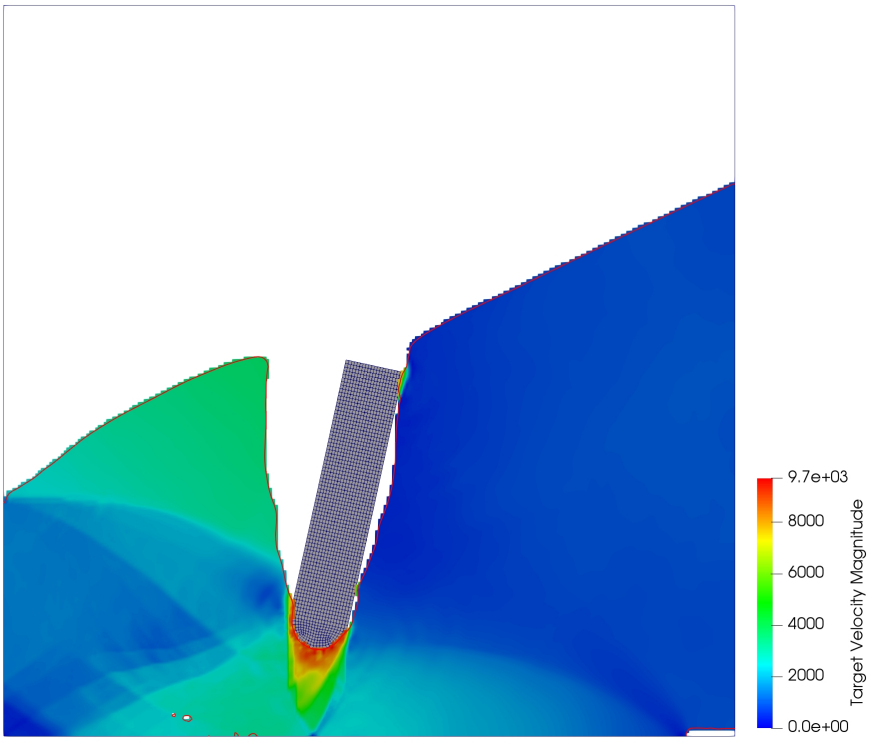

Figure 4-70 Final configuration for (a) the Eulerian simulation and (b) the coupled (OPENIFEM – SABLE) simulation.

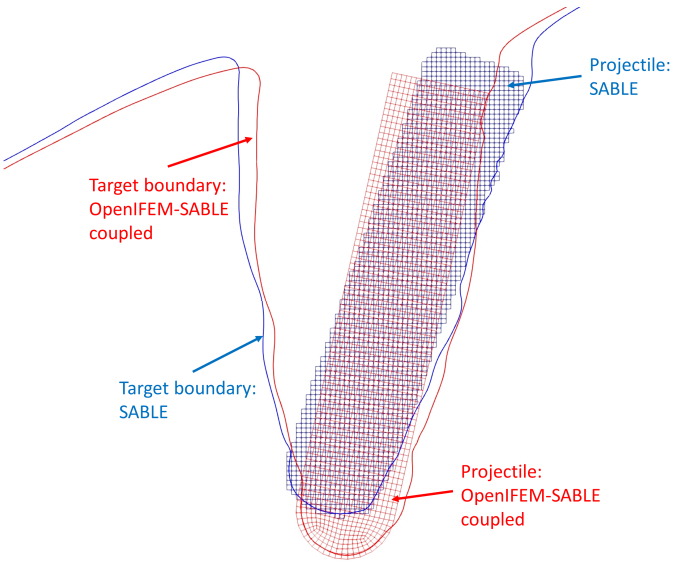

(a)

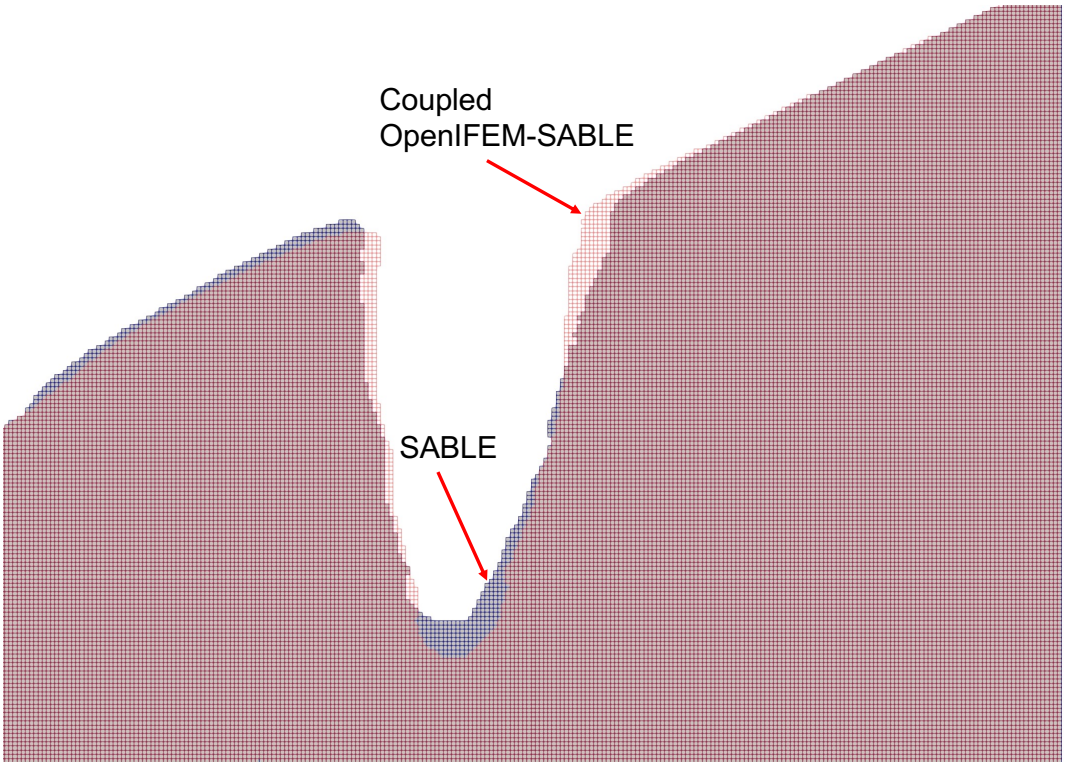

(b)

Figure 4-71 Comparison of the (a) the final projectile position and target material interface for the Eulerian (–) and coupled (–) simulations, and (b) the target material location for the Eulerian (blue) and coupled (red) simulations.

4.5. Programmed Burn Loading on a Ball

This problem considers behavior of a plexiglass ball under the pressure loading due to programmed burn of a high-explosive. The geometry is shown in Figure 4-72. The Eulerian domain is 20 cm square with the lower-left corner at $(x,y) = (-5.0, 0.0)$ cm. The ball is located at $(x,y) = (4.5, 12.5)$ cm has a 2.5 cm radius, and the high-explosive (HE) spans $(2.5, 4.0) \leq (x,y) \leq (7.5, 10.0)$ cm. An Eulerian mesh resolution of 0.1 cm is used for all calculations.

The exterior boundaries of the Eulerian domain use "do-nothing" boundary conditions emulating a passive outflow condition with $P = 0$. The low-pressure air surrounding the ball and HE is initially at rest with a pressure $P = 10^{-5}$ $dynes/cm^2$. A single detonation point is used for the HE.

The coupled simulations are carried out using (a) low-pressure air and (b) a matched material for the overlap region between the Lagrangian ball and the Eulerian mesh.

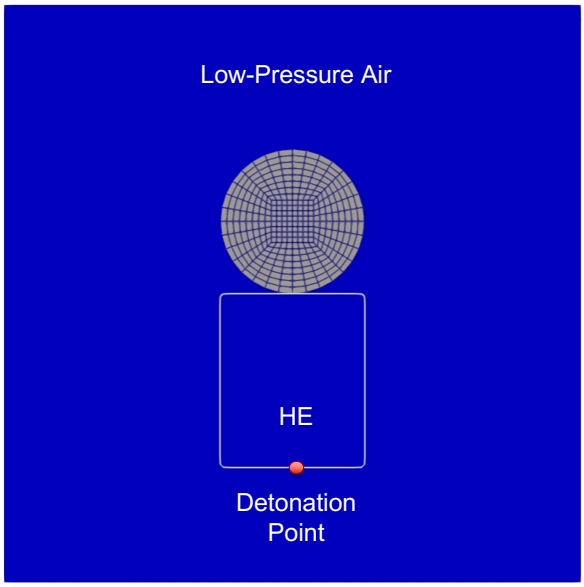

Figure 4-72 Programmed burn loading on a ball geometry.

4.5.1. Force-Coupling, Low-Pressure Air Background

Snapshots of the Eulerian and coupled simulations using low-pressure air in the overlap Lagrangian–Eulerian overlap region are shown in Figures 4-73 and 4-74 at $t = 2.1 \times 10^{-5}$ and $t = 3.1 \times 10^{-5}$ s respectively. The isolines show the 50% volume fraction of the high-explosive material. There is a reasonable, albeit qualitative, correlation between the Eulerian and coupled simulations. However, in the coupled calculations, the approximate location of the interface is clearly inside the Lagrangian body. This misalignment of the interface is due, in part, to the remap procedure in the Eulerian solve – see §3.14. Additional testing has indicated that the

interface mismatch is driven, in-part, by the high pressure gradients at the interface between the reacted HE and the low-pressure air in the overlap region between the Lagrangian ball and the Eulerian mesh. The low-pressure air responds with relatively large velocities under the ball, and the residual forces do not completely compensate for this effect. The ultimate result is a relatively high-pressure "bubble" that translates with the Lagrangian ball. The consequences of this behavior are presented in the ensuing discussion.

Time history plots of the ball y-momentum and kinetic energy are shown in Figures 4-75 and 4-76. Figure 4-75 shows that the ball in the Eulerian calculation achieves essentially rigid-body motion where it is translating vertically with essentially a constant y-momentum until it starts to leave the computational domain. In contrast, the coupled simulation undergoes a continuous acceleration during the same time period. This correlates with the divergence in the kinetic energy time-histories shown in Figure 4-76.

The time history plots of the ball center position and velocity are shown in Figure 4-77 and 4-78. Similar to the y-momentum, the y-position diverge after $t \approx 1.5 \times 10^{-4}$ s. The peak amplitude of the y-velocity also diverges after this point in time. The acceleration of the ball in the coupled simulation may be explained, in part, by the high-pressure region in the Eulerian simulation that is effectively "frozen-in" relative to the Lagrangian ball. This effect is shown in Figure 4-79. The consequence of the high pressure halo at the edge of the Lagrangian ball is an artificial pressure load on the ball that is relatively constant in time and continues to accelerate the Lagrangian ball. Additional work is required to understand and resolve these differences.

Figure 4-80 shows snapshots of the velocity field relative to the ball for (a) the Eulerian and (b) the coupled simulations. Another consequence of the "frozen-in" high-pressure region is the development of spurious velocities behind the ball which is moving vertically. The velocities develop because the moving high-pressure region effectively acts like a moving shock front, albeit moving with the ball.

(a)

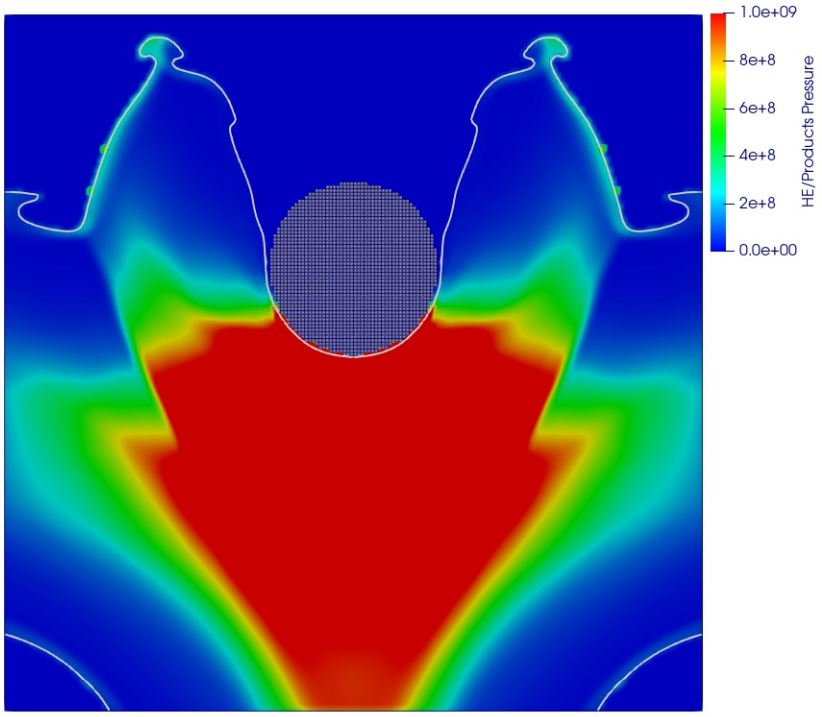

(b)

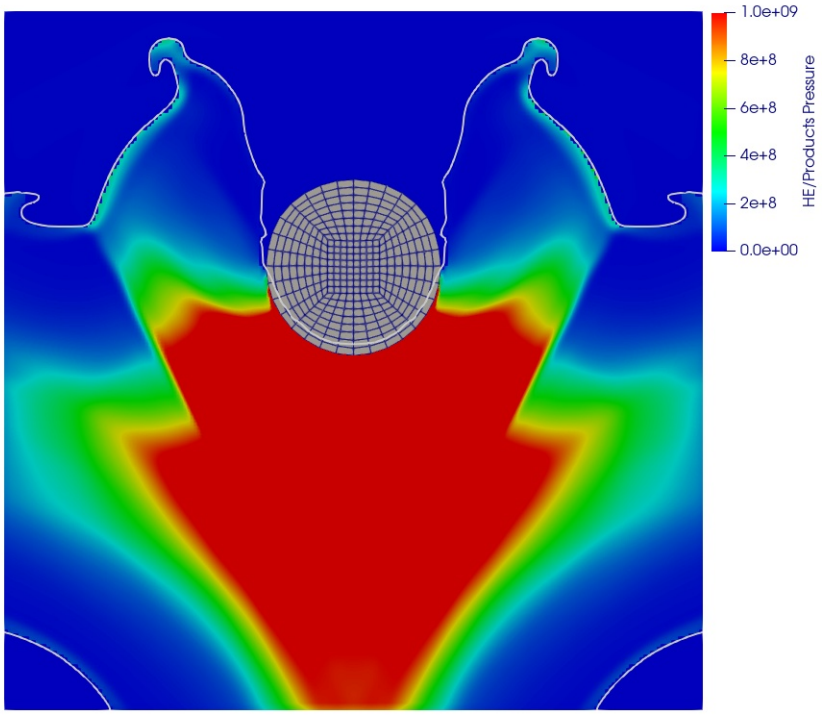

Figure 4-73 Snapshots of the gas pressure and ball location at $t = 2.1 \times 10^{-5} s$ for (a) the Eulerian simulation, and (b) the coupled simulation.

(a)

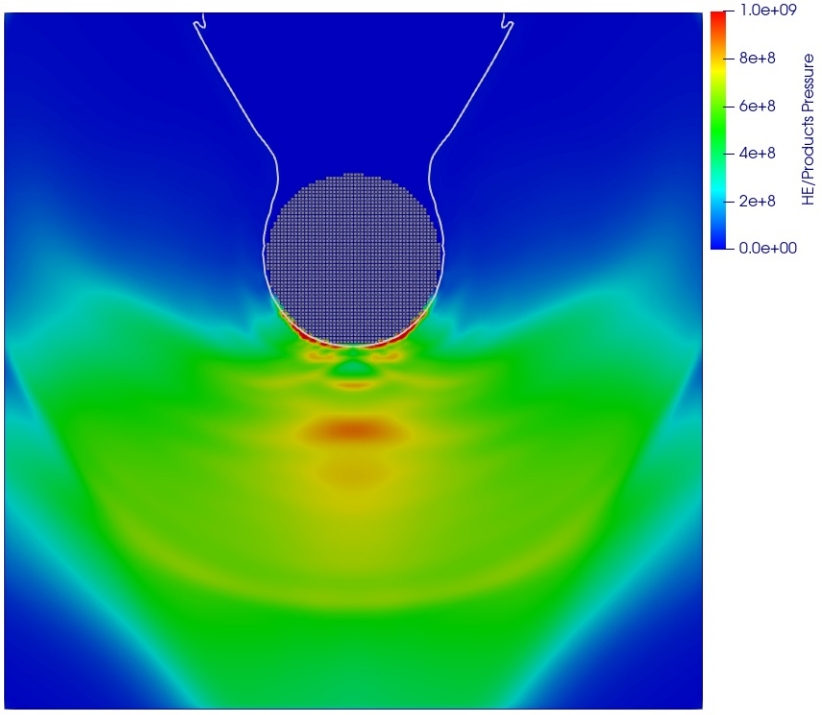

(b)

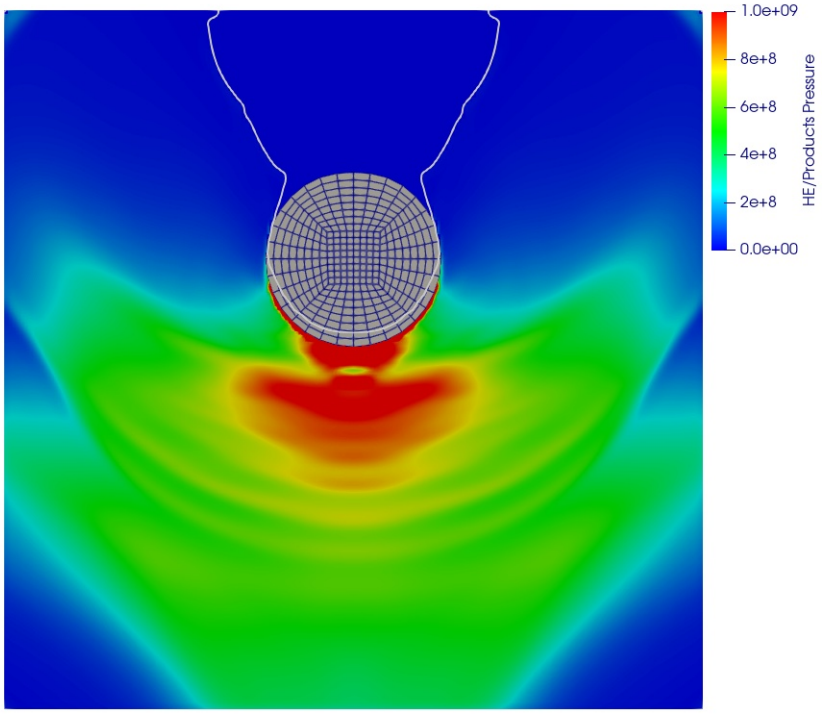

Figure 4-74 Snapshots of the gas pressure and ball location at $t = 3.1 \times 10^{-5} s$ for (a) the Eulerian simulation, and (b) the coupled simulation.

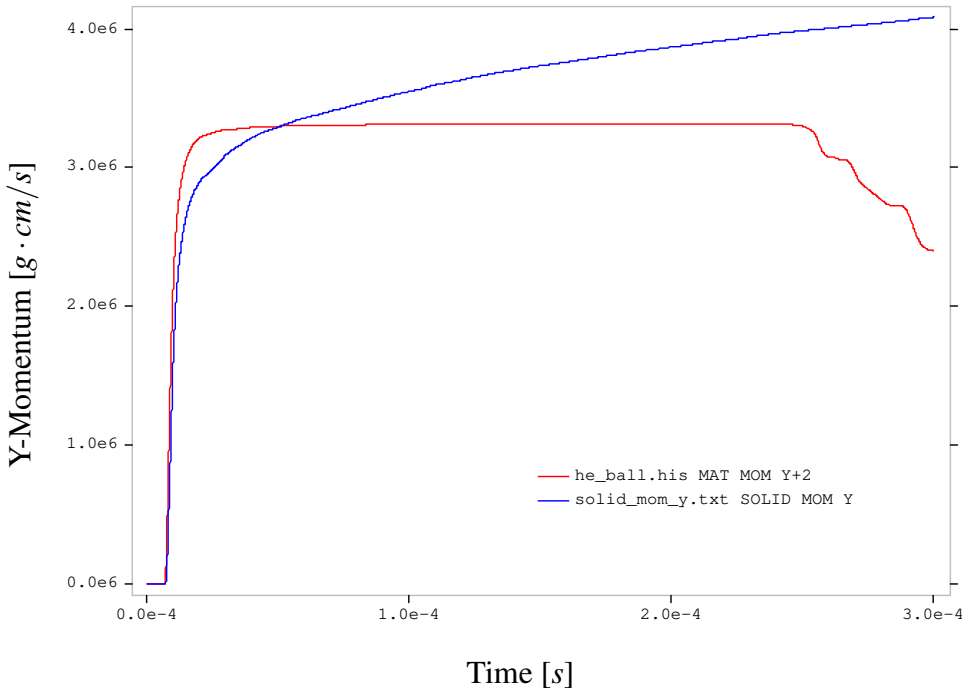

Figure 4-75 Ball y-momentum time history for the Eulerian (–) and Lagrangian (–) calculations.

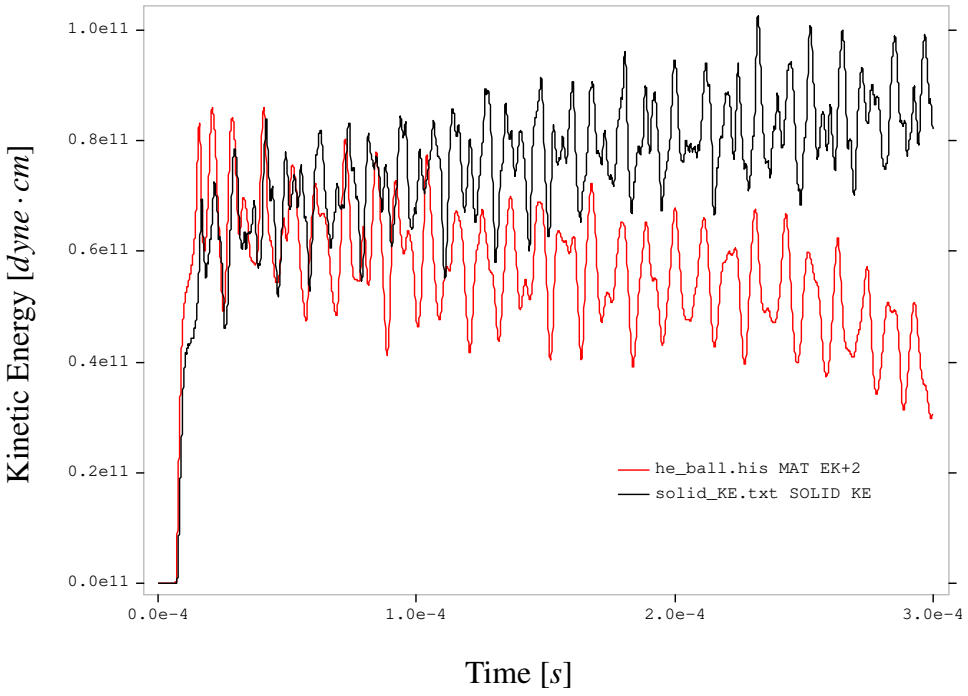

Figure 4-76 Ball kinetic energy time history for the Eulerian (–) and Lagrangian (–) calculations.

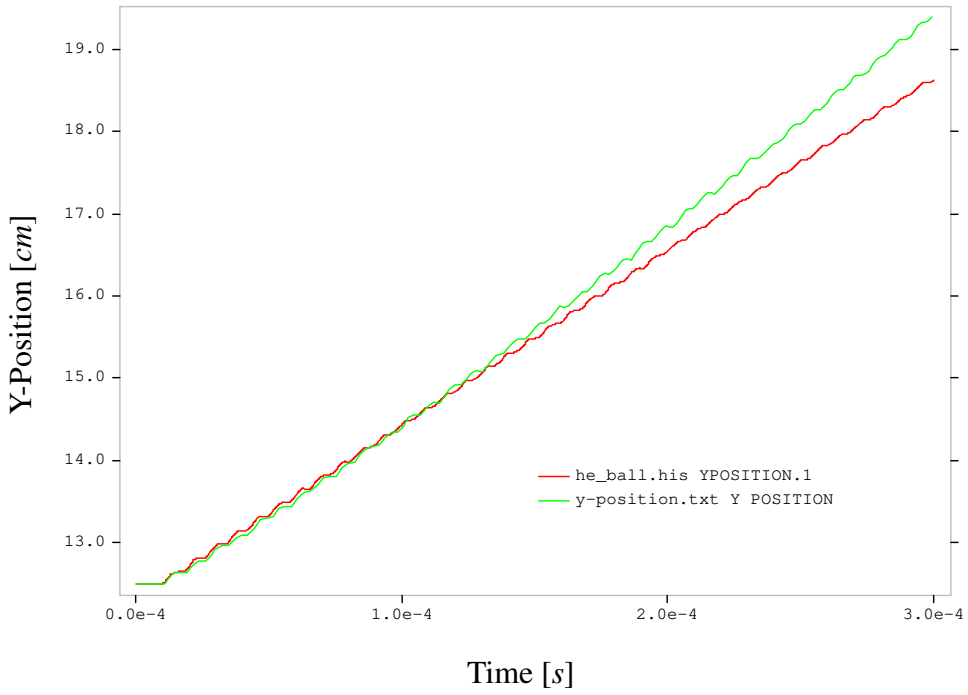

Figure 4-77 Ball y-position time history for the Eulerian (–) and Lagrangian (–) calculations.

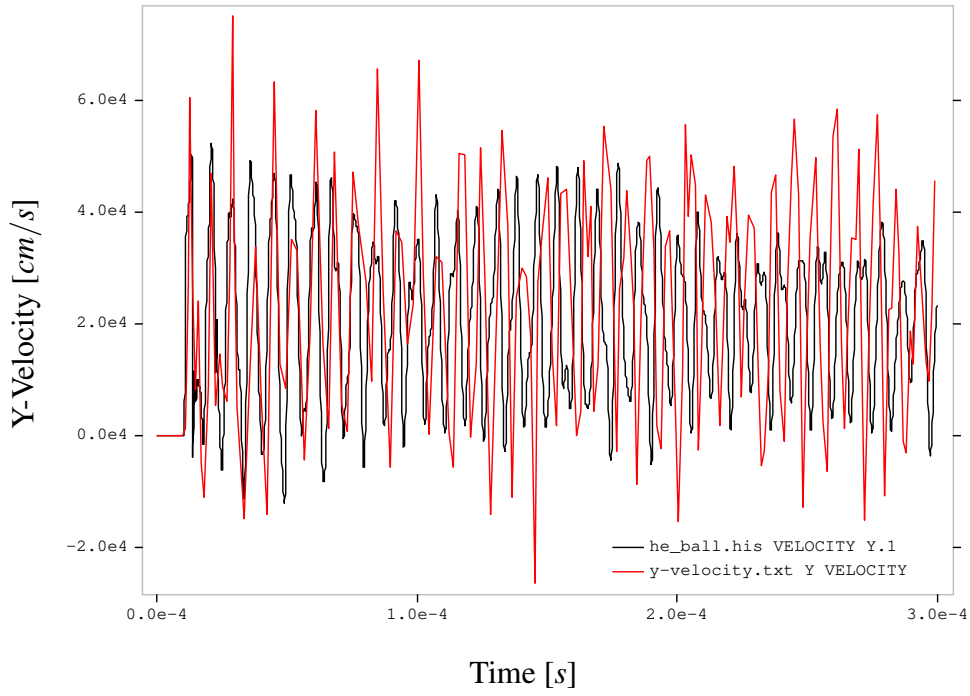

Figure 4-78 Ball y-velocity time history for the Eulerian (–) and Lagrangian (–) calculations.

(a)

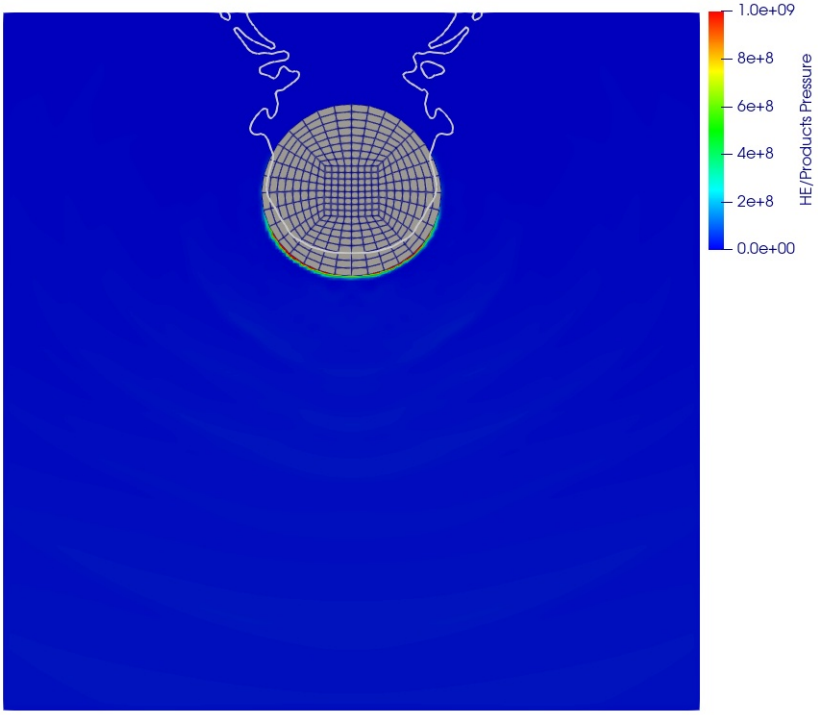

(b)

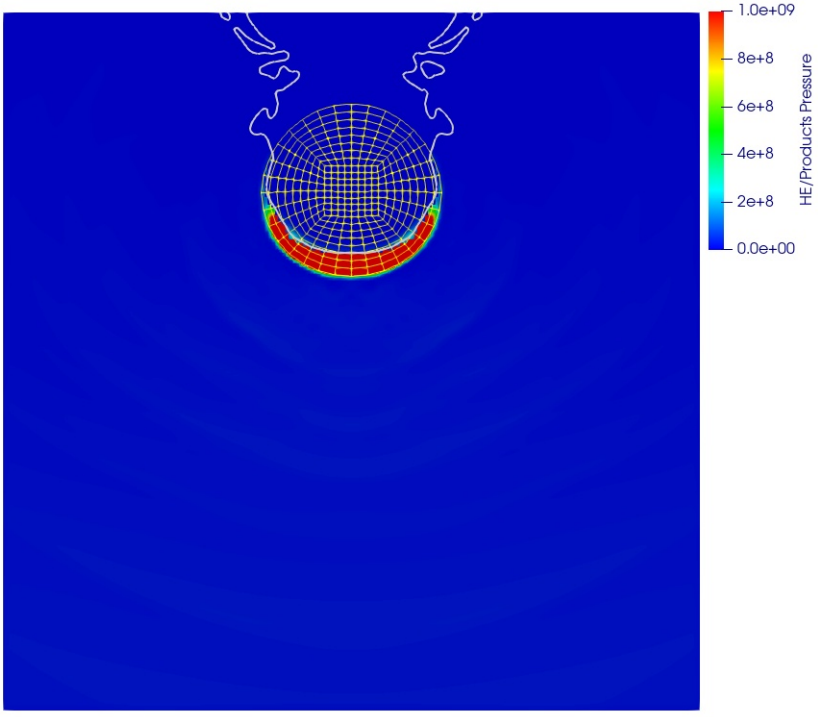

Figure 4-79 Snapshots of the HE pressure and ball location showing (a) the residual pressure halo below the Lagrangian ball, and (b) the high pressure region behind the Lagrangian ball.

(a)

(b)

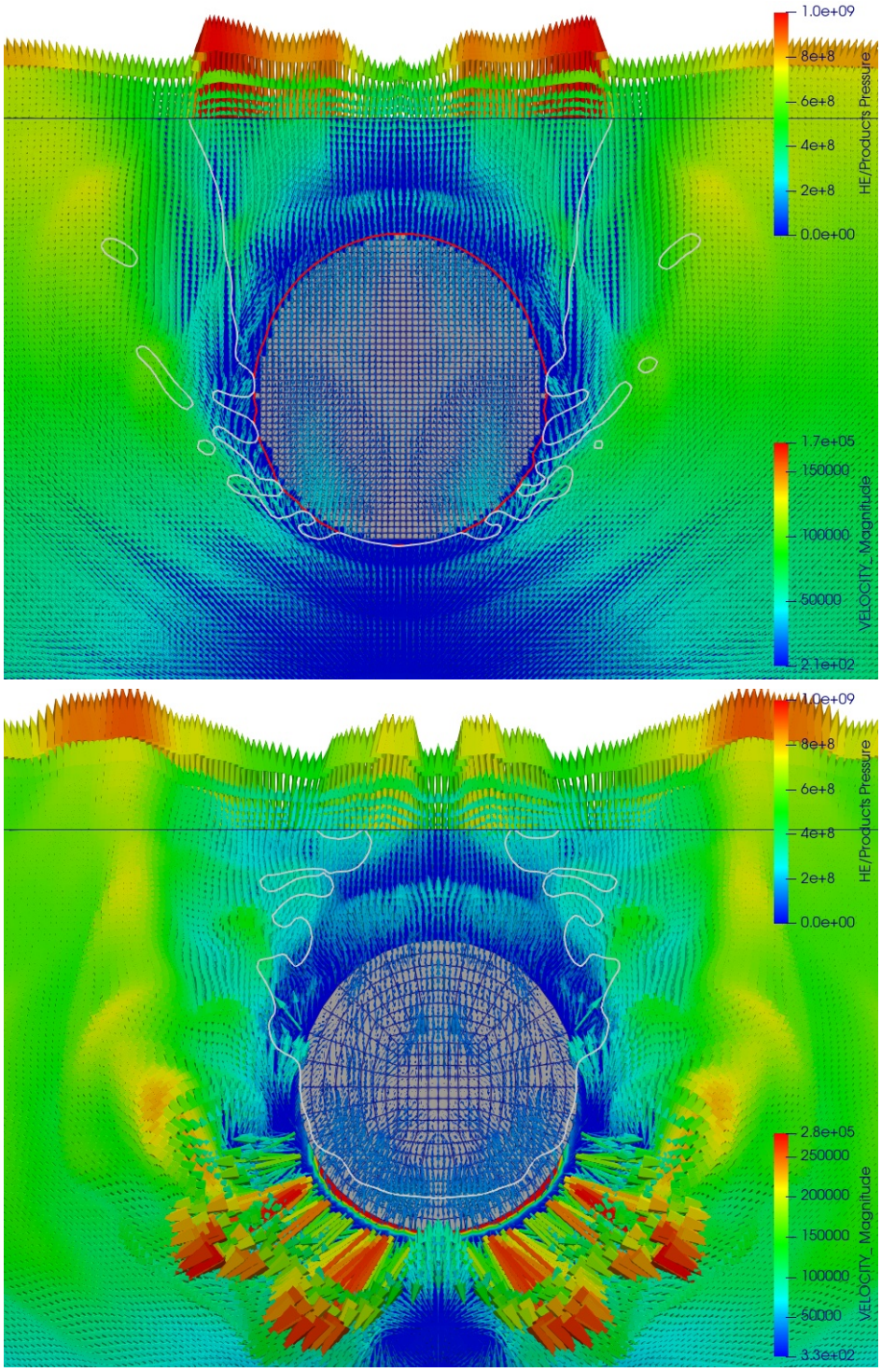

Figure 4-80 Snapshots of the velocity field and ball location for (a) the Eulerian calculation, and (b) the coupled simulation.

4.5.2. Force-Coupling, Matched Background Material

This version of the high-explosive – ball problem uses a material matched to the Lagrangian ball in the region of overlap in the Eulerian mesh. Snapshots of the Eulerian and coupled simulations are shown in Figures 4-81 and 4-82 at $t = 2.1 \times 10^{-5}$ and $t = 3.1 \times 10^{-5}$ s respectively. The isolines show the 50% volume fraction of the high-explosive material. In contrast to the snapshot of the coupled simulation using low-pressure air in 4-74, the interface location using a matched background material is aligned with the boundary of the Lagrangian ball. In addition, the use of a matched background material eliminates the high-pressure "bubble" and the associated pressure halo.

Time history plots of the ball y-momentum and kinetic energy are shown in Figures 4-83 and 4-84. Figure 4-83 shows that the ball in the Eulerian calculation achieves essentially rigid-body motion where it is translating vertically with essentially a constant y-momentum until it starts to leave the computational domain. This is seen at about 2.5×10^{-4} s in the Eulerian calculation because ball is being convected out of the Eulerian domain. In contrast, the Lagrangian ball continues to experience rigid-body motion despite having a partial overlap with the Eulerian mesh. The is a remarkably good correlation of the kinetic energy time-histories in Figure 4-84. The time history plots of the ball center position and velocity are shown in Figure 4-85 and 4-86. The y-position of the ball in the coupled calculations lags the Eulerian calculation by approximately 3% at $t = 3.0 \times 10^{-4}$ s

Figure 4-87 shows snapshots of the velocity field relative to the ball for (a) the Eulerian and (b) the coupled simulations. The general features of the velocity field are similar. However, the coupled simulation produces a peak velocity magnitude that is 23% higher than the Eulerian calculation. In addition, there are potential-flow artifacts near the trailing edge of the ball. Using the matched background material in the Eulerian mesh, removes the "frozen-in" high-pressure region and the associated spurious velocities. The use of adaptive mesh refinement may improve the quality of the results, but this remains a topic for future work.

(a)

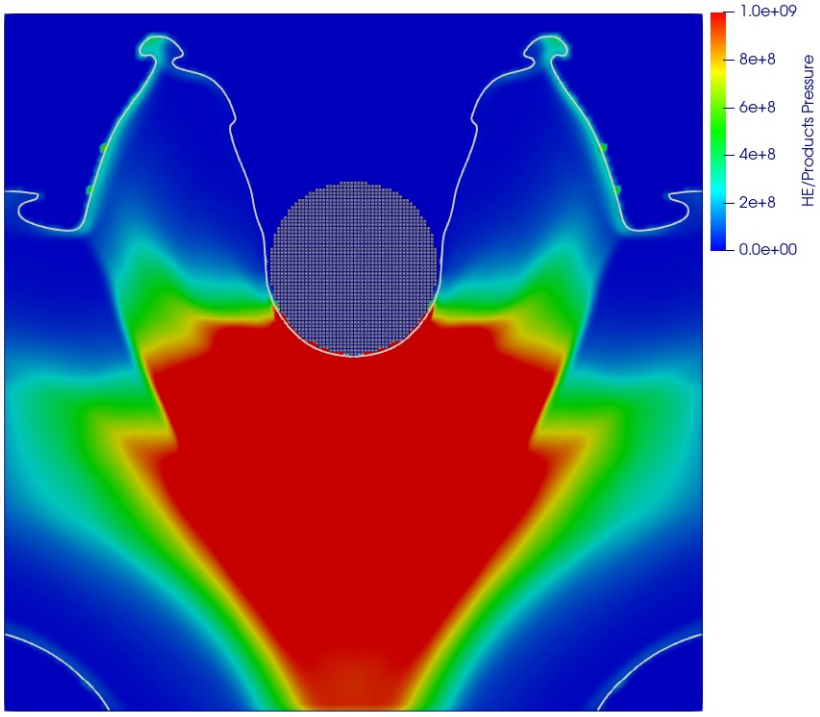

(b)

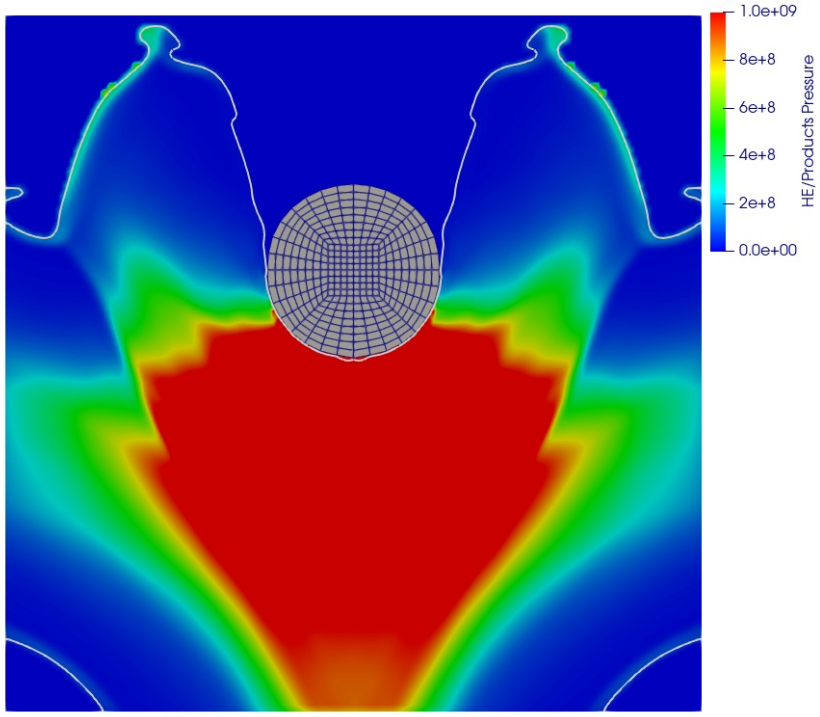

Figure 4-81 Snapshots of the gas pressure and ball location at $t = 2.1 \times 10^{-5} s$ for (a) the Eulerian simulation, and (b) the coupled simulation.

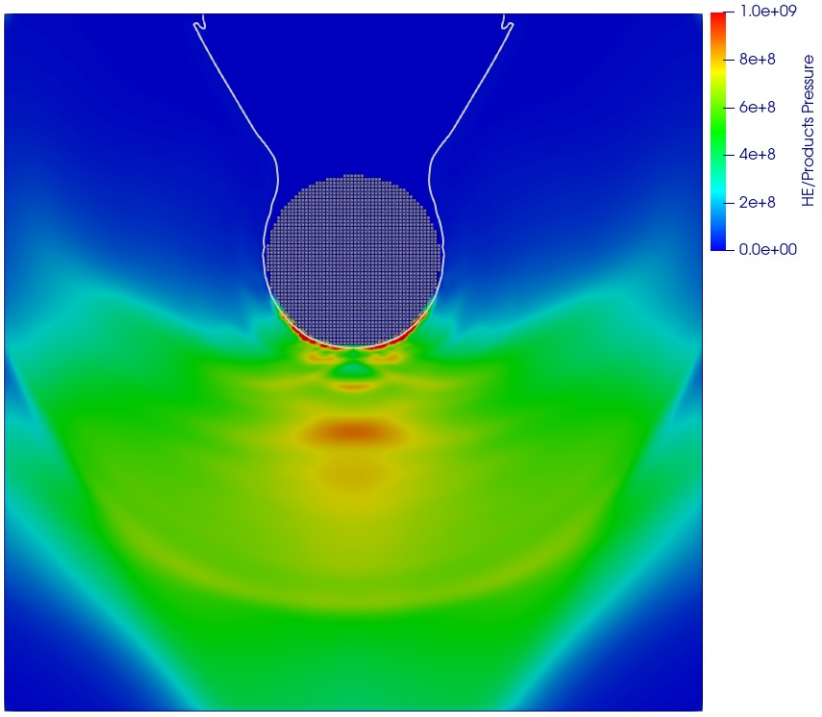

(a)

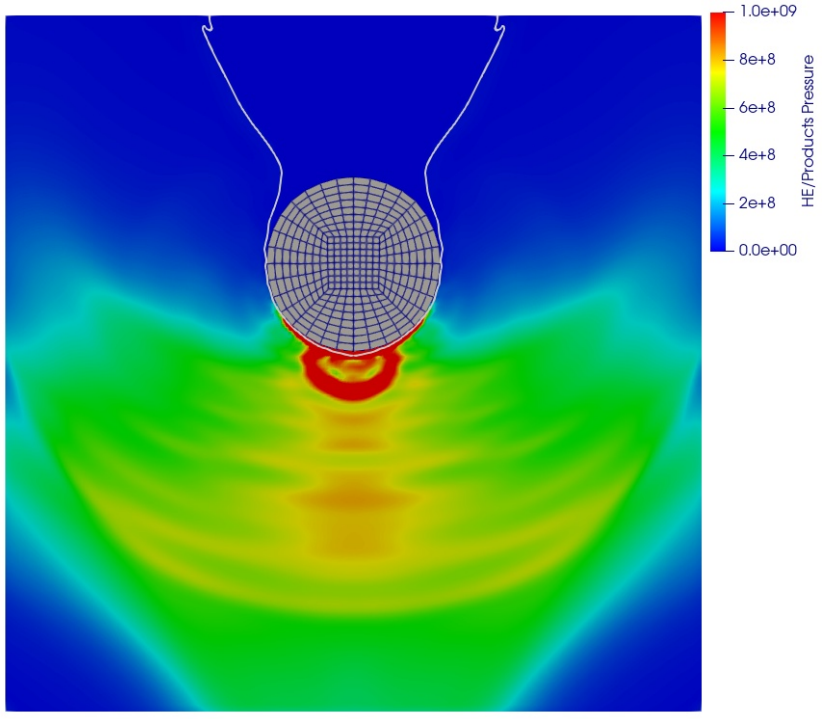

(b)

Figure 4-82 Snapshots of the gas pressure and ball location at $t = 3.1 \times 10^{-5} s$ for (a) the Eulerian simulation, and (b) the coupled simulation.

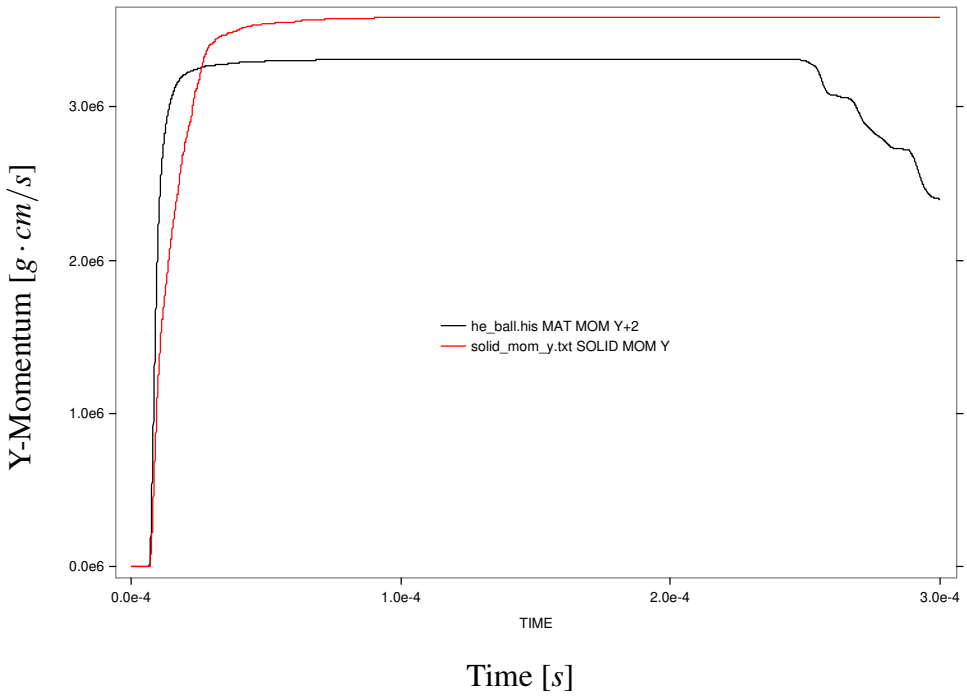

Figure 4-83 Ball y-momentum time history for the Eulerian (–) and Lagrangian (–) calculations.

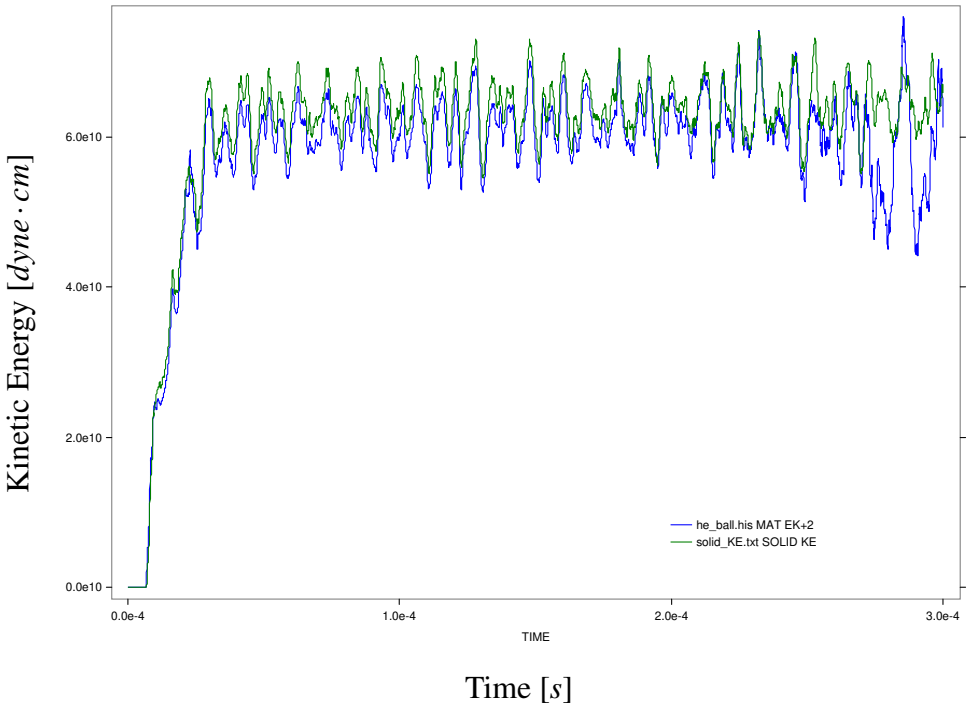

Figure 4-84 Ball kinetic energy time history for the Eulerian (–) and Lagrangian (–) calculations.

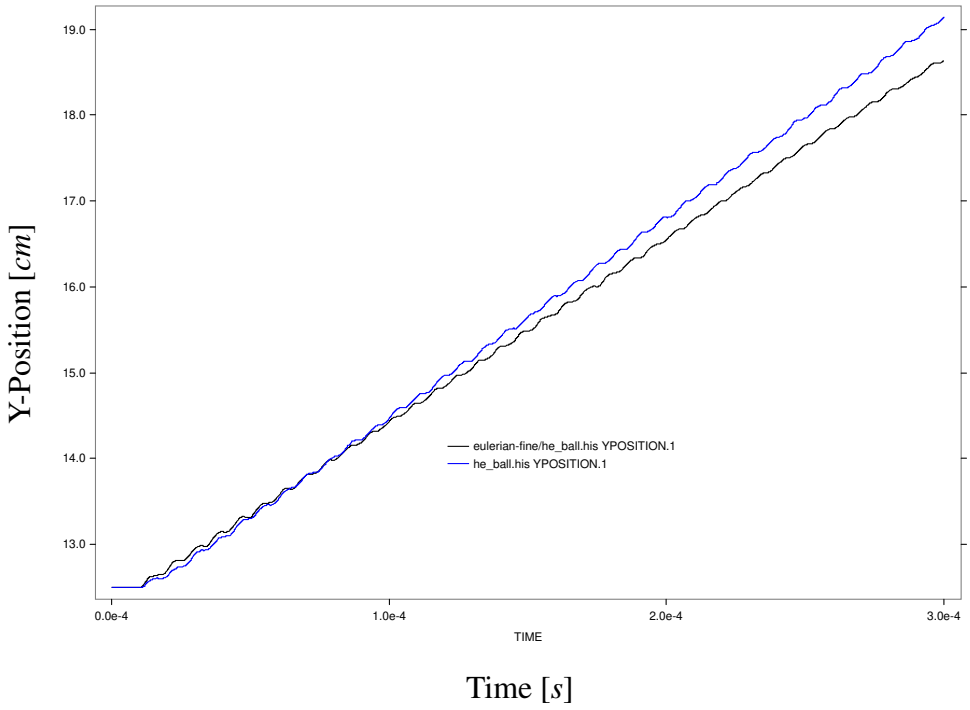

Figure 4-85 Ball y-position time history for the Eulerian (–) and Lagrangian (–) calculations.

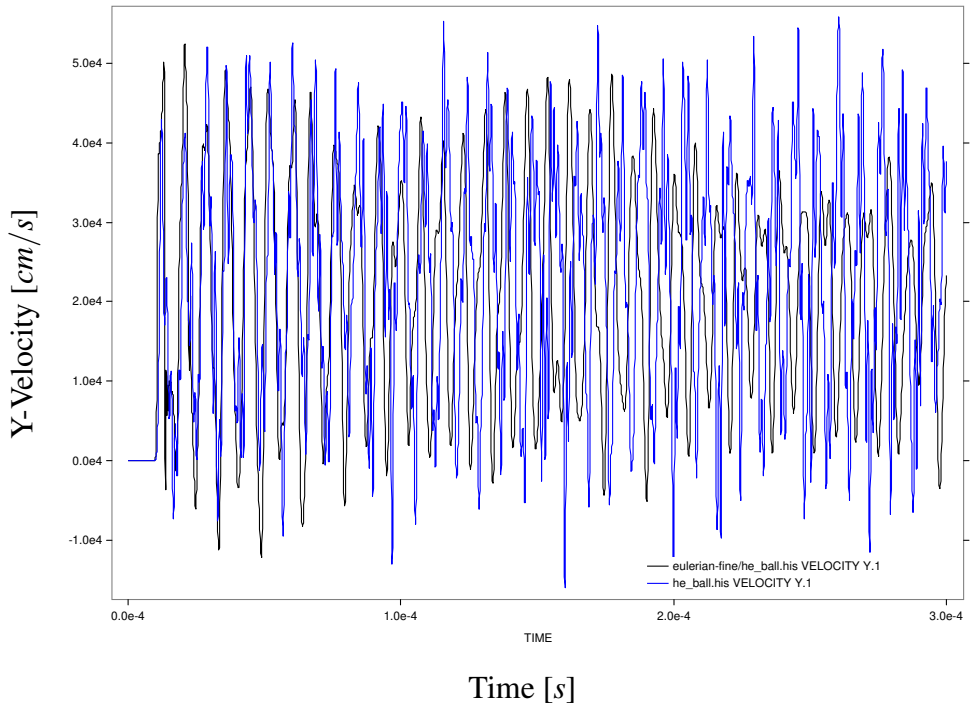

Figure 4-86 Ball y-velocity time history for the Eulerian (–) and Lagrangian (–) calculations.

(a)

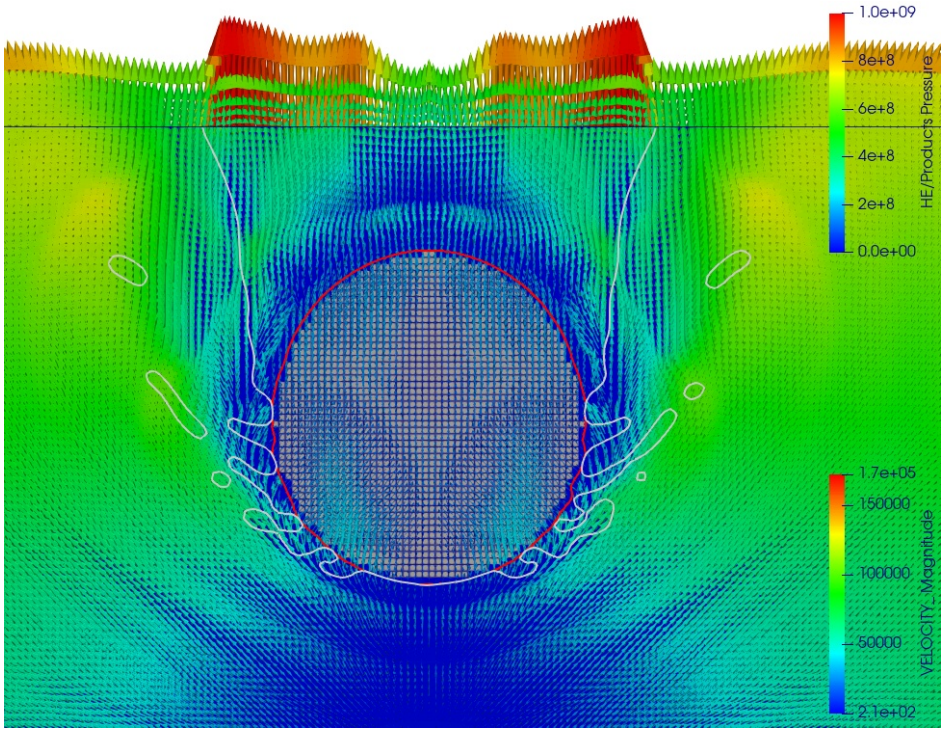

(b)

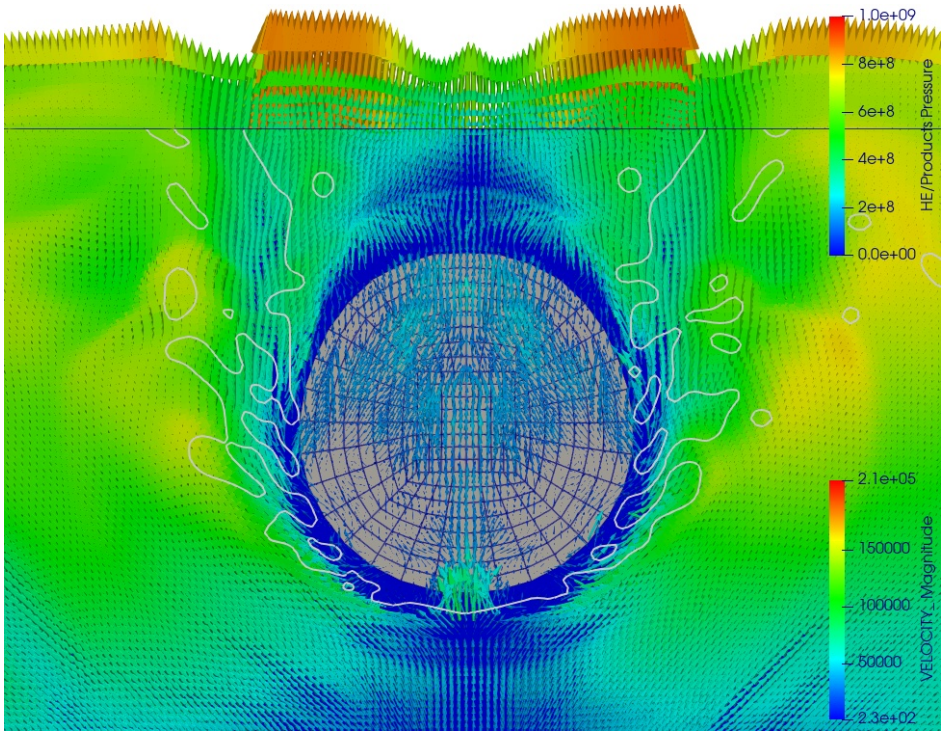

Figure 4-87 Snapshots of the velocity field and ball location for (a) the Eulerian calculation, and (b) the coupled simulation using a matched background material.

4.6. Shock Loading on Balls and Walls

This problem consists of shock loading on five plexiglass balls and two plexiglass walls. The geometry is shown in Figure 4-88. The high pressure gas region has a radius of 0.3 *cm*, with an initial pressure of 10^8 $dynes/cm^2$, and an initial density of 1 g/cm^3. The plexiglass balls have a 0.1 *cm* radius, and are distributed at radius of 0.5 *cm* from the center of the high pressure gas region.

No normal penetration conditions are prescribed along the bottom ($y = 0$) and right ($x = 1.0$) domain boundaries. This constrains the right plexiglass wall, but permits the left plexiglass wall to translate under the shock loading. The plexiglass balls and time-history tracers are located at the coordinates in Table 4-5.

The plexiglass is modeled using a Mie Gruëneisen equation of state, and a linear elastic constitutive model with Young's modulus $E = 2.855 \times 10^{10}$ $dynes/cm^2$ and Poisson's ratio $\nu = 0.355$. For the Eulerian simulation, inter-material fracture between the balls and walls uses a fracture pressure $P_{frac} = 0$ $dynes/cm^2$. For the coupled calculations, a hyper-elastic constitutive model was used with constants chosen to match the equivalent linear elastic model, e.g.,

$$C_1 = \frac{E}{4(1+\nu)} \tag{98}$$

$$C_2 = \frac{E}{3(1-2\nu)} \tag{99}$$

Ball	Location (x, y)
1	$(-0.4330, 0.2500)$
2	$(-0.2500, 0.4330)$
3	$(0.0000, 0.5000)$
4	$(0.2500, 0.4330)$
5	$(0.4330, 0.2500)$

Table 4-5 Ball and tracer point locations. The ball identifiers correspond to the numbers in Figure 4-88.

Figure 4-89 shows snapshots of the gas pressure field, the balls and walls at $t = 1.89 \times 10^{-4}$ and $t = 3.79 \times 10^{-4} s$ for the Eulerian simulation. The corresponding figure for the coupled calculation is shown in Figure 4-90. The mesh lines on the Lagrangian balls indicate that the traction conditions imparted by the plexiglass walls on the balls results in large rigid-body rotations.

Figures 4-91 – 4-100 show the time-history plots of the x- and y-position, and the x- and y-velocity. The overall trends in position and velocity are similar, but there are still substantive differences between the Eulerian and coupled results. Additional work is required to understand and resolve these differences.

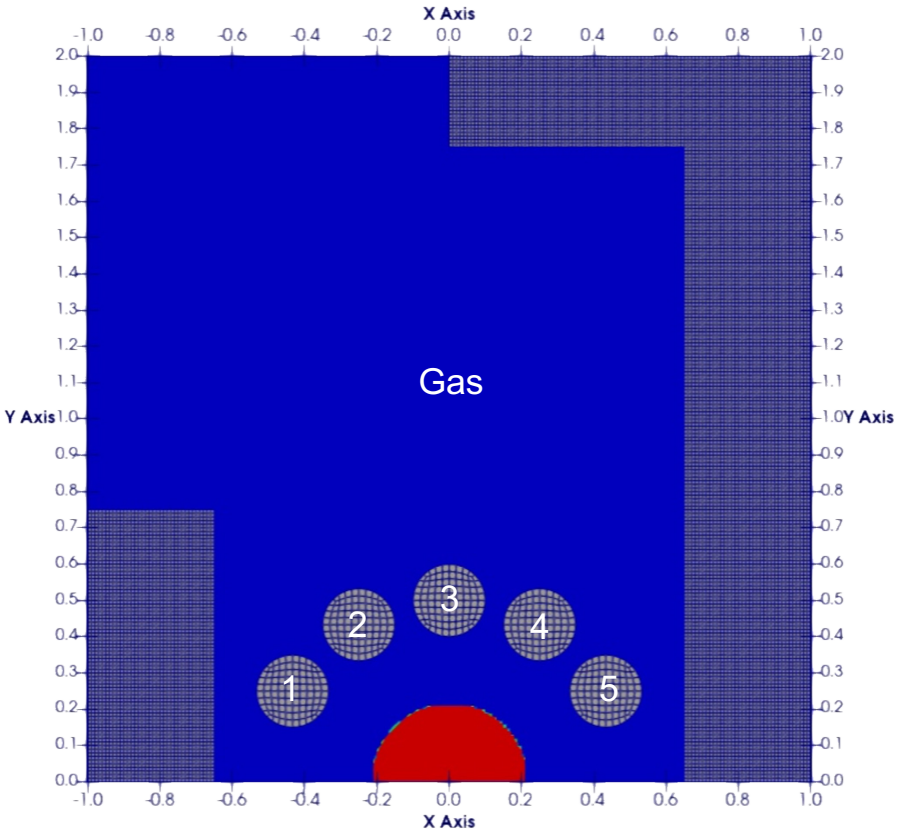

Figure 4-88 Shock loading on balls and walls geometry.

(a)

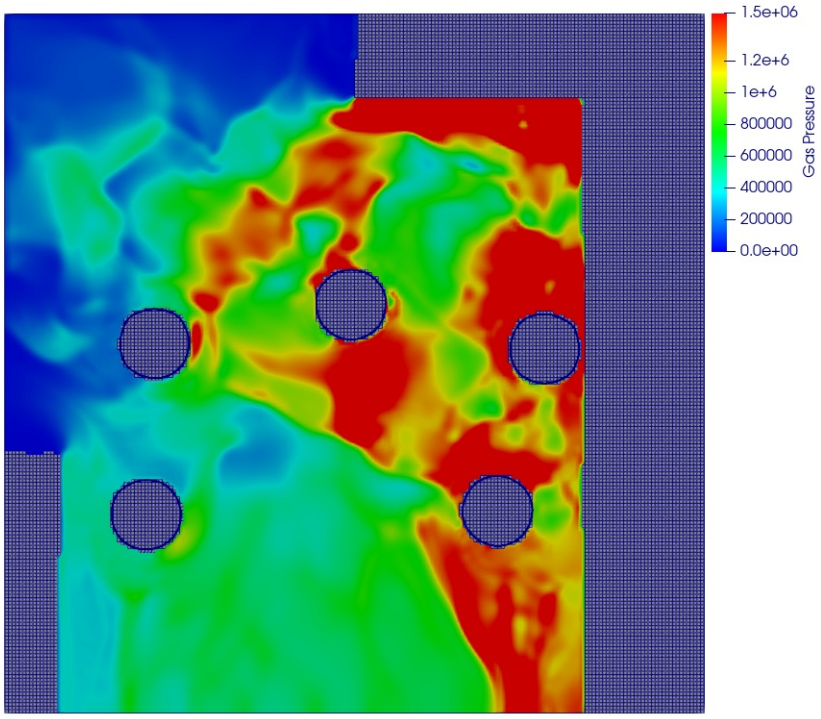

(b)

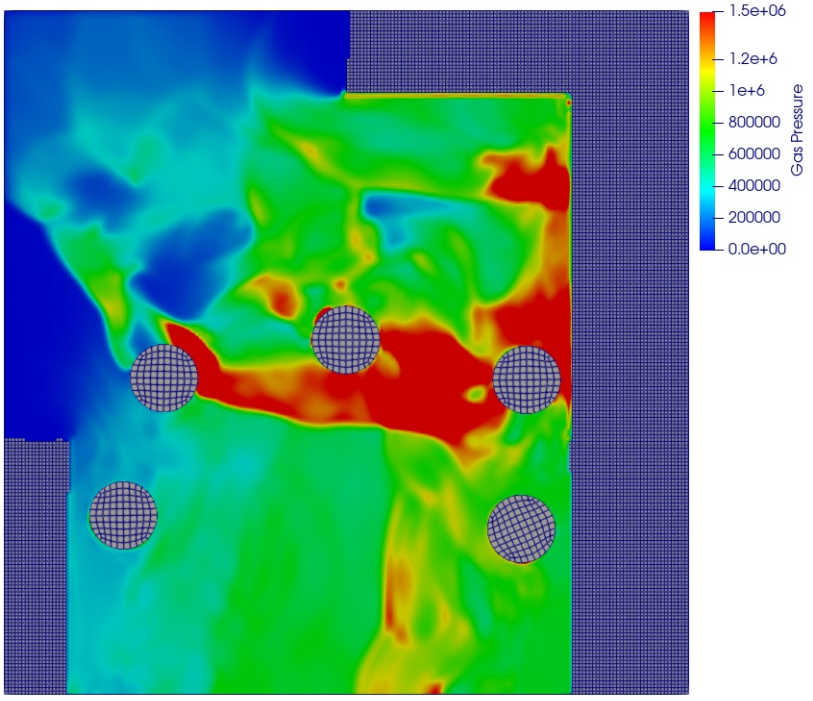

Figure 4-89 Snapshots of the gas pressure and ball location at $t = 1.89 \times 10^{-4}[s]$ for (a) the Eulerian simulation, and (b) the coupled simulation.

(a)

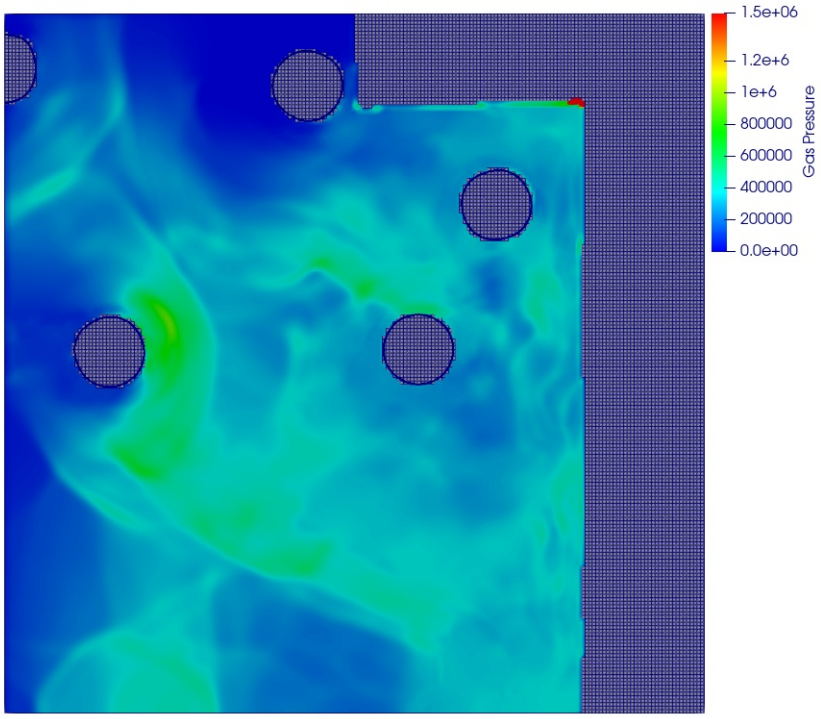

(b)

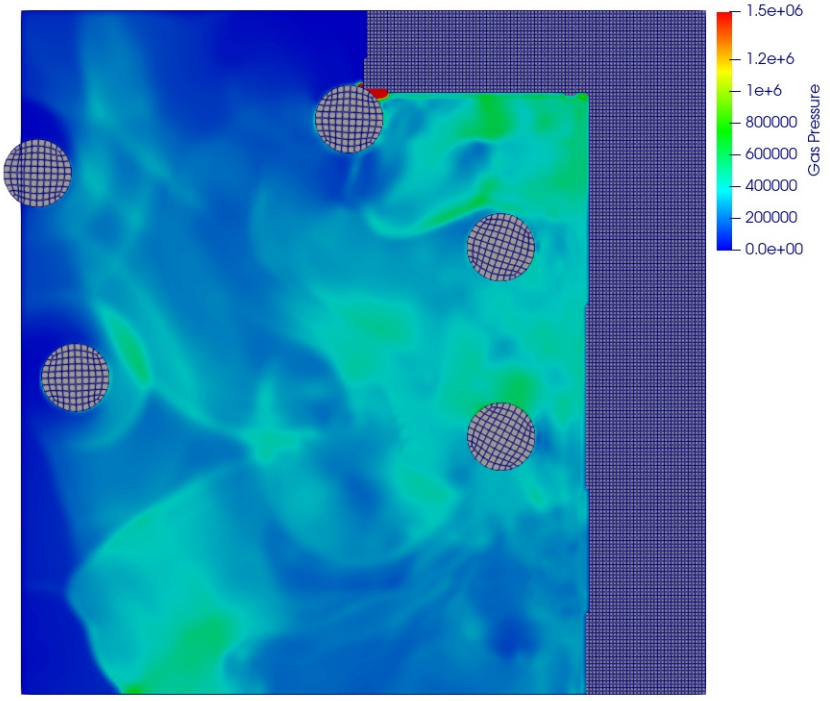

Figure 4-90 Snapshots of the gas pressure and ball location at $t = 3.79 \times 10^{-4}[s]$ for (a) the Eulerian simulation, and (b) the coupled simulation.

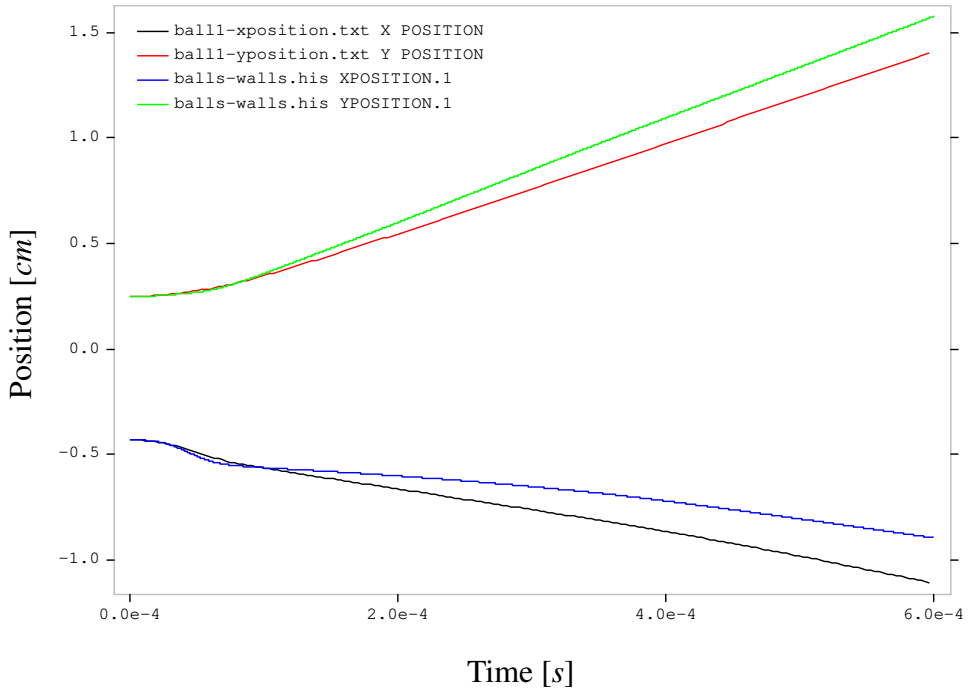

Figure 4-91 Ball-1 position as a function of time: Lagrangian (–) and Eulerian (–) x-position; Lagrangian (–) and Eulerian (–) y-position.

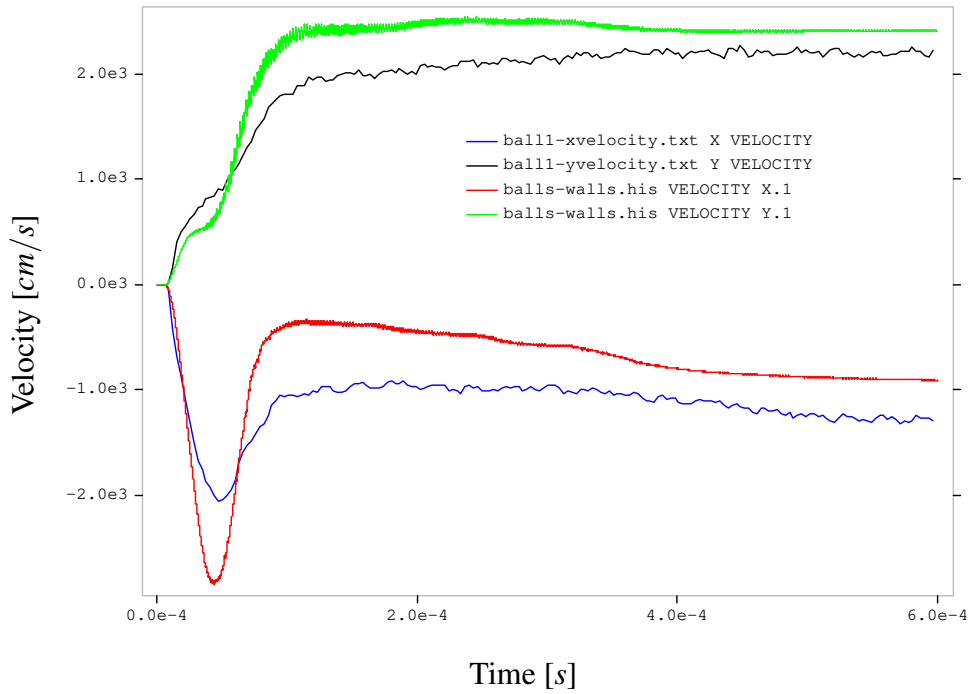

Figure 4-92 Ball-1 velocity as a function of time: Lagrangian (–) and Eulerian (–) x-velocity; Lagrangian (–) and Eulerian (–) y-velocity.

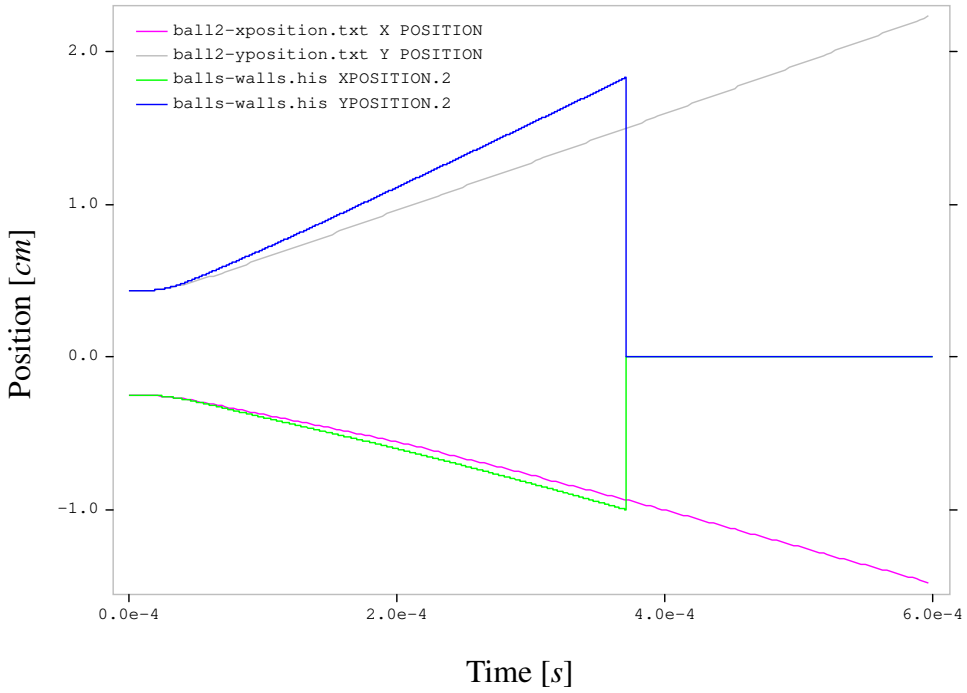

Figure 4-93 Ball-2 position as a function of time: Lagrangian (–) and Eulerian (–) x-position; Lagrangian (–) and Eulerian (–) y-position.

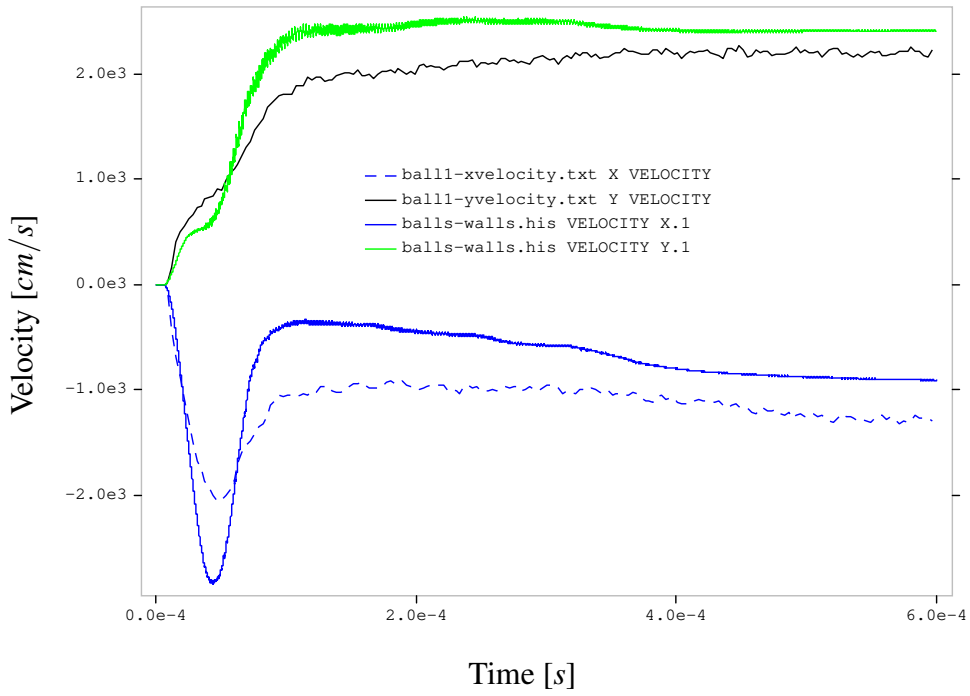

Figure 4-94 Ball-2 velocity as a function of time: Lagrangian (- -) and Eulerian (–) x-velocity; Lagrangian (–) and Eulerian (–) y-velocity.

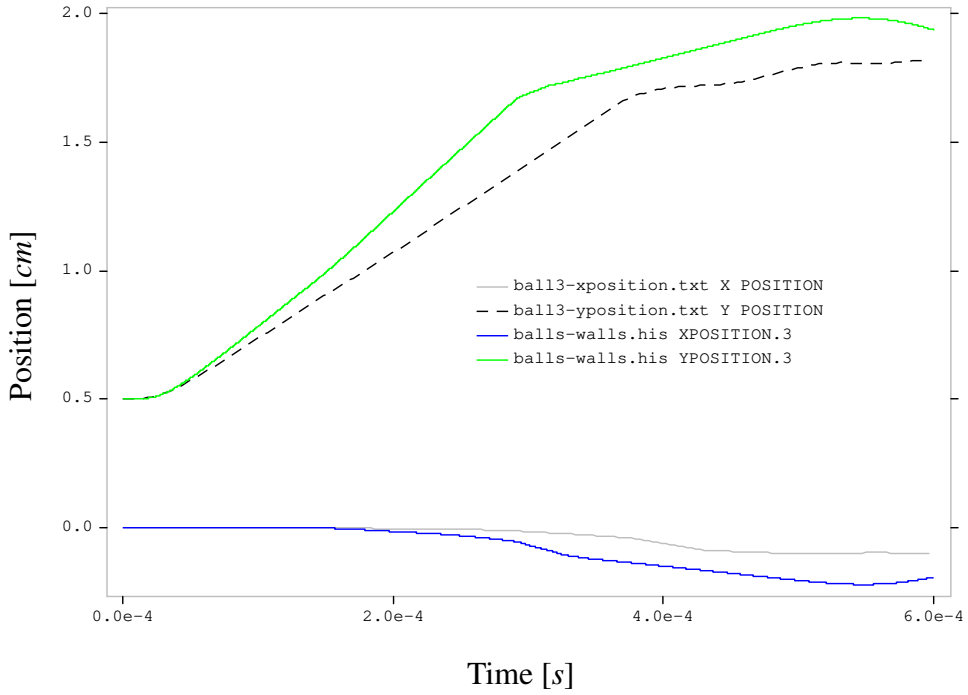

Figure 4-95 Ball-3 position as a function of time: Lagrangian (–) and Eulerian (–) x-position; Lagrangian (- -) and Eulerian (–) y-position.

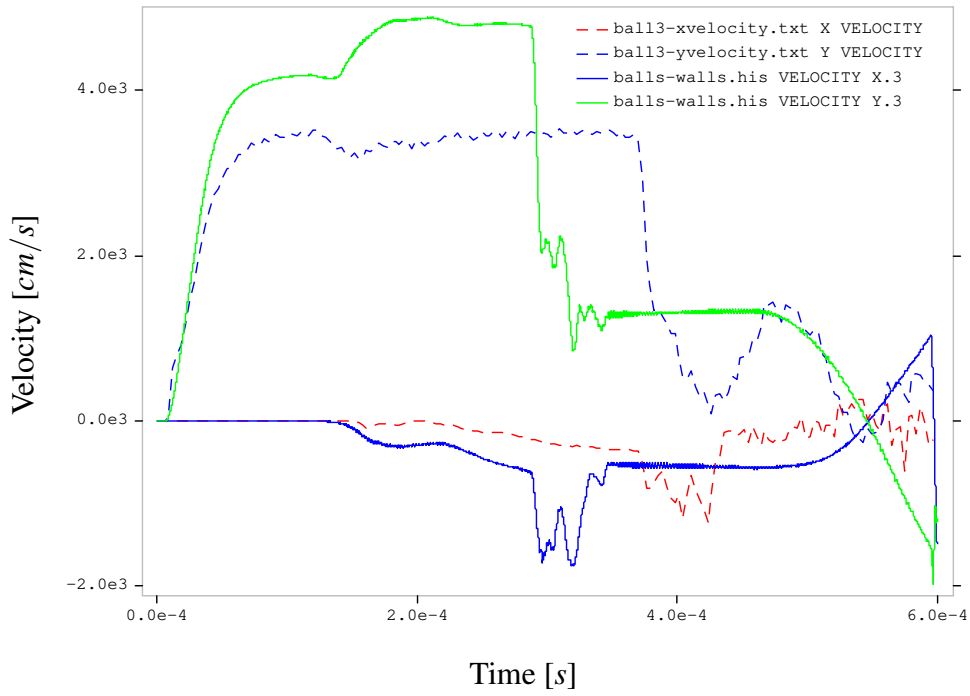

Figure 4-96 Ball-3 velocity as a function of time: Lagrangian (–) and Eulerian (- -) x-velocity; Lagrangian (- -) and Eulerian (–) y-velocity.

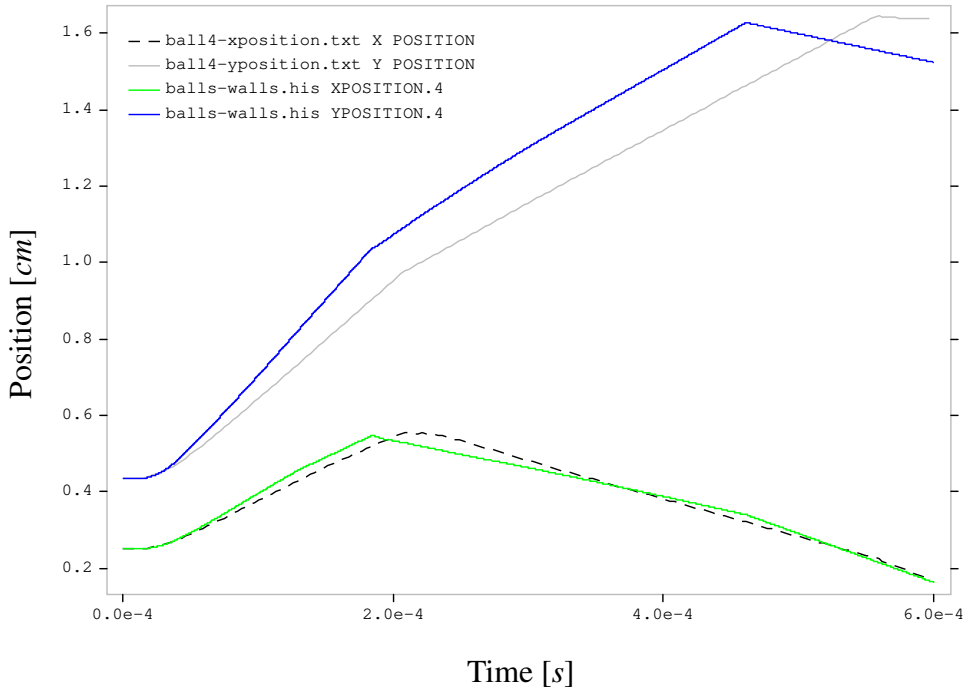

Figure 4-97 Ball-4 position as a function of time: Lagrangian (- -) and Eulerian (–) x-position; Lagrangian (–) and Eulerian (–) y-position.

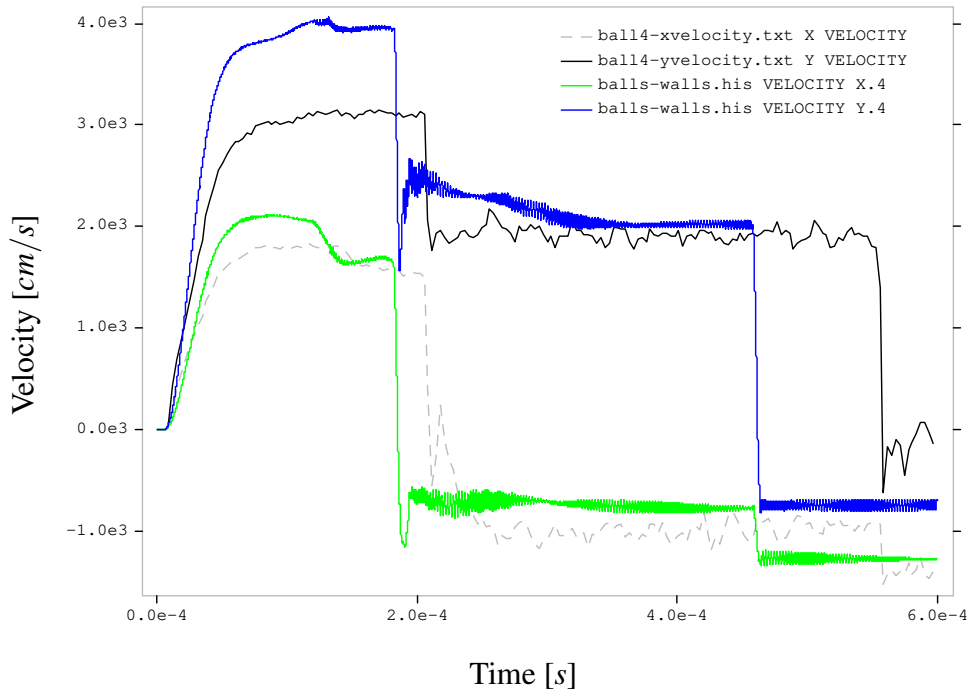

Figure 4-98 Ball-4 velocity as a function of time: Lagrangian (- -) and Eulerian (–) x-velocity; Lagrangian (–) and Eulerian (–) y-velocity.

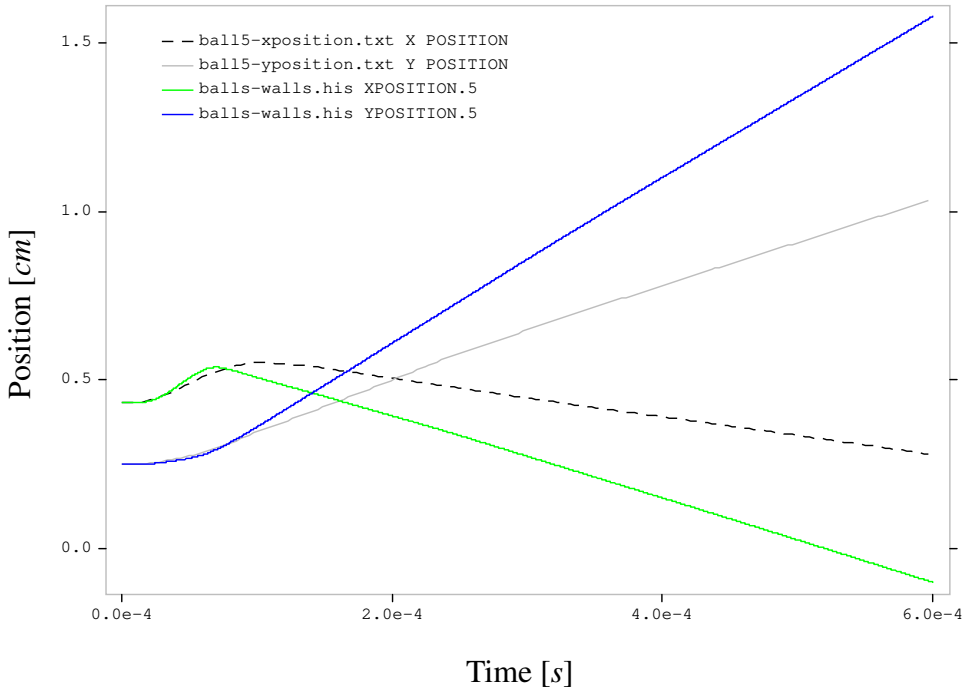

Figure 4-99 Ball-5 position as a function of time: Lagrangian (- -) and Eulerian (–) x-position; Lagrangian (–) and Eulerian (–) y-position.

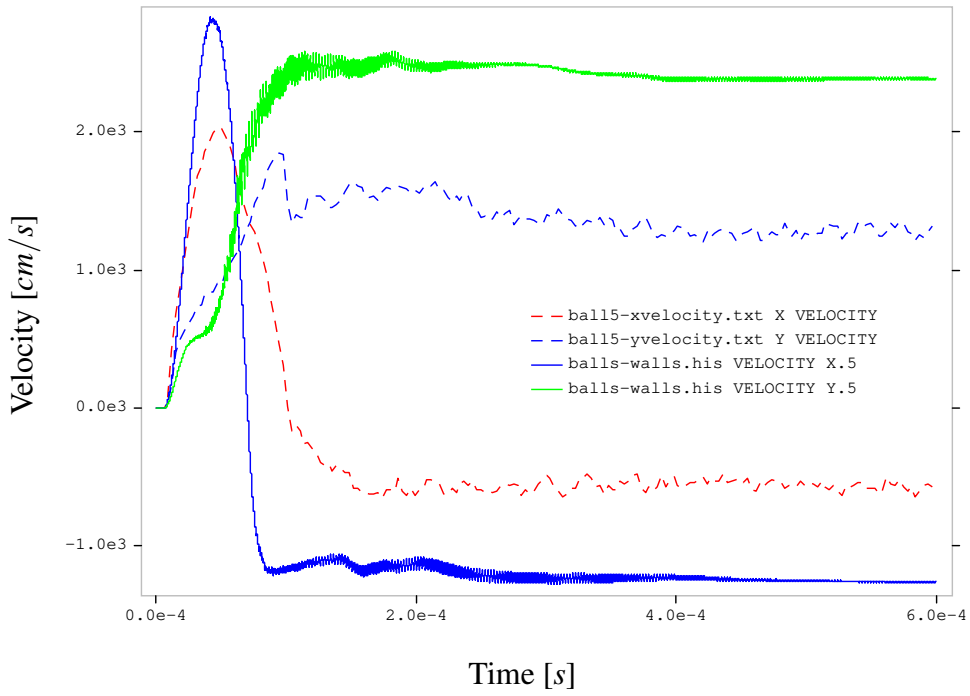

Figure 4-100 Ball-5 velocity as a function of time: Lagrangian (- -) and Eulerian (–) x-velocity; Lagrangian (- -) and Eulerian (–) y-velocity.

4.7. Sphere – Concrete Impact

The sphere – concrete impact problem geometry is shown in Figure 4-101. The sphere is 4340 steel with density $\rho = 7.8724\ g/cm^3$, Young's modulus $E = 2 \times 10^{12}\ dynes/cm^2$, and Poisson's ratio $\nu = 0.28$. The target material is a 23 MPa concrete with density $\rho = 2.040\ g/cm^3$, yield stress $Y = 4.189 \times 10^{10}\ dynes/cm^2$, Poisson's ratio $\nu = 0.345$, and a fracture pressure $P_{frac} = -2.0 \times 10^9\ dynes/cm^2$.

The overall Eulerian domain uses a mesh size of $0.125\ cm$, and spans a square domain $(-2.5, -2.5, -2.5) \leq (x, y) \leq (2.5, 2.5, 2.5)\ cm$. For the Eulerian calculation, the sphere uses the "K and C" SESAME equation of state, and the target uses a KEOS Mie Gruüneisen EOS. The target yield model uses the "CTH GEO" model and associated void insertion model for fracture. Void is used in the region above the target.

The target material has no-displacement conditions prescribed on the bottom and vertical sides and is initially at rest. This case uses a void background where the Lagrangian sphere overlaps the Eulerian mesh. The sphere has an initial downward velocity $v_y = -20,000\ cm/s$. A total simulation time of $100\mu s$ is used for all simulations. For the Eulerian calculations, a Lagrangian tracer is placed at the base of the sphere to measure the overall penetration depth.

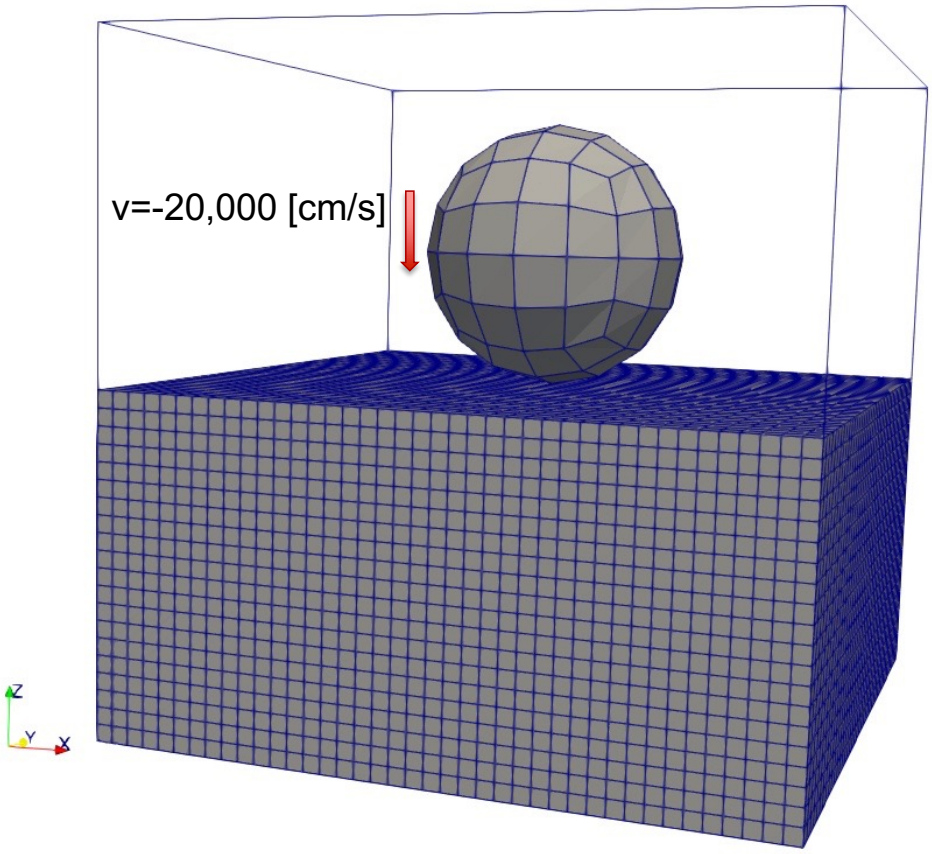

Figure 4-101 Sphere – concrete impact problem.

The penetration depth, measured at the base of the sphere, is shown in Table 4-6 for the Eulerian and coupled simulations. The coupled simulation over-predicts the penetration depth relative to the Eulerian calculation by 1.4%. The penetration depth time-history for the Eulerian and coupled simulations is shown in Figure 4-102.

Figures 4-103 and 4-104 show the time-histories for the sphere z-momentum and kinetic energy for the Eulerian and coupled simulations. The initial z-momentum for the Lagrangian sphere is slightly less than the Eulerian sphere due to the relatively coarse Lagrangian mesh. The momentum time-history shows that the Lagrangian sphere loses slightly more momentum, i.e., is moving slower from $0.4 \times 10^{-}4$ to $1.0 \times 10^{-}4$ $[s]$. This correlates with the kinetic energy histories where the Lagrangian penetrator has slightly lower kinetic energy values.

The concrete target time histories for y-momentum and kinetic energy are shown in Figures 4-105 and 4-106. The coupled calculation under-predicts the target z-momentum and kinetic energy. This is undoubtedly due to the coarse Lagrangian sphere mesh, and the momentum/energy transfer at the Lagrangian-Eulerian interface. Figure 4-107 shows the snapshots of the velocity field at $t = 100\mu s$ for the Eulerian and coupled Eulerian-Lagrangian simulations. The coupled simulation predicts a peak z-velocity that is 2.4% larger than the Eulerian simulation

Simulation	Penetration Depth [cm]
Eulerian	-1.2352
Coupled	-1.2527

Table 4-6 Penetration depth based on the base of the sphere for Eulerian and coupled simulations at $t = 100\mu s$.

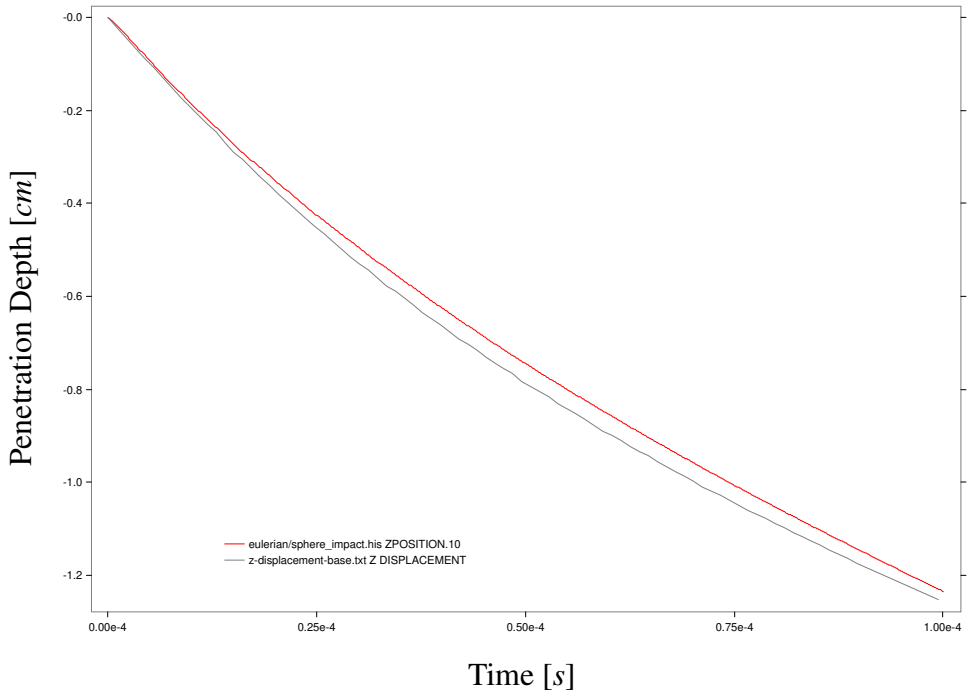

Figure 4-102 Sphere penetration depth time history for the Eulerian (–) and coupled Eulerian-Lagrangian (–) calculations.

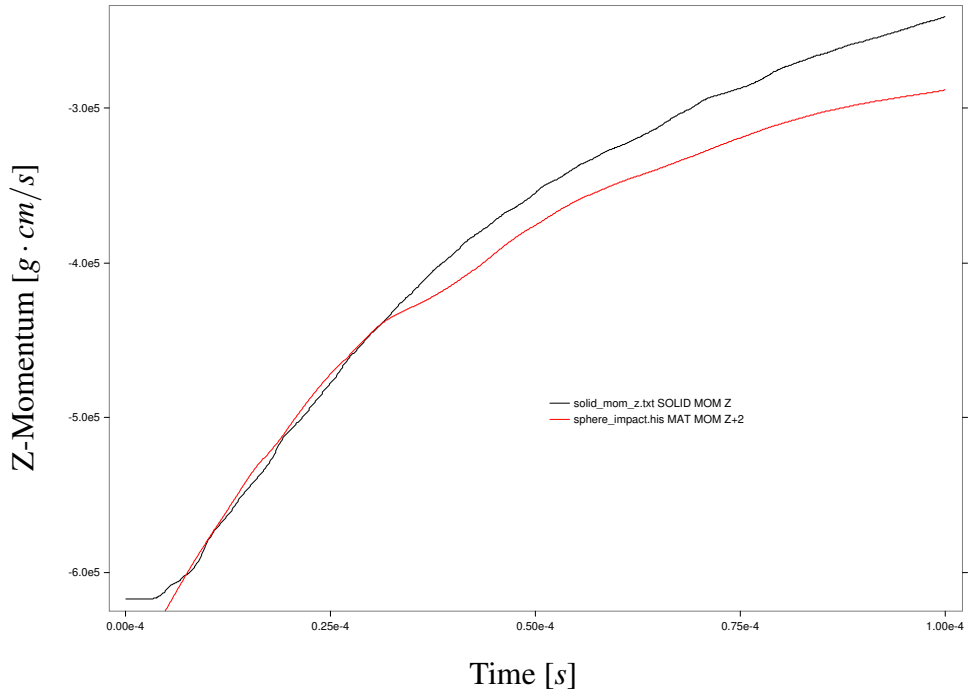

Figure 4-103 Sphere z-momentum time history for the Eulerian (–) and coupled Eulerian-Lagrangian (–) calculations.

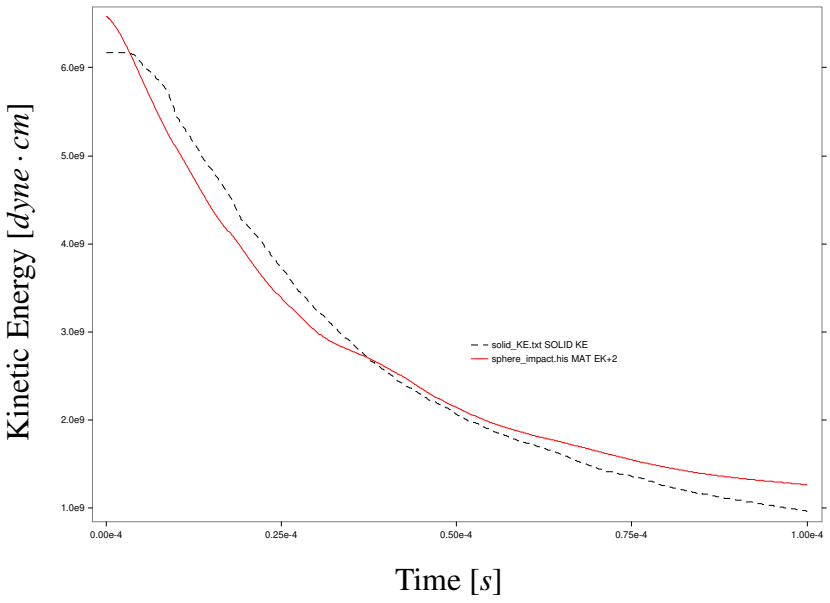

Figure 4-104 Penetrator kinetic energy time history for the Eulerian (–) and coupled Eulerian-Lagrangian (- -) calculations.

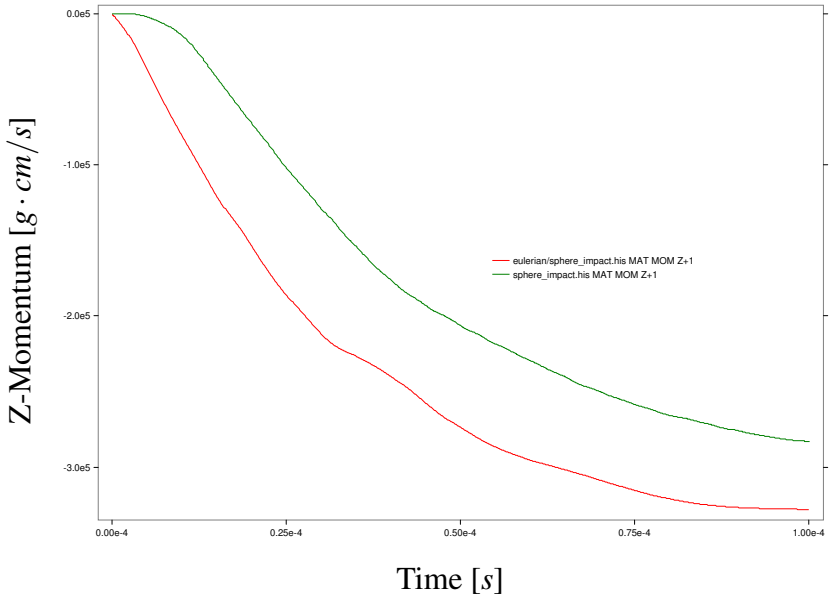

Figure 4-105 Target z-momentum time history for the Eulerian (–) and coupled Eulerian-Lagrangian (–) calculations.

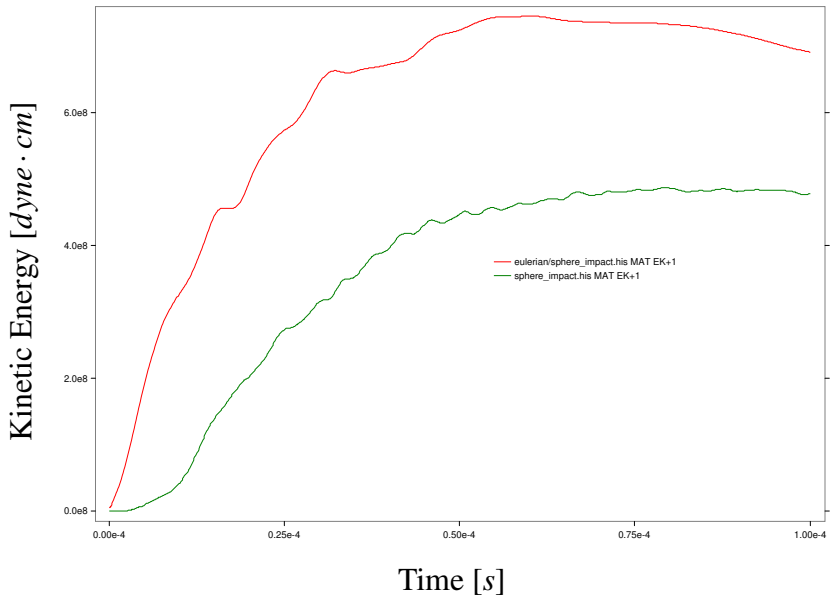

Figure 4-106 Target kinetic energy time history for the Eulerian (–) and coupled Eulerian-Lagrangian (–) calculations.

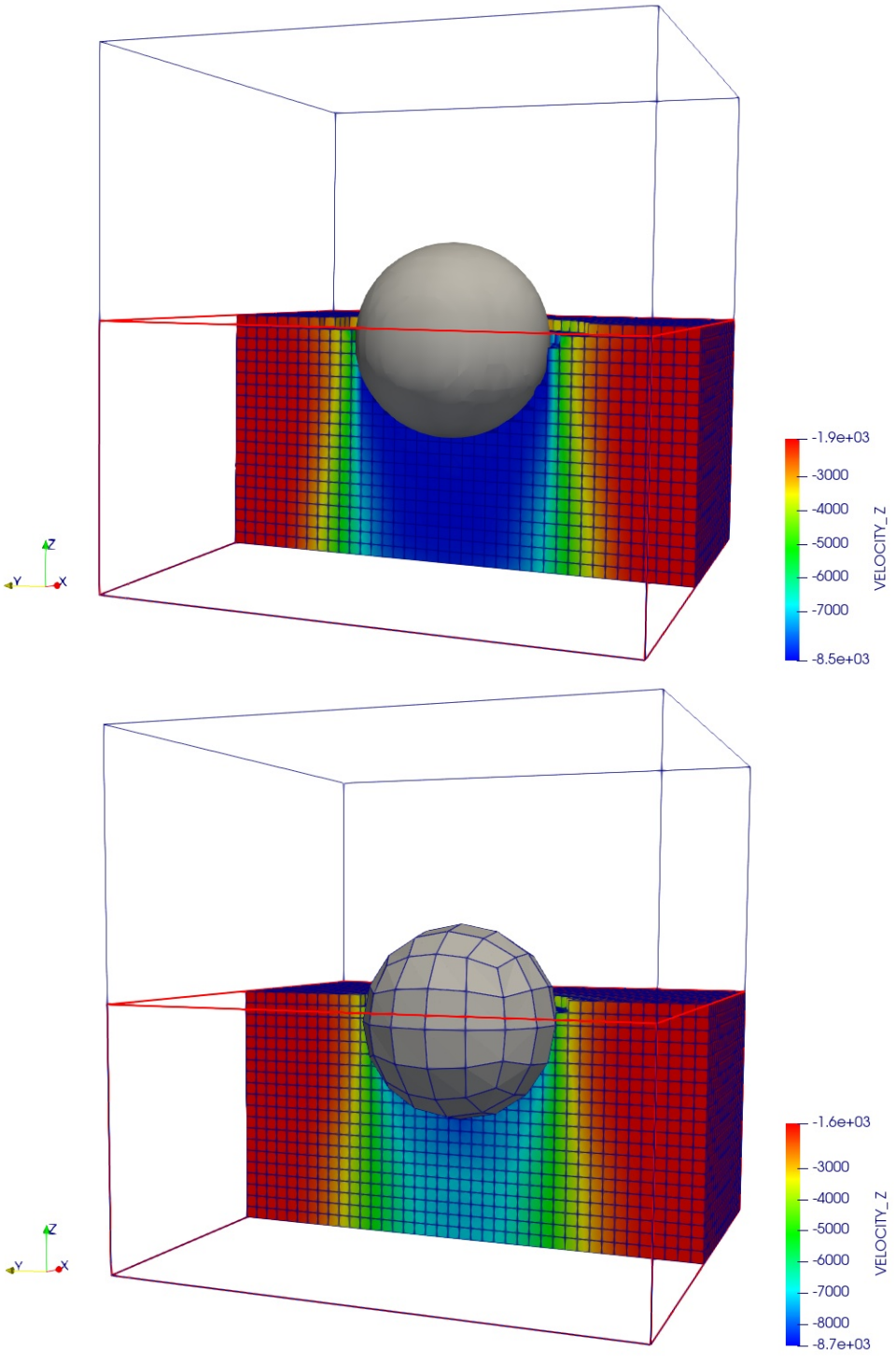

Figure 4-107 Target velocity magnitude at $t = 100\mu s$ for (a) the Eulerian, and (b) the coupled Eulerian-Lagrangian calculations.

5. SUMMARY AND CONCLUSIONS

The current effort has provided an in-depth investigation into the immersed finite element method for the purposes of providing a minimally invasive Lagrangian-Eulerian coupling technique for coupled simulations. The work with OPENIFEM and SABLE has demonstrated that the modified immersed finite element method is quite robust and provides a rigorous framework for Lagrangian-Eulerian coupling.

A number of extensions to the base method have been examined in this work. These extensions include

- Nodal and quadrature-point based indicator functions
- A more precise Lagrangian volume-fraction calculation, along with the associated improvements in the nodal coupling mass matrix
- The use of penalty constraints for the velocity continuity at the interface between the Eulerian and Lagrangian boundary
- A velocity reset for overlapping regions where void exists in the Eulerian model
- An MPI based coupling strategy that retains the MPI structure of each independent code without modifications to the underlying communications structure

The investigation of a direct velocity enforcement for the coupling did not always produce physically consistent results, and was dropped. The ability to build-in the Lagrangian volume fraction constraint in the Eulerian interface reconstruction and material remap procedure to properly partition and constrain material fluxes was investigated but deemed outside the scope of the current work.

Future work will consider the following items

- Integration of the Lagrangian volume fraction constraint in the Eulerian interface reconstruction and material remap
- Separating the normal and tangential traction forces, to permit using only normal forces, i.e., permitting slip conditions
- A detailed convergence study and analysis of errors generated in the overlap region of the Eulerian domain

REFERENCES

[1] Jie Cheng, Feimi Yu, and Lucy T. Zhang. OpenIFEM: a high performance modular open-source software of the immersed finite element method for fluid-structure interactions. *Computer Modeling in Engineering & Sciences*, 119(1):91 – 124, 2019.

[2] D. P. Flanagan and T. Belytschko. A uniform strain hexahedron and quadrilateral with orthogonal hourglass control. *International Journal for Numerical Methods in Engineering*, 17:679–706, 1981.

[3] C. S. Peskin. Numerical analysis of blood flow in the heart. *Journal of Computational Physics*, 25:220 – 252, 1977.

[4] C. S. Peskin. The immersed boundary method. *Acta Numerica*, 11:479 – 517, 2002.

[5] Xingshi Wang and Lucy T. Zhang. Modified immersed finite element method for fully-coupled fluid-structure interactions. *Computer Methods in Applied Mechanics and Engineering*, 267:150 – 169, 2013.

[6] Lucy Zhang, Axel Gertenberger, Xiaodong Wang, and Wing Kam Liu. Immersed finite element method. *Computer Methods in Applied Mechanics and Engineering*, 193:2051 – 2067, 2004.

[7] Lucy T. Zhang and M. Gay. Immersed finite element method for fluid-structure interactions. *Journal of Fluids and Structures*, 23(6):839 – 857, 2007.

APPENDIX A. SABLE KEYWORDS

SABLE keywords specific to coupling with OPENIFEM.

Remove background material under Lagrangian body for stress. As many background materials can be specified as required for a given problem.

```
domain
  background coupling material = matId_1
  ...
  background coupling material = matId_N
end
```

Activate velocity-coupling, note force-coupling is the default.

```
domain
  velocity coupling
end
```

Reset nodal velocities to the Lagrangian velocity at nodes with pure void. The Default is NOT to reset the void coupling velocity.

```
domain
  reset void coupling velocity
end
```

In cases where the Eulerian penalty term is required, the following keywords activate the penalty terms, and set the penalty scale factor. The default scale factor is 0.0, and must be in the range 0.0 to 1.0.

```
domain
  coupling penalty scale factor = 0.0
end
```

For debugging coupling, the following plot variables are useful.

```
plot, exodus
  plot variable
    coupling_node_mass
    coupling_density
    coupling_volfraction
    coupling_ol_volfraction
    oifemforce
    oifemvel
```

```
    oifemvflag
    oifemnodevfrac
   end
end
```

For debugging the Lagrangian step, the following is useful as well. This requires "debug mode: lagrangian" in the SABLE input file.

```
debug mode: lagrangian

plot, exodus
  plot variable
    sableforce
    totalforce
    acceleration
    volume
    el_mass
    char_length
    displacement
    lag_velocity
   end
end
```

APPENDIX B. OPENIFEM KEYWORDS

OPENIFEM keywords specific to coupling with SABLE.

```
# Set condition for calculating indicator field (only applied to OpenIFEM-SABLE Coupling)
# Options: CompletelyInsideSolid and PartiallyInsideSolid
set Indicator field condition = CompletelyInsideSolid

# Set criteria for calculating indicator field and FSI force
# Options: Nodes and QuadraturePoints
# set FSI force criteria = Nodes
set FSI force criteria = QuadraturePoints

# Set an option for SABLE stress used in calculation of FSI force
# Options: CellBased and NodeBased
# Default is CellBased
set SABLE stress option for calculating FSI force = CellBased

# Set an option for SABLE stress used in calculation of solid traction
# Options: CellBased and NodeBased
```

```
# Default is CellBased
set SABLE stress option for calculating solid traction = CellBased

# Surface normal extension (beta)
# Default = 0.0
set scale for solid traction extension along the face normal = 0.0

# Added mass toggle
# set use added mass = yes to use compute the added mass term
# Default = yes
  set use added mass = no

# Set penalty_scale_factor
# Should be between 0.0 and 0.5
# Default = 0.5
  set penalty scale factor = 0.0
```

DISTRIBUTION

Hardcopy—Internal

Number of Copies	Name	Org.	Mailstop
1	Kyran D. Mish	01555	MS 0845
1	Russell D. Teeter	01555	MS 0840
1	Michael K. Wong	01554	MS 0840
1	David M. Hensinger	01555	MS 0840
1	Scott T. Miller	01542	MS 0845

Email—Internal (encrypt for OUO)

Name	Org.	Sandia Email Address
Technical Library	1911	sanddocs@sandia.gov

Sandia National Laboratories

Sandia National Laboratories is a multimission laboratory managed and operated by National Technology & Engineering Solutions of Sandia LLC, a wholly owned subsidiary of Honeywell International Inc., for the U.S. Department of Energy's National Nuclear Security Administration under contract DE-NA0003525.